Ida Bochert

Diffusion Tools for Biological Systems

Dissertation

Max-Planck-Institut für Medizinische Forschung, Heidelberg
Institute for Molecular Systems Engineering and Advanced Materials,
Universität Heidelberg

INAUGURAL - DISSERTATION

zur

Erlangung der Doktorwürde

der

Gesamtfakultät für

Mathematik, Ingenieur- und Naturwissenschaften

der Ruprecht-Karls-Universität

Heidelberg

Vorgelegt von

Ida Saskia Bochert

geb. in Stuttgart

Tag der mündlichen Prüfung: 14.07.2025

Diffusion Tools for Biological Systems

Gutachter: Prof. Dr. Peer Fischer

Prof. Dr. Christine Selhuber-Unkel

To Oma Irmgard,
who is always interested in my research
and would have been a great scientist
if she had been given the opportunity.

Contents

Abstract

The diffusion of nanoparticles can be used to determine the structure of complex media, or as a probe to detect binding of an analyte. Two methods of diffusion measurements are presented to investigate nanoparticle diffusion mechanisms in different environments. One is used to detect the presence of DNA biomarkers, which is important for medical diagnosis. A biomarker can connect two DNA origami structures, causing a decrease in the diffusion coefficient of the origami structure, which is a means to detect the biomarker. Measurements at picomolar concentration by Fluorescence Nanoparticle Tracking Analysis are shown to detect a random DNA sequence and a characteristic sequence of an antibiotic resistance gene within a few minutes. The method shows that diffusion can be a tool for detecting DNA and suggests an application in the sensing of biologically relevant analytes. Further, Pulsed Field Gradient Nuclear Magnetic Resonance of liquid core particles enables direct, label-free diffusion measurements, even in complex or optically opaque media. It is shown that this permits the mesh size of a hydrogel to be probed, suggesting that this method may be used to characterize the microstructure of living tissue and other biologically relevant media.

Zusammenfassung

Die Diffusion von Nanopartikeln kann zur Strukturaufklärung komplexer Medien oder als Sonde zum Nachweis der Bindung eines Analyten genutzt werden. In dieser Arbeit werden zwei Methoden für Diffusionsmessungen vorgestellt, welche die Diffusion von Nanopartikeln in verschiedenen Umgebungen untersuchen. Die erste Methode dient dem Nachweis von DNA-Biomarkern, was für die medizinische Diagnostik von Bedeutung ist. Eine Verringerung des Diffusionskoeffizienten von DNA-Origami Strukturen, die durch eine Verbindung zweier Strukturen aufgrund eines Biomarkers verursacht wird, kann zu dessen Nachweis genutzt werden. Fluoreszenzbasierte Nanopartikel-Tracking-Analyse ermöglicht Messungen bei pikomolaren Konzentrationen innerhalb weniger Minuten. Dies wird anhand einer zufälligen DNA-Sequenz sowie der charakteristischen Sequenz eines Gens für Antibiotikaresistenz gezeigt. Die Methode zeigt auf, dass Diffusion zum Nachweis von DNA genutzt werden kann und legt eine Anwendung in der Detektion biologisch relevanter Analyten nahe. Darüber hinaus kann die Diffusion von flüssigkeitsgefüllten Nanopartikeln mithilfe von Feldgradienten-Kernspinresonanz direkt und ohne den Zusatz von Markern gemessen werden, was den Einsatz in komplexen oder optisch undurchlässigen Medien ermöglicht. Es wird gezeigt, dass damit die Mikrostruktur eines Hydrogels untersucht werden kann, was einen möglichen Einsatz der Methode in der Erforschung der Mikrostruktur von lebendem Gewebe oder biologisch relevanten Medien in Aussicht stellt.

List of Symbols and Abbreviations

Symbols

a	Radius of a spherical pore
$\boldsymbol{B}$	Vector of the magnetic field (magnetic flux density)
B_0	Strength of static magnetic field (magnetic flux density)
B_1	Strength of oscillating magnetic field (magnetic flux density)
b	Diffusion weighting parameter in PFG NMR
c	Concentration (of particles)
$\Gamma(x)$	Gamma function
γ	Gyromagnetic ratio
D	(Translational) diffusion coefficient
$\langle D \rangle$	Mean diffusion coefficient (of a distribution)
D_0	(Free) Diffusion coefficient in absence of interactions
d	Diameter
d_h	Hydrodynamic diameter
d_max	Maximum of size distribution
Δ	Diffusion time
Δf	Uncertainty of f
δ_g	Gradient pulse duration (PFG NMR)
$\delta_\mathrm{g,eff}$	Effective gradient pulse duration (PFG NMR)
δ	Chemical shift
$\delta(\boldsymbol{x})$	Dirac delta distribution
η	(Dynamic) viscosity
f	Frequency

g	Gradient pulse strength (PFG NMR)
$g_{\max}$	Maximum gradient pulse strength (PFG NMR)
$\hbar$	Reduced Planck constant
I	Nuclear spin quantum number
I	NMR echo signal intensity
I_0	NMR echo signal intensity in absence of gradient
k_{B}	Boltzmann constant
$\boldsymbol{M}$	Magnetization
M	Molecular mass
μ	Individual magnetic moment
m_{I}	Magnetic quantum number
O1, O2	End of DNA origami 6HB
$P(D)$	Distribution of diffusion coefficients
$P(D;\kappa,\theta)$	Gamma distribution of D
$\tilde{P}(D;\kappa,\theta)$	Number-weighted gamma distribution of D
$\tilde{P}(r;\kappa,\theta)$	Size distribution obtained from $\tilde{P}(D;\kappa,\theta)$
$P(\boldsymbol{r}\|\boldsymbol{r'},t)$	Conditional probability density of being at $\boldsymbol{r'}$ for time t when starting at $\boldsymbol{r}$ at a time $t=0$
$p(x)$	Log-normal distribution of x
R	Radius
R_{h}	Hydrodynamic radius
R_{i}	Inner radius (of a hollow particle)
R_{shell}	Shell thickness
$\boldsymbol{r}$	Position
$\langle r^2 \rangle$	Mean squared displacement
Re	Reynolds number
ρ	Density
σ	Standard deviation
T	Temperature
t	Time
τ	Lag time in spin echo experiments
T_1	Spin-lattice (longitudinal) relaxation constant

T_2	Spin-spin (transverse) relaxation constant
T_2^*	Effective transverse relaxation constant
T_2'	Transverse relaxation contribution caused by local inhomogeneities
V	Volume
x', y'	Co-rotating coordinate system
ξ	Mesh size
ω	Angular velocity
ω_L	Larmor frequency
∇	Differential operator Nabla

Abbreviations

6HB	Six-helix bundle
A, C, G, T	Nucleobases of DNA: adenine, cytosine, guanine, thymine
DNA	Deoxyribonucleic acid
diffSe	Diffusion spin echo pulse sequence
diffSte	Diffusion stimulated echo pulse sequence
DLS	Dynamic Light Scattering
dsDNA	Double stranded DNA
FID	Free induction decay
FWHM	Full width at half maximum
IM	DNA sequence
IR	Inversion-Recovery
MD	Molecular Dynamics (simulation)
MSD	Mean squared displacement
NoB	'Non-Binding' DNA sequence *ACAGA*
NTA	Nanoparticle Tracking Analysis
NTA-FL	Fluorescence Nanoparticle Tracking Analysis
Oxa	DNA sequence based on antibody resistance gene blaOxa-48
PCR	Polymerase Chain Reaction
PFG NMR	Pulsed Field Gradient Nuclear Magnetic Resonance
PSD	Particle size distribution

RMSF	Root-mean-squared-fluctuation
SEM	Scanning Electron Microscope
SES eq.	Stokes-Einstein-Sutherland equation
ssDNA	Single stranded DNA
TC	Temperature cycling
TEM	Transmission Electron Microscope

Chemicals

DCM	Dichloromethane
EDTA	Ethylenediaminetetraacetic acid
HA	Hyaluronic acid
HAMA	Hyaluronic methacrylate
LAP	Photoinitiator Lithium phenyl-2,4,6-trimethylbenzoylphosphinate
PMMA	Poly(methyl methacrylate)
SDS	Sodium dodecyl sulfate
SilF7	Fluorinated silane: 1H,1H,2H,2H-Perfluorooctyltriethoxysilane
Tris	Tris(hydroxymethyl)aminomethane
TA	Tris-Acetate
TAE	Tris-Acetate-EDTA
TE	Tris-EDTA

1 Introduction

On small length scales, on the order of nanometers to microns, materials and liquid-like media show behaviors and structures that are not observed in the macroscopic world. Viscous media and low Reynolds numbers lead to different hydrodynamic behaviours, and microstructural heterogeneities are observable in media that might seem homogeneous on dimensions of everyday materials and objects. In liquid-like media, thermal motion leads to diffusion of species ranging from molecules to nanoparticles. This movement is not only dependent on the temperature, viscosity of the medium, and size of the diffusing species, but also the structure of the environment. Measuring the diffusion of well-characterized nanoparticles can therefore serve as a method to evaluate material properties on the nanometer to micron scale, including biologically relevant systems with a complex microstructure, as shown in the context of this thesis.

In the first part of this thesis, diffusion is used to detect the presence of DNA. Characteristic DNA biomarkers hold a key position for the diagnostics of microbial or viral infections, genetic diseases, as well as antibiotic resistance.[1–5] The commonly used PCR method[3,6–16], followed by optical readout, is based on amplification of the analyte DNA to the nanomolar range, which suffers from long processing times of around 45 minutes to one hour.[9,11,15] Alternative methods often require high sample concentrations[17–33], long incubation or experimental times[34–45], or are based on complex experimental procedures[46–56].

In chapter 4, a different method to sense analyte DNA is presented that is based on measuring the diffusion of a nanosensor which can bind DNA. DNA origami structures with a precisely defined size show size changes in the presence of the biomarker DNA, such that diffusion measurements of the origami can serve as a tool to detect the presence of analyte DNA. A significant change in size is obtained by connecting two DNA origami nanosen-

sors via the analyte. Nanosensors with overhanging DNA strands are fabricated, that are complementary to one half of the analyte strand. Fluorescence Nanoparticle Tracking Analysis (NTA-FL) is used for precise measurements of the diffusion coefficients. It permits the detection of picomolar concentrations of DNA nanoparticles. Only a few minutes are needed to track enough particles to obtain statistically relevant data. The proposed method therefore allows for sensing of an analyte DNA at picomolar concentrations in only a few minutes.

In the second part of the thesis, the microstructure of a complex medium is investigated by means of diffusion. Understanding diffusion mechanisms and behaviour of nanoparticles in soft, heterogeneous media is of importance to understand transport in complex media like biological or artificial hydrogels.[57–59] Hydrogel-like systems are part of the extracellular matrix or the vitreous humor, to name a few examples.[60–62] Natural and synthetic hydrogels consist of a three dimensional network of polymers that is able to incorporate large amounts of water. The different polymers and crosslinking mechanisms permit their use in biomedical, biotechnological, or pharmaceutical applications or for catalysis.[63–68] Nanoparticles located in a polymer network are affected in their diffusion due to steric hindrance, hydrodynamic drag, or polymer-solute interactions.[69–74] To investigate their three-dimensional diffusion processes in different media, optical methods like Fluorescence Correlation Spectrocopy or Fluorescence Recovery After Photobleaching are often employed.[75–85] However, a limited optical penetration depth in opaque or complex media, and the need for fluorescent particle labeling, which can suffer from photobleaching, limit their effectiveness in hydrogels.[86,87]

Chapter 5 shows that the diffusion of nanoparticles of around 200 nm in size can be investigated by Pulsed Field Gradient Nuclear Magnetic Resonance (PFG NMR), if the nanoparticles exhibit a liquid core that provides an 'NMR active' signal. PFG NMR offers non-invasive, direct and absolute measurements of the diffusion coefficient of a large ensemble of spins in bulk, without the need for a fluorescent label. If the particles are leak-tight, so that the liquid is trapped inside the shell, the long-time displacement of the liquid molecules is mostly dependent on the movement of the whole particle and therefore mirrors the diffusion coefficient of the particle. This allows for diffusion measurements of the particles in liquid-like media, as well as in the complex microstructure of hydrogels. Diffusion can be used to draw conclusions on the mesh size of the hydrogel, using the

particles as diffusion nanosensors to investigate their environment. While PFG NMR has been used to measure the diffusion of molecules in complex media,[73,74,88–96] nanoparticles on the order of tens to hundreds of nanometers have not been investigated in complex media by PFG NMR before. Although the idea of using particles with a liquid core is not new[97–106], to the best of my knowledge there is no previous study that allows for non-invasive diffusion measurements of liquid filled particles in complex media. The presented method supports the examination of structural properties of complex media, like an estimation of the mesh size in hydrogels, in a size range and under conditions that are not easily accessible by other methods.

Published Work

The work presented in this thesis has been conducted in the research group Micro Nano and Molecular Systems at the Max Planck Institute for Intelligent Systems (Stuttgart) and later in the same group at the Max Planck Institute of Medical Research (Heidelberg). The main results of this thesis have been either submitted or are being prepared for submission to be published:

- Ida Bochert, Jan-Philipp Günther, Izar Schärf, Erik Poppleton, Kerstin Göpfrich, Mariana Alarcón-Correa, and Peer Fischer. "DNA Detection with Origami Diffusion Nanosensors", *submitted 2025*
- Ida Bochert, Camila Vacas Betancourt, Dimitris Missirlis, Nicolás Moreno-Gómez, and Peer Fischer. "Absolute Measurement of Nanoparticle Diffusion Using 19F PFG NMR in Complex Media", *in preparation*

In addition the author has contributed to the following publications

- Jessie Levillain, François Alouges, Antonio Desimone, Akash Choudhary, Sankalp Nambiar, Ida Bochert. "A bi-directional low-Reynolds-number swimmer with passive elastic arms." 2024. DOI: 10.48550/arXiv.2403.10556.
- Ida Bochert, Jan-Philipp Günther, Peer Fischer, and Günter Majer. "Diffusion mechanisms of DNA in agarose gels: NMR studies and Monte Carlo simulations". In: The Journal of Chemical Physics 156.24 (2022), p. 245103. ISSN: 0021-9606. DOI: 10.1063/5.0092568.

2 Theory

This chapter outlines the theoretical background for the work presented in the following chapters. Principles of diffusion mechanisms in low Reynolds number systems are introduced in section 2.1, as well as the behaviour of particles in confined spaces. While diffusion of nanoparticles as a tool to sense their environment is a relevant concept throughout the entire thesis, the special case of confined spaces is addressed in chapter 5. Section 2.2 gives an overview of the used measurement techniques. A detailed introduction to the basics of PFG NMR is presented, as this method is used in chapter 5 to measure the diffusion of nanoparticles in liquid-like and complex media non-invasively and without the need of optical labeling. Further, methods for size measurements by optical detection of nanoparticles are presented. While NTA and Dynamic Light Scattering (DLS) are used in both chapters 4 and 5, the special method of NTA-FL is applied in chapter 4 to measure the diffusion of DNA origami.

2.1 Hydrodynamics at low Reynolds Number

The field of hydrodynamics ranges from swimming of bacteria under laminar flow conditions[107] up to turbulent environments like in a natural river.[108] The behaviour of an object placed in hydrodynamic system is highly dependent on the so-called Reynolds number Re, which defines the ratio of inertial to viscous forces. It is defined as

$$\mathrm{Re} = \frac{\text{inertial forces}}{\text{viscous forces}} = \frac{\rho u L}{\eta}, \tag{2.1}$$

and therefore dependent on the density ρ and viscosity η of the fluid, as well as the velocity u and size L of the object. While for high Reynolds number, inertial forces are dominant, they are negligible in the case of low Reynolds number systems. For

hydrodynamics at the nano- or microscale, the small characteristic size L and velocity u of the moving objects leads to low Reynolds numbers. A main transport mechanism in these systems is diffusion, which will be outlined in the following.[107,109]

2.1.1 Diffusion in Homogeneous Media

Diffusion is of importance in our everyday life as it helps our body in a medical context to transport drugs into tissue, or supplies our cells with nutrients and oxygen.[110–112] The diffusive transport of particles is described by random Brownian motion, such that a particle performs a random walk based on collisions with surrounding molecules.

If we put sugar to our tea, or salt into a soup, a concentration gradient is generated. As described by Fick's second law,

$$\frac{\partial c(\boldsymbol{r},t)}{\partial t} = D\nabla^2 c(\boldsymbol{r},t), \tag{2.2}$$

the concentration $c(\boldsymbol{r},t)$ of sugar molecules or salt ions changes over time to generate a uniform distribution of particles. This process is controlled by the concentration gradient and the (isotropic) diffusion coefficient D, which is dependent on the given system, and describes how fast the diffusing species spreads out, which is known as *mutual diffusion*. However, diffusion does not only take place in the presence of a macroscopic concentration gradient, but it is a continuous process. Thermal energy provided by the system causes the molecules or particles to continuously perform Brownian motion. This process is called *self-diffusion* and was first explained by Albert Einstein. In the context of this thesis, self-diffusion is investigated. The term 'diffusion' therefore refers to self-diffusion.[113,114]

Einstein derived a mathematical model of self-diffusion by considering the conditional probability $P(x_0|x_1,t)\mathrm{d}x$. It describes the probability that a diffusing particle, that starts at the position x_0 at a time $t = 0$, can be found at x_1 at time t. It is a Markovian property, which means that $P(x_0|x_1,t)\mathrm{d}x$ is not dependent on the behaviour of the considered particle before $t = 0$. The three dimensional conditional probability density $P(\boldsymbol{r}|\boldsymbol{r'},t)$ can be shown to follow Fick's law (2.2). Using the initial condition $P(\boldsymbol{r}|\boldsymbol{r'},0) = \delta(\boldsymbol{r'}-\boldsymbol{r})$,

where $\delta(\boldsymbol{x})$ is the Dirac Delta distribution, the solution for Fick's law for diffusion in isotropic and homogeneous media using the conditional probability density is

$$P(\boldsymbol{r}|\boldsymbol{r'},t) = \frac{1}{(4\pi Dt)^{3/2}} \cdot \exp\left(-\frac{(\boldsymbol{r'}-\boldsymbol{r})^2}{4Dt}\right). \tag{2.3}$$

This result shows a Gaussian distribution around the starting point $\boldsymbol{r}$ that flattens and broadens with increasing time. This shows the behaviour of an ensemble of diffusing species: If hypothetically all particles started at the same point $\boldsymbol{r}$, their locations after time t will be distributed around r in a Gaussian form.[113,115–117]

An important result from equation (2.3) is the mean squared displacement (MSD) $\langle r^2 \rangle$ that a diffusing species will cover in a given diffusion time Δ. It is dependent on the number of dimensions of movement d as

$$D = \frac{\langle r^2 \rangle}{2d\Delta}. \tag{2.4}$$

For the case of free diffusion, the MSD is proportional to the diffusion time. The square-root of the MSD $\sqrt{\langle r^2 \rangle}$ can be the understood as a scale for the mean covered distance within the diffusion time Δ.[113,115–117]

Since a diffusion process is based on collisions with surrounding molecules, it has to be dependent on the movement of the molecules, and hence on the thermal energy present in the system. In analogy to an ideal gas, Einstein derived a mathematical description of this relationship based on minimizing the free energy for a small displacement of the particles.[116] He found that the diffusion coefficient

$$D = \frac{k_\mathrm{B}T}{\zeta} \tag{2.5}$$

is dependent on the friction ζ and the thermal energy, given by the Boltzmann constant k_B, multiplied with temperature T. Choosing the Stokes drag $\zeta = 6\pi\eta R$, which describes the friction that a spherical particle of radius R experiences in a medium of viscosity η, he obtained

$$D = \frac{k_\mathrm{B}T}{6\pi\eta R}. \tag{2.6}$$

This relation is used in the case of spherical particles. However, for non-spherical particles, as well as hydrated particles, the radius R can be replaced by the hydrodynamic radius R_h, which describes the radius of a sphere that is diffusing with the same speed as the given particle. Interestingly, around the same time as Einstein, William Sutherland found the same result.[118] Eq. (2.6) is therefore known as the Stokes-Einstein-Sutherland (SES) equation.[113,116–118]

2.1.2 Diffusion in Confined Spaces

While the equations derived above apply for diffusion in homogenous liquids, the case of diffusion inside a complex environment becomes more complicated. It has been discussed in the literature, which the following section is based on.[113,117,119] In polymer networks like a hydrogel, the gel fibres create local inhomogeneities that can hinder the diffusion of solutes. There are many different models for diffusion of nanoparticles of different size and shape in hydrogels or polymer solutions of different volume fractions. For a detailed discussion, the reader is referred to the literature.[69–74] However, the case of nanoparticles completely trapped inside a cavity is of interest in the context of this thesis. As shown in figure 2.1, the diffusion coefficient becomes apparently dependent on the diffusion time.

On a very short timescale, the particles will perform free and unhindered diffusion inside the porous hydrogel structure. Only a small number of them will move far enough in the given time to touch the obstructing gel fibres and be repelled by them. In this regime, the apparent (i.e. measured) diffusion coefficient is comparable to the free, unhindered diffusion coefficient D_0. For increasing diffusion time, more particles will perceive the steric restrictions by the gel, which leads to a smaller covered distance than the particles would perform without the gel. Considering the diffusion time, the measured diffusion coefficient of the particles will now be smaller than for unhindered diffusion. Is has to be noted that the particles are not diffusing slower on the nanoscale, but appear so, due to the reduced covered distance in the given diffusion time. The diffusion coefficient that is measured in this case is therefore referred to as an ‘apparent diffusion coefficient’.

For the long-term limit, two different cases have to be considered. In some gels, the particles can be assumed to be hindered by the gel fibres, but can randomly pass them and move on to another part of the mesh, denoted as a pore in the following. The

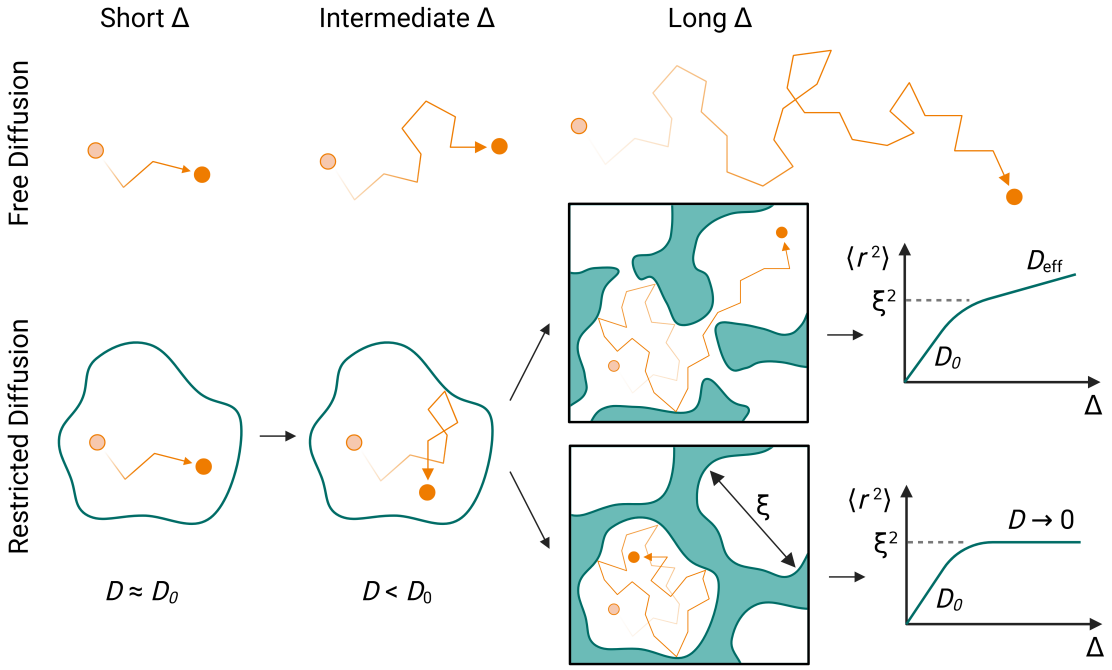

Figure 2.1: Diffusion behaviour of nanoparticles in absence (top) or presence of obstacles (bottom). The columns represent different regimes of the diffusion time Δ. While for free diffusion, the particles move unhindered for any Δ, in the case of restricted diffusion the MSD $\langle r^2 \rangle$ scales no longer linear with Δ. Instead, for short Δ, the diffusion seemes to be nearly unhindered, while for increasing diffusion time, the movement is slowed down due to interactions with the obstacles. For the case of long Δ, the diffusion coefficient D can either tend to an apparent D_{eff} for a slow movement from one 'pore' to another, or the particles can be trapped inside a cavity, leading to $D \to 0$. The average pore size is denoted as ξ. Created with BioRender.com. Image adapted from P. Callaghan[113] and W. Price[117].

observed long-term diffusion coefficient will then cover the motion from one pore to another. For long diffusion times, the diffusion coefficient converges to the long-term, hindered diffusion coefficient of the particles in the mesh. The MSD, which normally shows a linear dependence on the diffusion time according to Eq. (2.4) shows two regions. In the short-term limit, the slope is comparable to the case of free diffusion, and reduces to a smaller increase for the long-term diffusion.

In the second case, the particles can be assumed to be completely trapped inside a pore. This leads to a covered distance independent from the diffusion time. When increasing the time, the particles will therefore appear to move slower. This can be observed as a plateau in the plot of the MSD over diffusion time. The value of the plateau is on the order of magnitude of the squared pore diameter ξ. A constant MSD with increasing diffusion time corresponds to an apparent diffusion coefficient that will tend to zero. From the time-dependent behaviour of the diffusion coefficient, conclusions can therefore be drawn on the structure of the medium.[113,117]

For the special case of diffusing particles trapped inside a spherical cavity, a model has been reported in the literature, that estimates the mesh size from PFG NMR measurements for the long-term diffusion coefficient and the condition of small q values, where q defines measurement-dependent parameters as discussed in section 5.4.2. The model assumes that the position of a particle will no longer be dependent on the starting position, so the probability that the particle is located at a certain position inside the cavity is only dependent on the density distribution in the cavity. This leads to

$$D = \frac{a^2}{5\Delta}, \tag{2.7}$$

where a is the radius of the spherical pore.[113,120–122]

2.2 Diffusion Measurement Techniques

Different methods for diffusion measurements of nanoparticles are presented in the following. To explain PFG NMR, some basics about NMR are presented, as well a description of the procedure of diffusion measurements. After that, the case of polydisperse nanosen-

sors is outlined. Subsequently, some light based methods are introduced, namely NTA, NTA-FL and DLS.

2.2.1 Pulsed Field Gradient Nuclear Magnetic Resonance

Nuclear magnetic resonance (NMR) is a method based on the generation and measurement of nuclear spin transitions in magnetic fields. Individual spins are highly sensitive to their environment, hence NMR allows for drawing conclusions on molecular structure and other interactions between nuclear spins and their surroundings. NMR plays an important role in the structural investigation of organic molecules containing hydrogen atoms. In general, however, any nucleus having a nuclear spin can be studied using nuclear magnetic resonance.

Apart from structural analysis, a more advanced method of NMR is used here, which is the so-called Pulsed Field Gradient (PFG) NMR. It allows for observation of the diffusion of spin-attached particles. Compared to other diffusion measurement techniques like Fluorescence Correlation Spectrocopy, Fluorescence Recovery After Photobleaching or DLS, it allows for diffusion measurements without the need of fluorescent labeling and without being affected by optical properties of the sample.[123] It is non-invasive and works in bulk media. It further offers the advantage of an ensemble measurement. An absolute diffusion coefficient can be measured without the need for a model.[113,117]

Basic Theory of Nuclear Magnetic Resonance

Understanding the basic principles of NMR is essential for the interpretation of NMR experiments and their use in diffusion experiments. NMR can be performed on various atomic nuclei, whereof hydrogen ^{1}H, carbon ^{13}C, fluorine ^{19}F, or phosphorus ^{31}P are some of the most investigated 'NMR active' nuclei. They all show a nuclear spin of $I = 1/2$, which is needed for performing NMR experiments, as will be shown in the following.[110,124]

Zeeman Effect While a spin $\boldsymbol{I}$ cannot be measured directly, its associated magnetic moment $\boldsymbol{\mu}$ can be investigated experimentally. It is given by

$$\boldsymbol{\mu} = g_{\mathrm{I}} \frac{\mu_{\mathrm{I}}}{\hbar} \cdot \boldsymbol{I} = \gamma \cdot \boldsymbol{I}, \tag{2.8}$$

where the magneton $\mu_{\mathrm{I}} = \hbar e / 2m_{\mathrm{p}} \approx 5.05 \cdot 10^{-27}\,\mathrm{J/T}$ and the g factor can be merged yielding the gyromagnetic ratio γ. Values of the gyromagnetic ratio of the two nuclei used in the context of this thesis are $\gamma_{^1\mathrm{H}} = 26.75 \cdot 10^7\,1/\mathrm{Ts}$ and $\gamma_{^{19}\mathrm{F}} = 25.18 \cdot 10^7\,1/\mathrm{Ts}$.[125] Due to the different values of the gyromagnetic ratio, the magnetic moment induced by a spin is not only dependent on the nuclear spin, but also on the type of nucleus.[126]

If a nuclear spin is placed in a constant, homogeneous magnetic field such as $\boldsymbol{B}_0 = (0,0,B_0)^{\mathrm{T}}$, the energy provided by the magnetic field causes the spins states, that were degenerated before, to shift in energy. This is called Zeeman effect. For a $I = 1/2$ system, it leads to the presence of two energy levels $m_{\mathrm{I}} = \pm 1/2$, which are separated by the energy $\Delta E = \gamma \hbar B_0$. These spin states are often denoted as 'spin up' and 'spin down' states. The occupation of this system without external perturbation is described by a Boltzmann distribution.[127,128]

In presence of the constant magnetic field $\boldsymbol{B}_0$, the spins will further start precessing around the axis given by the direction of the magnetic field. This rotation is called Larmor precession and shows the Larmor frequency[127,128]

$$\omega_{\mathrm{L}} = \gamma \cdot B_0. \tag{2.9}$$

Chemical Shift Considering the local environment of a nuclear spin inside a sample, the precession frequency changes by small contributions to the local magnetic field. A nuclear spin, that is part of a molecule, experiences small changes in the local magnetic field caused by the structure of the molecule. The applied external magnetic field induces a current in the electronic system of the molecule, which causes an additional magnetic moment. It shields the external magnetic field depending on the electronic structure. This is represented by the *chemical shift*

$$\delta = \frac{\omega_i - \omega_{\mathrm{ref}}}{\omega_{\mathrm{ref}}} \cdot 10^6, \tag{2.10}$$

which defines the frequency shift of sample i with respect to a standard frequency ω_{ref} in parts per million (ppm). For a detailed discussion of the chemical shift, the reader is referred to the literature.[129–131]

Magnetic resonance Upon providing energy in form of an electromagnetic wave, the spins can be 'flipped' between the two states. This happens when the wave satisfies the resonance condition

$$E = hf = \gamma \hbar B_0. \tag{2.11}$$

In a magnetic field of $B_0 = 9.4\,\mathrm{T}$, as used in the context of this thesis, the required frequency for hydrogen resonance is therefore around $f = 400\,\mathrm{MHz}$.[128]

A high frequency magnetic field of amplitude B_1 and frequency ω_{L} perpendicular to $\boldsymbol{B}_0$ provides the energy for spin-flips in an NMR experiment. The duration of applying the $\boldsymbol{B}_1$ field decides on the number of spins that are lifted to the higher energy level.[125]

While the magnetic moments generated by individual spins are very weak, the macroscopic property of the magnetization $\boldsymbol{M}$ is easily accessible. It is defined as the sum of all magnetic moments of the individual spins in the given volume V as

$$\boldsymbol{M} = \frac{1}{V} \sum_i \boldsymbol{\mu}_i. \tag{2.12}$$

By applying a $\boldsymbol{B}_1$ pulse, the individual spin-flips lead to a turn of the magnetization into the xy plane or – if the pulse is longer – to a total flip of the magnetization into negative z direction. These pulses are denoted as $\pi/2$ and π pulse, respectively.[129]

Turning the magnetization into the xy plane allows for measuring its precession frequency by induction in a measurement coil. Signals of different species with their own, slightly different, precession frequencies are included in the overall magnetization. Doing a Fourier transform reveals a spectrum that shows the different species at different chemical shifts. The intensity of each peak is dependent on the number of chemically equivalent spins that contribute to the peak. These NMR spectra give valuable insight into the chemical structure of the molecules contained in a sample. However, this describes an ideal case without energy loss processes. In a real NMR experiment, the

magnetization with respect to the time will not only show a precession, but also a decay. The signal induced in the coil, that it used for calculating an NMR spectrum is therefore called free induction decay (FID). Due to the relaxation, the peaks representing each chemical species show a distribution of non-zero linewidth.[125,128–130]

Relaxation times To discuss the processes of energy loss present in an NMR experiment qualitatively and quantitatively, the Bloch equations are considered. Besides the Larmor precession presented by $\mathrm{d}\boldsymbol{M}/\mathrm{d}t = \gamma \boldsymbol{M} \times \boldsymbol{B}$, different relaxation processes are introduced by the Bloch equations. They include time constants that describe after which time the system is relaxed into its ground state after it was disturbed. The full set of Bloch equations reads

$$\frac{\mathrm{d}\boldsymbol{M}}{\mathrm{d}t} = \gamma \boldsymbol{M} \times \boldsymbol{B} - \begin{pmatrix} M_x/T_2 \\ M_y/T_2 \\ (M_z - M_0)/T_1 \end{pmatrix}. \tag{2.13}$$

It introduces the *longitudinal relaxation time* T_1, also called *spin-lattice relaxation time*, which gives the characteristic time of the relaxation of the magnetization in the direction of the applied magnetic field to reach the equilibrium state M_0. It is caused by energy exchange with the environment, like a surrounding crystal lattice. It can be measured using the Inversion-Recovery (IR) technique, where a $\pi/2$ pulse is applied after a π pulse to force the recovery of magnetization following

$$M_z = M_0 \left(1 - 2 \cdot \exp\left(-\frac{t}{T_1}\right)\right). \tag{2.14}$$

Further, equation (2.13) introduces the *transverse relaxation time* T_2, also denoted as the *spin-spin relaxation time*. It gives the time frame of dephasing effects of the spins due to interaction of the spins among each other. It describes an irreversible decay of the measured magnetization. Further, local inhomogeneities lead to a reversible dephasing on the time scale T_2', which is included in an effective transverse relaxation time T_2^*, given by $(T_2^*)^{-1} = (T_2)^{-1} + (T_2')^{-1}$. It defines the decay of the FID and is therefore related

to the linewidth of the corresponding peak. The peaks in an NMR show the form of a Lorentz curve. Their full width at half maximum (FWHM) therefore follows[132]

$$T_2^* = \frac{2}{\Delta\omega} = \frac{1}{\pi \cdot \Delta f}, \tag{2.15}$$

where $\Delta\omega$ and Δf describe the linewidth at the half maximum for the angular velocity and the frequency, respectively. While the effect of the T_2 time cannot be prevented in an NMR experiment due to its irreversible character, the reversible effect of the local magnetic inhomogeneities can be minimized by performing a spin echo experiment as discussed below.[127,128,130,132,133]

In solids, very short relaxation times are observed due to anisotropic direct dipol-dipol interaction. While in liquids, the motion of the individual spins leads to an averaging of the anisotropic interactions, this is not possible for solids. The short relaxation times lead to inhomogeneous broadening of the peaks in the NMR spectrum, which makes the case of solid state NMR more difficult compared to liquid NMR.[127–129,134,135]

Spin Echo To eliminate the reversible effect of dephasing due to local magnetic field inhomogeneities, a spin echo pulse sequence can be applied. It is used to measure the transverse relaxation time T_2 without the effect of T_2'. A $\pi/2$ pulse is applied to turn the magnetization into the xy plane. After a given time τ, during which the spins dephase due to the transverse relaxation T_2 and the reversible dephasing mechanisms T_2', a π pulse is applied. It leads to a 180° flip, so that the spins appear to experience the local inhomogeneities flipped by 180°. This leads to a rephasing of the spins. After time 2τ, the effect of the reversible dephasing is cancelled and an NMR signal can be measured, which is called the spin echo. Its intensity is reduced by only the irreversible effects of the transverse relaxation T_2. By measuring different values of τ, the T_2 relaxation time can be observed using

$$M_x(2\tau) = M_0 \cdot \exp\left(-\frac{2\tau}{T_2}\right). \tag{2.16}$$

While this method is often denoted as the Hahn spin echo experiment, Hahn[136] used different pulse sequences. However, he was the first to observe and describe the mechanism of spin echoes.[113,117,128,130,132,136,137]

For the case of diffusion measurements, which will be discussed below, a long observation time is desirable. This can be obtained by splitting the π pulse into two separate $\pi/2$ pulses, which is denoted as a stimulated echo pulse sequence. In the time between these two, only the longitudinal relaxation is active, while for a spin echo sequence, transverse relaxation is present all the time. Since the relaxation times in many materials fulfill $T_2 \ll T_1$, the stimulated echo is beneficial for diffusion measurements or other setups, where long observations times are needed.[113,122]

PFG NMR

The concept of PFG NMR is well described in the scientific literature.[117,119,138–140] An overview based on these references is given in the following.

To be able to measure diffusion using a NMR based method, the spins need to be labeled by their position in the sample. If this can be achieved, the MSD between their initial positions and the position after a given diffusion time Δ can be used to calculate the diffusion coefficient. The labeling of the z position of the particles is done by applying a magnetic gradient pulse collinear with the $\boldsymbol{B}_0$ field, $\boldsymbol{g} = (0,0,g)^{\mathrm{T}}$. For the short time period of the gradient pulse, the spins precess faster or slower dependent on their position according to $\omega_{\mathrm{L}} = \gamma(B_0 + g \cdot z)$. This leads to a systematic, position-dependent phase shift.

The simplest case of a diffusion pulse sequence based on a spin echo experiment is shown schematically in figure 2.2a. This pulse sequence is called Stejskal-Tanner pulse sequence and will be denoted later as *diffSe* sequence. The two $\boldsymbol{B}_1$ pulses, shown in blue, lead to a $\pi/2$ turn of the magnetization at $t = 0$ and an inversion by a π pulse at $t = \tau$ (see figure 2.2b). After time $t = 2\tau$, the spin echo is measured, which is reduced by effects of the transverse relaxation time. Additionally, two magnetic field gradient pulses of strength g and length δ_{g} are shown in green. They are applied at time $t = t_1 > 0$ and $t = t_1 + \Delta$. Due to the inverting π pulse, the spins experience the second gradient pulse as if it was oriented in the opposite direction than the first gradient pulse.

The effect of the two gradient pulses is shown in figure 2.2c and 2.2d. Before the first gradient is applied, the magnetization was flipped to the xy plane. This is presented here as a co-rotating coordinate system $x'y'$. At time $t = t_1$, the first gradient generates a

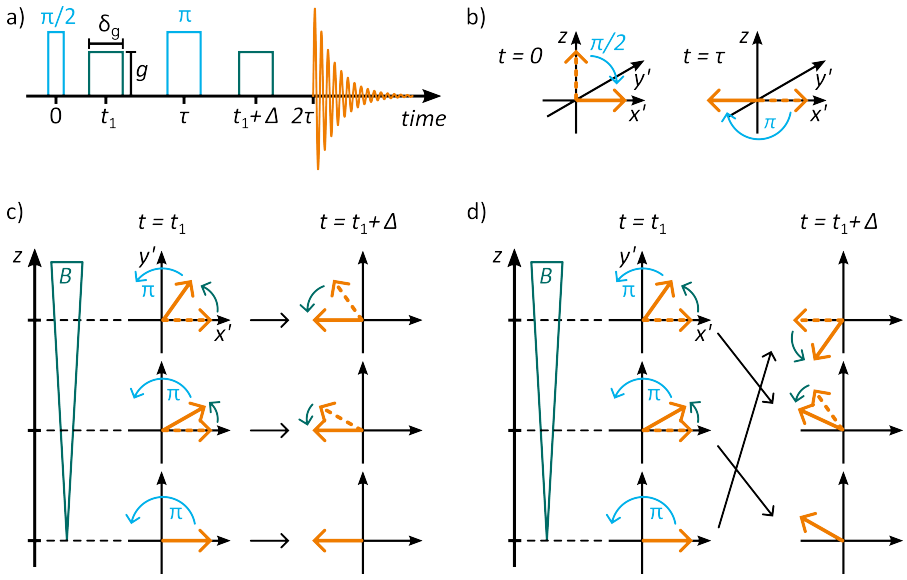

Figure 2.2: Explanation of the method used in PFG NMR measurements. a) Stejskal-Tanner pulse sequence used for diffusion measurements based on a spin echo experiment. $\boldsymbol{B}_1$ pulses are shown in blue, gradient pulses are green. After applying a $\pi/2$ pulse at $t = 0$, and a π pulse at $t = \tau$, a spin echo (depicted in orange) can be measured at $t = 2\tau$. The gradient pulses allow for diffusion measurements. b) Behaviour of the magnetization, shown in orange, when applying the $\boldsymbol{B}_1$ pulses. The axes x' and y' denote a coordinate system that is co-rotating with the Larmor frequency. c) and d) Impact of the gradient pulses on a system without (c) and with (d) diffusion in z direction, as indicated by black arrows. Each row shows a spin located at different z coordinates. When applying the gradient pulse, they obtain a phase shift depending on their position (shown in green). Without diffusion, the π pulse together with the second gradient pulse lead to a rephasing. In the case with diffusion the spins change their position, which causes a incomplete rephasing. Image adapted from W. Price[117].

phase shift of the spins, depending on their z position. This is followed by the π pulse. If the spins are static at their z position (figure 2.2c), the second gradient at $t = t_1 + \Delta$ leads to a rephasing of the spins. However, if diffusion causes a change in position (figure 2.2d), the second gradient leads to an incomplete rephasing, which results in an attenuation of the intensity of the magnetization, and therefore to a loss in NMR signal intensity. The attenuation of the NMR signal of a specific chemical component, represented by the area under the peak in the NMR spectrum, is therefore dependent on the diffusion of this species (represented by the average change in z position $z(t = \Delta) - z(0)$ of the spins), as well as the gradient strength and length g and δ_g, and the diffusion time Δ. By recording NMR spectra for different gradient strengths, the diffusion coefficient of a chemical component can therefore be obtained from the attenuation of the corresponding peak in the NMR spectrum.

A mathematical description of the spin system in the case of diffusion is given by the Bloch-Torrey equations. A diffusion term $D\nabla^2\boldsymbol{M}$ is added to the right-hand side of the Bloch equations (2.13). It is obtained from Fick's second law, as shown in equation (2.2) and holds for isotropic diffusion. Solving the Bloch-Torrey equations leads to a attenuation of the NMR signal intensity following

$$I(b) = I_0 \cdot \exp(-b \cdot D), \tag{2.17}$$

where the diffusion weighting parameter b contains the diffusion time Δ, the gradient length δ_g, the gradient strength g, and the gyromagnetic ratio of the considered nucleus. For sinusoidal gradient pulses of length δ_g, the parameter b is given as[141,142]

$$b(g) = \gamma^2 g^2 {\delta_\mathrm{g,eff}}^2 \left(\Delta - \frac{\pi}{8}\delta_\mathrm{g,eff}\right). \tag{2.18}$$

The effective gradient length for a sinusoidal gradient pulse is given by $\delta_\mathrm{g,eff} = 2\delta_\mathrm{g}/\pi$, and the factor I_0 in equation (2.17) contains relaxation effects, as well as the intensity of the magnetization without perturbation. When measuring the NMR intensity for fixed values of Δ and $\delta_\mathrm{g,eff}$, the relaxation terms show the same value and can therefore be treated as a constant. By varying the gradient strengths g and fitting equation (2.17) to the resulting NMR intensities, the diffusion coefficient D of the considered chemical species can be obtained.[117,138–140]

For the case of $T_1 > T_2$, as assumed for all diffusion measurements in the context of this thesis, the *diffSte* sequence can be applied. It is based on a stimulated echo sequence, where the π pulse of the spin echo sequence is split into two $\pi/2$ pulses. As they are applied shortly after the first, and before the second gradient, they flip the magnetization into the negative z direction for the time period in between. This reduces relaxation effects to the longitudinal relaxation instead of the transverse relaxation. The experimentally accessible diffusion time is therefore no longer limited to the transverse, but to the (longer) longitudinal relaxation time T_1.[122,143]

PFG NMR on polydisperse particles

The mean diffusion coefficient of different chemical species can be measured by PFG NMR as shown above. However, fitting the intensity attenuation using equation (2.17) is only reasonable for a single diffusion coefficient. If a sample contains two species of the same chemical shift, but different diffusion coefficients, a bi-exponential decay can be fitted to the NMR intensity attenuation.[96,99,144] However, the evaluation becomes more difficult if the diffusion of polydisperse particles is to be evaluated. Looking at an ensemble of polydisperse particles, the measurements should give not only a single diffusion coefficient, but a distribution of diffusion coefficients. In this case, equation (2.17) can be integrated over all diffusion coefficients, which yields

$$I(b) = I_0 \cdot \int_0^\infty P(D) \exp(-bD) \mathrm{d}D. \tag{2.19}$$

The gamma distribution model $P(D; \kappa, \theta)$ has been shown to give results that are comparable to a log-normal distribution of diffusion coefficients and is therefore assumed to be a reasonable model for a distribution of diffusion coefficients of polydisperse nanoparticles.[145,146] The gamma distribution model follows

$$P(D; \kappa, \theta) = D^{\kappa-1} \frac{\exp(-D/\theta)}{\Gamma(\kappa)\theta^\kappa}. \tag{2.20}$$

Here, $\Gamma(x)$ is the gamma function, and κ and θ are shape and scale parameter, respectively. They follow $\theta = \sigma^2/\langle D \rangle$ and $\kappa = \langle D \rangle^2/\sigma^2$, where $\langle D \rangle$ is the mean self-diffusion coefficient and σ the standard deviation of the distribution. Different to the log-normal

distribution, the gamma distribution as given in equation (2.20) is analytically solvable for the case of a PFG NMR intensity attenuation. Equation (2.19) then becomes

$$I(b) = I_0(1 + b\theta)^{-\kappa} = I_0 \left(1 + \frac{\kappa\sigma^2}{\langle D \rangle}\right)^{-\langle D \rangle^2/\sigma^2} . \tag{2.21}$$

By fitting equation (2.21) to the intensity attenuation obtained in a PFG NMR experiment, the fitting parameters κ and θ can be used to calculate the distribution of diffusion coefficients $P(D)$, and the mean and standard deviation of the diffusion coefficient.[145]

2.2.2 (Fluorescence) Nanoparticle Tracking Analysis

Nanoparticle Tracking Analysis (NTA) is a fast and sensitive method to measure the size and concentration of nanoparticles suspended in a liquid. Multiple particle tracking is used to measure the diffusion of the nanoparticles, from which a PSD can be deduced. NTA allows for the investigation of particles in a size range of around 20 nm to 1 µm. The lower limit is dependent on the particle properties and the settings of the used system. Low particle concentrations of down to picomolar suspensions can be detected, which makes NTA a very sensitive method for the determination of particle size and concentration.[147,148]

The setup used for NTA is depicted in figure 2.3a. The particle suspension is filled into a flow chamber, and can be either measured in a static state, or using a well-defined flow speed. A laser sheet is used to illuminate the particles present in a horizontal plane. These scatter the light, which is then captured by a camera, equipped with a microscope. The particles appear on the camera as broad, but well separated light spots, allowing for real-time visualisation of the suspension. A snapshot of a captured image in the software *Nanosight NTA 3.4* is shown in figure 2.3b. The bright spots, marked with a blue or red cross, represent the scattered light of one particle, each. A video of the particle diffusion is recorded and their tracked positions are evaluated to obtain the MSD of each particle. According to equation (2.4), the distance covered in a given time by diffusion is proportional to the diffusion coefficient. This value, in turn, is directly related to the hydrodynamic radius as given in equation (2.6). For a known temperature and viscosity, the hydrodynamic radius for each particle is obtained. A histogram of the numbers

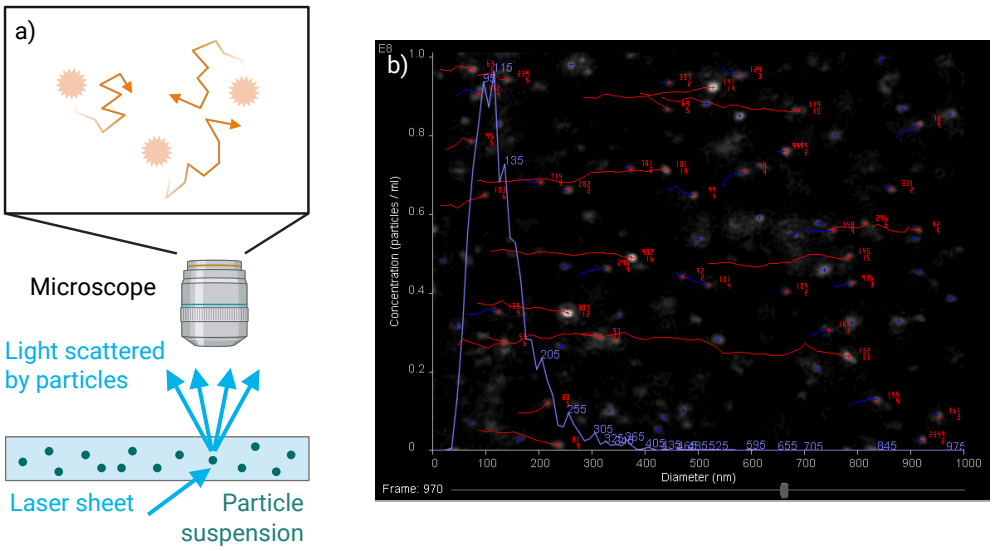

Figure 2.3: Principle of size measurement by NTA-FL. a) Schematic representation of the setup used for NTA or NTA-FL. Particles are suspended in a liquid, which can be flushed through the flow chamber or investigated statically. The particle suspension is illuminated with a laser sheet, which scatters at the particles or excites fluorescence labels. The scattered or emitted light is captured by a camera, which is equipped with a microscope objective. A filter can be inserted in the path of the light to block unwanted wavelengths. Light spots appear at the videos, which represent one particle, each. The movement of each particle is tracked to obtain the diffusion coefficients, which in turn can be used to calculate the PSD. Created with BioRender.com. Image adapted from R. Dragovic et al.[150]. b) A snapshot of the software *Nanosight NTA 3.4*, measuring a 6HB origami sample stained with SYBR gold (see chapter 4). A 500 nm high-pass filter is used and flow is applied to prevent bleaching of the fluorophore. Tracked particles are shown in red, the blue line represents the PSD.

of particles with respect to their size yields the PSD. An exemplary evaluation by the software *Nanosight NTA 3.4* is shown as a blue line in figure 2.3b.[149,150]

For nanoparticles that produce a small scattering signal, a fluorescent dye can be used as in the case for DNA origami (see section 3.1), where a fluorophore can be added that intercalates into the DNA double helix. Using the same process as outlined above, the emitted light of the fluorophore molecules is captured to measure the diffusion coefficient of the individual particles. Using a dye that specifically stains the considered structure like a dsDNA further allows for a reduction of background noise caused by scattering on contaminants. This Fluorescence Nanoparticle Tracking Analysis will be referred to as NTA-FL in the context of this thesis. Since a fluorophore will bleach after some time,

it is important to use a light-shielded system. Further, the measurements need to be performed using flow that regularly replaces the particles in the illuminated and visible range. Knowledge of the flow speed is therefore important for the determination of the diffusion-based MSD.[148,150,151]

It is important to note that the methods of NTA and NTA-FL inherently measure a number-weighted particle size distribution.

2.2.3 Dynamic Light Scattering

A DLS setup uses a monochromatic light beam to illuminate a sample of suspended particles. The light is scattered at the suspended particles in all directions. The scattering intensity is detected at a chosen angle. The particles' diffusion causes fluctuations in the scattering intensity. The measured intensities are correlated to get the correlation function. This contains information about the diffusion coefficients of the diffusing species present in the sample. DLS can in principle be used for particles in a range of $< 1\,\mathrm{nm}$ to around $2\,\mu\mathrm{m}$.[123] It offers fast, low-cost, and non-invasive measurements that are not affected by treatment of the sample. However, the intensity of a Rayleigh scattering signal is proportional to the volume of the scattering object squared.[130] The measured PSD is weighted by the scattering intensity, and therefore values larger particles higher than smaller particles. Hence, the method is very sensible to dust, and requires assumptions to be made about the optical properties of the measured particles to calculate a number weighted particle size distribution.[123,152]

3 Methods

The diffusion coefficient of nanoparticles can give information about their environment. To be able to measure the diffusion precisely, not only the choice of a measurement method is essential, which has been discussed in chapter 2. Also the selection of a suitable diffusion nanosensor that fits the method and fulfills further requirements regarding size, structure, or the possibiliy of surface modifications is of great importance. In the context of this thesis, two different nanoparticles are used as diffusion sensors, namely DNA origami, which is the focus of chapter 4, and oil-filled core-shell particles, which allow for diffusion measurements by NMR as discussed in chapter 5. The fabrication of both types of nanosensors is presented in this chapter.

3.1 Folding of DNA Origami

Deoxyribonucleic Acid (DNA) is a linear polymer made up of four different monomers, called nucleotides. Each nucleotide consists of a sugar and a phosphate group, building the 'backbone' of the DNA, and a characteristic nucleobase. Connecting several nucleotides allows for the formation of a single stranded DNA (ssDNA). It carries a negative charge due to the oxygen atom in the phosphate group, therefore causing DNA to be negatively charged. The ends of a ssDNA strand are labeled as 5' (phosphate group) and 3' (sugar) ends.[110]

The four different nucleobases are adenine (A), thymine (T), guanine (G), and cytosine (C). Adenine and guanine are derivatives of purine, meaning that they show two aromatic rings, while thymine and cytosine are derivatives of pyrimidine, showing one aromatic ring. Each two of the nucleobases are complementary (A/T and C/G) towards each other. The base complementary permits binding of the nucleobases by hydrogen bonds.

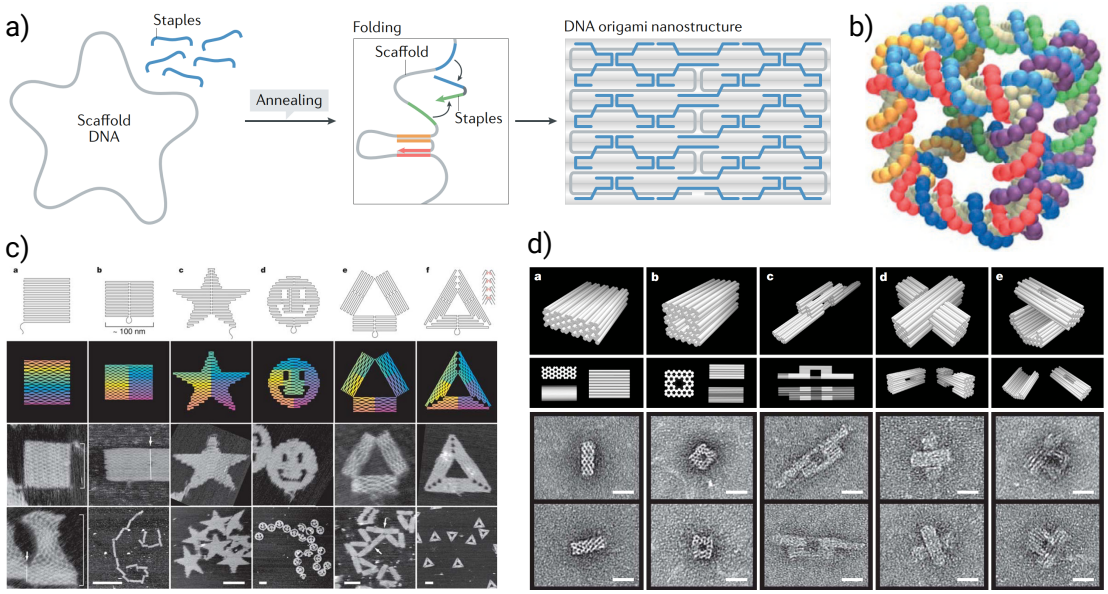

Figure 3.1: Fabrication mechanism and possible shapes of DNA origami. a) Schematic of DNA origami fabrication. Scaffold and staple strands are mixed to form a pre designed structure. The staple strands are designed in a way that they fold the scaffold to yield the intended structure. The final nanostructure is stabilized by various interconnecting strands. Image taken from S. Dey et al.[154]. b) Schematic of the first 3d DNA assembly created by Seeman in 1991.[155] The cube consists of six DNA loops, shown in different colors, that are twisted into their neighbouring strands. Image taken from N. Seeman et al.[156]. c) Schematics and AFM (atomic force microscopy) pictures of Rothemund's 2d DNA origami (2006). Scale bars in the lower row AFM images are 1 µm (2nd column) and 100 nm (3rd to 6th column), respectively. Image taken from P. Rothemund[157]. d) Models and TEM images of 3d origami by Douglas in 2009. Scale bars are 20 nm. Image taken from S. Douglas et al.[158].

Two single strands of complementary base sequences are therefore able to form a double-stranded DNA (dsDNA) in an antiparallel way. A dsDNA naturally coils into a helix shape, where one turn contains ten basepairs. The regular distance between bases is 0.34 nm.[110,153]

Taking DNA out of living systems, it is also used in nanotechnology to construct 2d and 3d objects on the nanoscale. The strands are 'folded' into a well-defined structure by a process that is known as 'DNA origami'. In 1991, Seeman created the first DNA based assembly. He used ten DNA strands of lengths between 36 and 80 bases to create six ssDNA loops forming the edges of a 3d cube as shown in figure 3.1b.[155,156] However, it was Rothemund in 2006 who first reported an efficient way to form DNA origami which is still used today. He used a 7,249 base 'scaffold' strand from the virus M13mp18 and added

over 200 shorter 'staple' oligonucleotides of mostly 32 bases in a single-step assembly as depicted in figure 3.1a. The staple strands couple to well designed spots of the scaffold, causing crossovers to other parts of the strand, which leads to a folding of the scaffold into the desired shape. Rothemund showed the formation of various 2d structures like a square, triangle, star, or smiley face, shown in figure 3.1c.[157] As shown by Douglas in 2009, it is possible to expand this technique to create 3d structures. He folded the double helices in multiple layers so that are connected by staple strands, showing the formation of 3d objects like cuboids or crosses, which are shown in figure 3.1d.[158,159]

Today, many examples of DNA origami constructs can be found in the literature.[154,160,161] The self assembly of DNA into various, well defined, shapes allows for the fabrication of large batches of highly uniform nanoparticles. Both static and dynamic structures are fabricated that are used in several fields like nanofabrication, biosensing, drug delivery, electronics or synthetic cells.[156,159,160,162,163] There are different software tools available that are used for the design process. For the DNA origami used in the context of this thesis, caDNAno[164] was used.[159]

3.2 Fabrication of Oil-Filled Core-Shell Particles

Chapter 5 reports on the diffusion of oil-filled core-shell particles, which is investigated by PFG NMR. The particle fabrication follows roughly the description given by Loxley and Vincent in 1998[165] and was slightly modified to obtain smaller particles and contains an additional NMR reporter as outlined in section 5.2.1. The fabrication principle is shown in figure 3.2. Two separate phases coexist in the beginning, which are poly(methyl methacrylate) (PMMA) in a mixture of hexadecane and dichloromethane (DCM), and an emulsifier like poly(vinyl alcohol) or sodium dodecyl sulfate (SDS) in water. As can be observed in the ternary phase diagram in figure 3.3 describing the mixture of PMMA, hexadecane, and DCM, the three components can be miscible (Region I), or phase-separated (Region II), depending on the concentration of each component. While PMMA and hexadecane are not miscible in absence of DCM, region I can be reached upon adding DCM.[165]

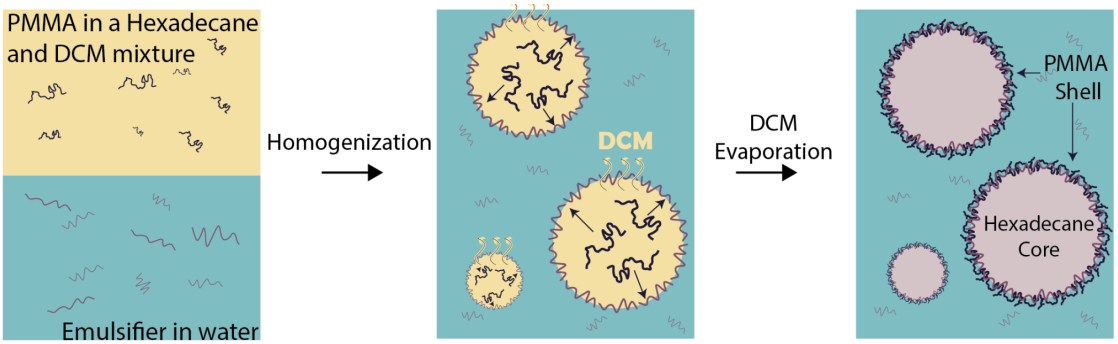

Figure 3.2: Fabrication mechanism of the oil-filled core-shell particles. Figure created by Nicolás Moreno-Gómez. Adapted from A. Loxley et al.[165].

The mixture of PMMA, hexadecane, and DCM is prepared to fulfill the requirements of the single-phase regime. It it then dispersed into the SDS containing aqueous phase, where an emulsion is formed by homogenization. The emulsifier's hydrophobic part stabilizes the oil droplets, while its hydrophilic head is exposed to the surrounding water. Acetone can further be added to the mixture of PMMA, hexadecane, and DCM as it has been shown to reduce the average size of the droplets and narrow their size distribution.[165] As discussed above, the droplets are in the single-phase domain (I). Upon increasing the temperature, the DCM, which was dissolving the polymer, evaporates, as does the acetone, if it is part of the mixture. This causes the system to move towards the two-phase domain (II), resulting in domains of concentrated PMMA migrating to the hexadecane-water interface. This process is called 'controlled phase separation' and yields hexadecane droplets surrounded by a PMMA shell.[165,166]

As pointed out by Loxley and Vincent[165,166], or Lars Evenäs (né Nordstierna)[167–169], different morphologies can be obtained by this method, ranging from core-shell particles, over acorn shapes, to inverted core-shell particles. Since the morphology of the system is dependent on interfacial tension and spreading coefficients of the phases, as well as kinetic effects, is is important to thoroughly select the compounds and find suitable working conditions.[165,169,170]

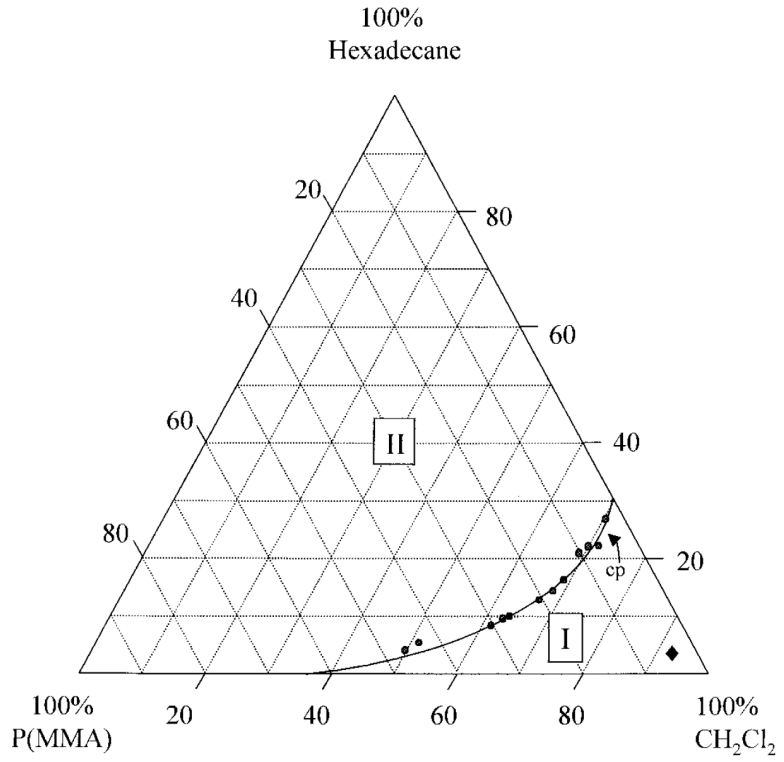

Figure 3.3: Ternary phase diagram for a three component system consisting of PMMA, hexadecane, and DCM CH_2Cl_2. Regime I and II represent the one- and two-phase region, respectively, and 'cp' denotes the consolute point. Image taken from A. Loxley et al.[165].

4 DNA Detection with Origami Diffusion Nanosensors

This chapter describes the realization of a DNA sensing method based on diffusion measurements of origami nanosensors. Most of the concepts and results discussed in this chapter are part of the paper

Ida Bochert, Jan-Philipp Günther, Izar Schärf, Erik Poppleton, Kerstin Göpfrich, Mariana Alarcón-Correa, and Peer Fischer. "DNA Detection with Origami Diffusion Nanosensors", *submitted 2025*

4.1 Introduction

Being able to detect the presence of specific DNA biomarkers is of importance for the diagnosis of a wide range of infections and diseases or antibiotic resistance.[1–5] Existing methods for direct DNA detection suffer from long experimental times or other constraints as mentioned before.[3,6–56] In the specific case of antibiotic resistance, one currently relies on blood cultures, antibiogramms and mass spectrometry which are also time-consuming.[5,171–174] The application of an immunoassay as described by He et al[53], followed by the detection of the analyte DNA using nanopores allows for the detection of proteins or other biomarkers.[53–56] For this, the target protein is captured on paramagnetic beads (PMBs) using antibodies on the PMB surface. The analyte DNA is attached to the complex using a second antibody and streptavidin/biotin binding. By UV light exposure, the analyte is released and ready to be detected. The analyte serves as a proxy for the biomarker and can also be amplified during the process, if needed. This immunoassay provides an analyte DNA that is then detected by nanopores in form of a conductance

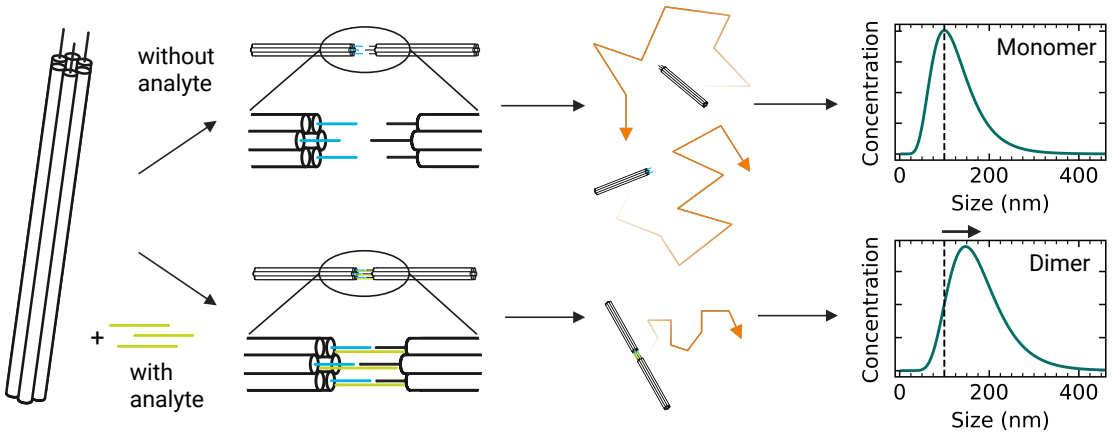

Figure 4.1: Schematic explanation of the behaviour of the system without analyte strands (top) and in the presence of analyte strands (bottom). The analyte can couple two DNA origami structures, which leads to an increase in size and hence a decrease in the diffusion coefficient. This is indicated as a size shift in the PSD plot. Created with BioRender.com.

change.[53] However, the nanopores are difficult to fabricate and can easily clog, which is a major drawback. The measurement times range from 10 to 30 min.[53,55,175]

As will be shown in this chapter, detection of analyte DNA is also possible by measuring the diffusion of a nanosensor, which offers a sensitive and fast alternative detection method. The diffusion of nanoparticles is directly related to their size, so if the analyte generates a change in size of the nanosensors, its presence can be observed by a change in diffusion. This is achieved by connecting two nanosensors via the analyte, which leads to an increase in size and therefore in a change in the diffusion coefficient. Figure 4.1 presents a schematic explanation of this process. As will be discussed in section 4.2, DNA origami structures are a promising choice as diffusions sensors due to their well-defined shape and size. They further allow for specific binding of the analyte and their diffusion can be measured precisely by Fluorescence Nanoparticle Tracking Analysis (NTA-FL). The proposed method allows for sensing of picomolar concentrations of an analyte strand in a measurement time of about seven minutes.

While DNA origami is used for various sensing applications[56,176–186], examples of diffusion measurements of DNA origami are scarce in literature. Liu et al. investigated the thermophoretic motion of DNA origami in polymer networks.[187] Others tested for membrane binding using diffusion measurements by single particle tracking or fluorescence correlation spectroscopy.[188–190] The same methods have been used to measure diffusion

of free DNA origami.[191–193] As far as we are aware, there are no other studies on analyte sensing methods based on diffusion of DNA origami.

The origami nanosensors used in the context of this chapter are based on a six-helix bundle (6HB) motif.[194] DNA strands are folded to obtain a honeycomb structure made of six double helices. The overhangs can be exchanged to couple to predefined DNA strands. Section 4.3 gives details on the design, fabrication, and properties of these structures. By carefully designing the sequence of the nucleobases in the overhangs of the 6HB, they can couple to a complementary sequence, which can be used to form dimers of 6HB structures as shown in section 4.4. The presence of a 30 base ssDNA of an arbitrary sequence, denoted as the IM (intermediate) strand, is detected by the origami and the results are presented in section 4.5. Further, a DNA origami 'detection kit' is suggested and was tested experimentally, which allows for the versatile application of the method.

For the special case of antibiotic resistance, a 40 base sequence unique to the antibiotic resistance gene blaOXA-48 was investigated as presented in section 4.6. The OXA-48 enzyme carbapenemase (UniProt: Q6XEC0) is able to metabolise beta-lactam and carbapenem antibiotics and represents the class of beta-lactamases, which contribute significantly to widespread antibiotic resistance.[195–198]

4.2 DNA Origami as a Diffusion Tracer

Chemically synthesized nanoparticles can be fabricated with well defined shapes and a reasonably high degree of monodispersity.[199,200] Therefore, the question might arise why DNA origami is used as a diffusion sensor in this context. DNA origami has some features that makes it a perfect choice for sensing a ssDNA analyte by diffusion. The following section explains these advantages of DNA origami, and how their diffusion can be measured and evaluated precisely and in few minutes.

4.2.1 Requirements of a Diffusion Tracer for DNA Detection

As discussed in section 3.2, the fabrication of DNA origami follows a strict scheme and is therefore highly reproducible. It can therefore be assumed that the resulting origami

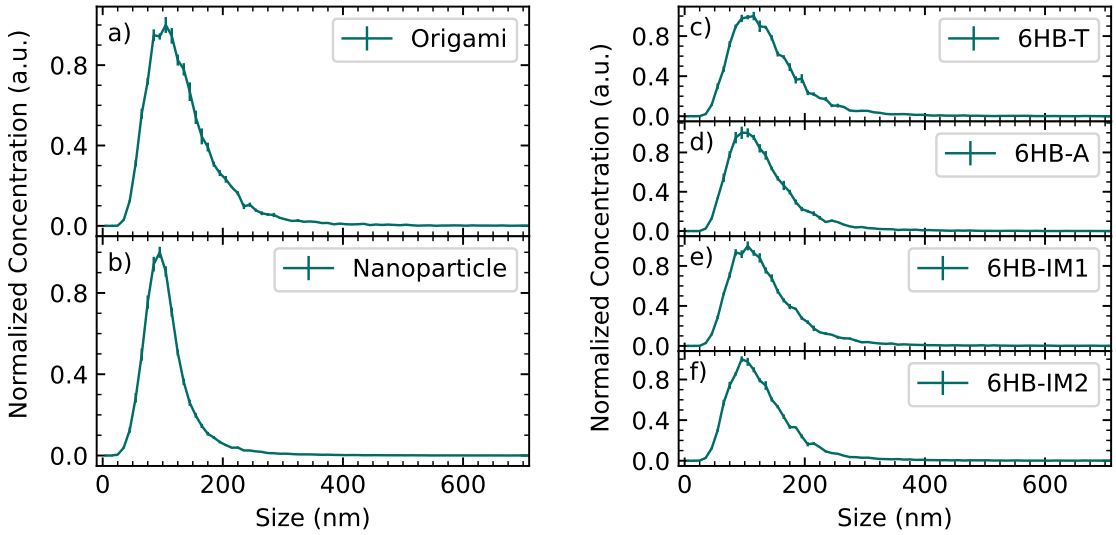

Figure 4.2: Particle size distributions as obtained from NTA and NTA-FL measurements. a) A 5 pM suspension of 6HB DNA origami 6HB-A' in TA/$MgCl_2$ buffer, measured by NTA-FL. b) Polystyrene standard nanoparticles of diameter 100 nm, diluted to around 11 pM in water, measured by NTA. c) - f) 6HB DNA origami structures with different overhangs as indicated by the letter(s) in the name. Details on the overhang sequences are given in section 4.3.2. All samples were measured at 5 pM. All curves presented in a) to f) are averaged over five measurements per sample and the error bars are calculated as the standard error of the measurements.

structures are monodisperse and show a well-defined diffusion coefficient. Crucially, the monodispersity follows from the design and assembly and is not a function of the conditions used for the synthesis as is the case in the chemical synthesis of nanoparticles. This makes them an attractive choice for the use as diffusion tracers.

To estimate the quality of a 6HB particle size distribution measured by NTA or NTA-FL as described in detail in the next section, the PSD of a 6HB-A' (see section 4.3.2 for details about the 6HB design) suspension in TA/$MgCl_2$ buffer (all buffer recipes are given in section A.1.4) of a concentration of 5 pM is compared to that of an aqueous suspension of chemically synthesized spherical polystyrene standard nanoparticles of around 11 pM.[1] The size of the particles is around 100 nm according to the manufacturer. The resulting plots of the PSD obtained by NTA (nanoparticle) and NTA-FL (DNA origami) are shown in figure 4.2a and 4.2b. For each sample, five measurements were performed and averaged. The evaluation was performed using the parameters mentioned in section A.1.1. The

[1]The particles were provided by *Malvern Panalytical*[201] and are denoted as 'Polystyrene latex standard NTA4088'. The concentration of the standard particles was calculated from the results of the NTA measurement, since it was not provided by the manufacturer.

error bars represent the standard error of five measurements. It can be observed and is intuitively reasonable that the spherical nanoparticles show a narrower peak in the PSD than the 6HB due to the different spatial dimensions of the latter. As discussed in section 4.3, the 6HB show a cylindrical shape. It is therefore assumed that the diffusion of 6HB – although probably highly monodisperse – depends on their orientation with respect to the diffusion direction and the peak is therefore broader than for a spherical particle.

However, the size peak of the 6HB origami is narrow enough to detect small size changes, as will be shown later. Although not as narrow as the spherical particles, DNA origami has the great advantage over chemically synthesized nanoparticles that it possesses high molecular specificity. The overhangs of the 6HB can be designed as needed and allow for highly specific binding to any other DNA labelled object. Having a well defined number of overhangs would not be possible for chemically synthesized particles and therefore makes the DNA origami a valuable diffusion tracer system.

To prove that the PSD of a 6HB is independent of the overhangs, the PSD of different structures were measured by diffusion. The results are shown in figure 4.2. Each graph refers to an origami structure with different overhangs. More details on this will be given in section 4.3. It can be seen that all graphs are highly comparable regarding the peak position, as well as the shape of the curve. This shows that it is possible to modify DNA overhangs without changing the overall dimensions of the 6HB. DNA origami can hence be used as a versatile and precise nanosensor for diffusion measurements.

4.2.2 Diffusion Measurements by NTA-FL

To measure nanoparticle or DNA origami diffusion of down to picomolar concentrations, NTA and NTA-FL can be utilized as explained in section 2.2.2. The measurements shown in this chapter were performed on a *Nanosight NS300* setup. The suspensions were diluted in TA/$MgCl_2$ buffer to a final concentration of 5 pM of each type of origami that is used in the specific experiment. To prevent disturbing signals from contamination in the buffer, the used buffer was filtered using a 20 nm syringe filter prior to usage. The same buffer was used to flush the flow chamber before loading the new sample. The DNA was fluorescently stained using SYBR gold at a concentration of 0.4x. The samples were mixed and quickly transferred to a light-shielded system to protect the fluorophore from

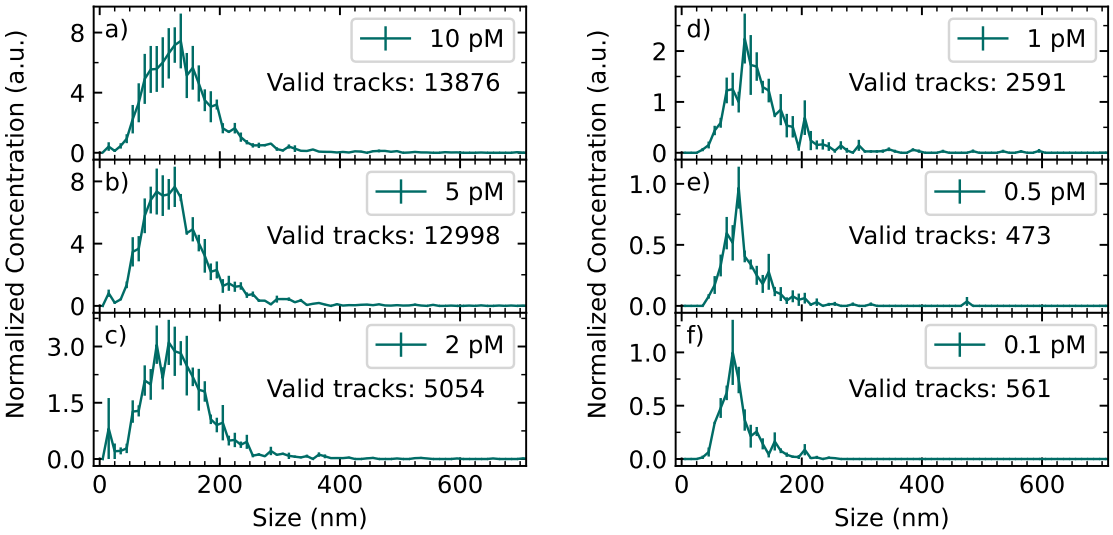

Figure 4.3: Size distributions of a 6HB structure comparable to 6HB-T at different concentrations as measured by NTA-FL. The DNA origami were diluted in TA/$MgCl_2$ buffer. The detection threshold was reduced for the measurements shown in e) and f). Three measurements per sample were measured and averaged. The error bars present the standard error of the three measurements. All measurements are normalized to the maximum value of the 0.1 pM sample. The number of valid tracks for all three measurements together as evaluated by the *Nanosight NTA 3.4* software are indicated.

bleaching. Details about the used settings and parameters for the NTA-FL measurements are presented in the appendix (section A.1.1).

To determine the minimum concentration and a reasonable working condition for the measurements, NTA-FL on DNA origami samples containing DNA origami of different concentrations was performed. The 6HB structure used here is comparable to 6HB-T (see section 4.3.2)[2]. Each result shown in figure 4.3 is obtained from three measurements of 1 min. The error bars represent the standard error of those. The evaluation is performed in a slightly different way compared to the standard parameters given in section A.1.1 as a blur of 7×7 was used. For the measurements on concentrations of 0.5 pM and lower, the detection threshold was reduced to 3. The number of valid particle tracks is given in each graph.

It can be observed that the curves of all concentrations have their maximum at roughly the same size. However, the peaks of the measurements performed at higher concentration

[2]The used 6HB structure has three polyT(5) overhangs and three overhangs of the random sequence *GAG TGA TAC CTT ACC G* on the O1 side, and each three overhangs of polyT(5) and polyT(16) at O2.

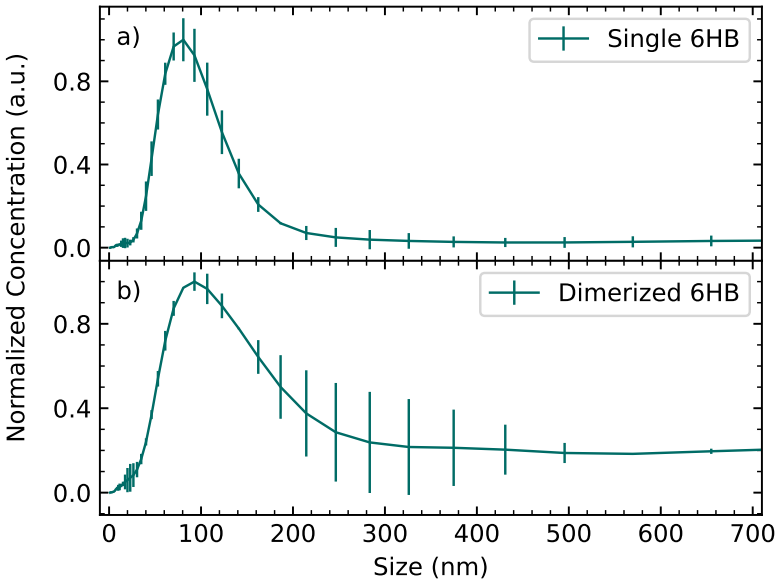

Figure 4.4: Size distributions as measured by DLS using the *Nanotemper* system. Three measurements of ten acquisitions each were performed and averaged. Some acquisitions were sorted out by the instrument. The error bars represent the standard deviation of all valid acquisitions. The measurements were performed a) on a structure comparable to 6HB-A' at a concentration of 6.2 nM and b) on a dimerized sample using 6HB comparable to 6HB-A and 6HB-T at a concentration of 2.9 nM (details about the structures are given in the text).

are broader and seem to represent the sample in more detail. The intensity of the error bars with respect to overall covered particles (represented by the area under the curve) decreases for higher concentrations. The number of valid tracks obviously increases with the concentration of DNA origami. The results show that NTA-FL can be performed with concentrations down to around 0.5 pM. However, while the working concentration for the later discussed experiments is aimed for being as low as possible, it should still allow for significant results in a reasonable measurement time of some minutes. To be able to base the measurements in the context of this chapter on enough valid tracks, a concentration of 5 pM was always chosen unless otherwise noted.

Another method so measure a PSD is the *Nanotemper Prometheus Panta* instrument. The measurements were performed at Heidelberg University Biochemistry Center (BZH) with the help of Merlin Schwan. The instrument performs DLS, i.e. it measures scattered light and uses a correlation function to calculate the PSD.[202] Its advantage compared to conventional DLS instruments is the low sample volume of some microliters needed. We

therefore measured two samples with a *Nanotemper* system, namely a 6HB comparable to 6HB-A' (see section 4.3.2)[3] at a concentration of 6.2 nM and a 2.9 nM sample containing the just described 6HB with polyA overhangs and an origami comparable to 6HB-T that were dimerized as explained in section 4.4 in HEPES buffer. The result is shown in figure 4.4. Compared to the measurements using NTA-FL (e.g. in figure 4.2), the *Nanotemper* measurements show a slightly smaller maximum value, while the error bars are larger, especially in figure 4.4b. Three measurements with ten acquisitions each were performed and averaged. However, the instrument software sorts out every measurement that does not meets its internal quality criteria, e.g. due to a concentration that is too low. This is the case in figure 4.4b, where the used concentration of around 3 nM is apparently on the lower limit of the instrument. Only 20 out of 30 acquisitions gave reasonable results and are therefore included in the evaluation.

Comparing the results obtained by the *Nanotemper* system with the ones measured by NTA-FL, both the needed amount of sample and the results have to be considererd. The NTA-FL measurements are performed on 1 ml of a 5 pM suspension, which is a total amount of 5 fmol of DNA origami. The amount and volume used for the *Nanotemper* measurements add up to an amount of roughly $5\,\mathrm{nM} \cdot 10\,\mu\mathrm{l} = 50\,\mathrm{fmol}$, which is around one order of magnitude higher than what is needed for the NTA-FL measurements. Therefore, NTA-FL measurements are preferred for the continuation of this project.

4.2.3 Evaluation of NTA-FL Measurements

The already discussed figure 4.2 shows two exemplary PSD curves as measured by NTA-FL. What is shown as a line with error bars here is in principle evaluated as a histogram with pre-defined bins of 10 nm width. The error bars show the standard error of five measurements on the same sample (if not otherwise stated). In the following chapter, the size distributions are evaluated by fitting a log-normal distribution[203] which follows

$$p(x) \propto \frac{1}{\sqrt{2\pi}\sigma x} \cdot \exp\left(-\frac{(\ln(x) - \ln(x_\mathrm{m}))^2}{2\sigma^2}\right). \tag{4.1}$$

[3]The 6HB used for the *Nanotemper* measurements has each three polyT(5) and polyA(15) overhangs on the O1 side, and each three overhangs of polyT(5) and the random sequence *AAT ATC TGT ATG TCT A* at O2.

Here, $\ln(x_\mathrm{m})$ describes the mean of $\ln(x)$ and σ is the standard deviation of $\ln(x)$. The log-normal distribution is a commonly used model for particle size distributions.[203–206] However, the broadening of the PSD peak is assumed to be also caused to some extent by the procedure of NTA-FL. In this method, every particle is tracked for as many frames as the software is able to follow the particle. A minimum track length can be set, which in the following is chosen to be five frames. All particle tracks shorter than five frames are discarded. The average covered distance between two frames is calculated to get the apparent (i.e. measured) diffusion coefficient and hence the size of each individual particle. The higher the number of frames for each particle, the closer the apparent and the real particle size get. Although the chosen minimum value of five frames is assumed to allow for a good estimation of the particle size, there is an uncertainty in size for particles showing short track lengths.

A different fit model in the literature[207,208] assumes all trajectories to have the same length. Using this model to evaluate the data obtained from the *Nanosight NTA 3.4* software would therefore require recalculation and cutting of the particle tracks, which leads to worse distribution data. Testing this evaluation on an exemplary NTA measurement showed that the modification of the data leads to a broader peak since information achieved from longer particle tracks gets discarded. Further, the fit model has been tested to fit worse on the modified data than the log-normal distribution does on the original data. The log-normal distribution is therefore used in the following. Nevertheless, the fit function should be understood as an apparent particle size distribution rather than a real distribution since the broadening of the peak is not (only) caused by polydispersity but also by uncertainties caused by the method.

To compare different measurements, the maximum value of the log-normal distribution is used as given by $d_\mathrm{max} = \exp(\ln(x_\mathrm{m}) - \sigma^2)$. It depicts the species (monomers vs dimer 6HB) with the highest concentration. Different to the mean of the distribution it is not (or much less) affected by the presence of chunks or randomly occurring aggregates. In the following, the maximum values of the log-normal distribution fit will always be given with their uncertainty that is derived as described in section A.2.1.

4.2.4 Evaluation using a Global Fit

When expecting different species like single 6HB (monomers) and dimerized 6HB structures with different hydrodynamic sizes in a sample, the measured PSD will be a sum of two or more curves. If these species are far from each other in size, the PSD will show distinct peaks. If the sizes are too close to each other to discriminate them, the peaks will fuse to one peak that includes information on all species. While the standard evaluation performed in the context of this chapter relies on fitting a single log-normal fit and relying on the maximum value, there is another fitting model that includes the different present species. This global fit uses a sum of log-normal distributions, each of them representing one species i, for example monomers, dimers, and multiples, like

$$p(x) = \sum_i \frac{A_i}{\sqrt{2\pi}\sigma_i x} \cdot \exp\left(-\frac{(\ln(x) - \ln(x_{\mathrm{m},i}))^2}{2\sigma_i^2}\right). \tag{4.2}$$

Here, A_i describes the intensity of each signal, $\ln(x_{\mathrm{m},i})$ denotes the mean of $\ln(x)$, and σ_i is the standard deviation of $\ln(x)$ for each species i = Monomers, Dimers, Multiples. The size and standard deviation of a species are assumed to be constant and independent from the concentration of this species. Hence, for the evaluation of different measurements, like one sample containing more monomers versus another sample with mostly dimers, the mean particle size $x_{\mathrm{m},i}$ and the standard deviation σ_i are taken as global parameters and are adjusted to a value that fits all measurements. The intensity A_i of each curve is fitted for every measurement individually. It represents the concentration of the corresponding species.

Figure 4.5a shows a schematic explanation of this procedure. Artificially created curves mimicking NTA-FL measurements are shown and fitted with a sum of a monomer and a dimer curve, shown in blue and green. The resulting fit, given by the sum of both, is shown in gray. While the position and standard deviation of the curves representing monomers and dimers are the same for the top and the bottom curve, only their intensity changes to fit the shift in the curve mimicking the NTA-FL measurement. A graphic representation of the fitting parameters is given in figure 4.5b. The global parameters are indicated by dashed lines, while the intensity (solid line) is fitted for every single measurement.

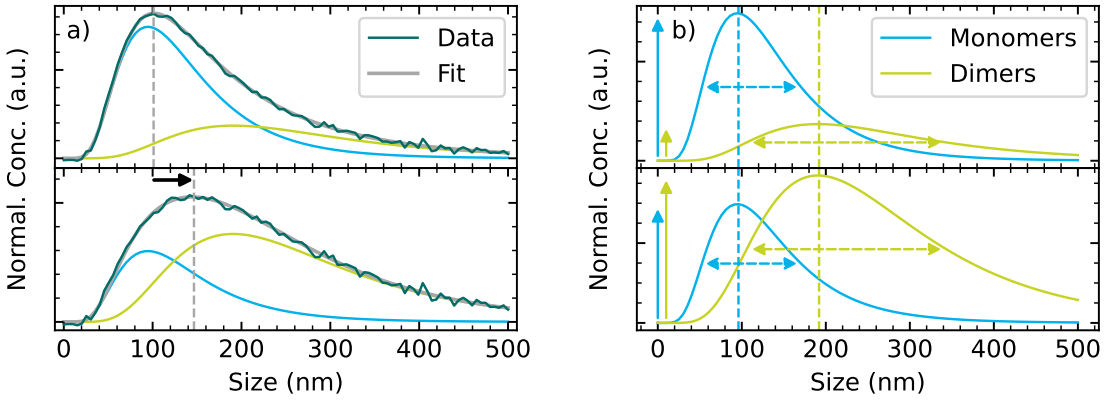

Figure 4.5: Schematic explanation of the global fitting method. The overall fit (gray) as given in equation (4.2) is calculated from a sum of the log-normal fit representing all monomer structures (blue) and the fit showing the dimers (green), following the log-normal distribution as well. a) An exemplary created curve, illustrating a PSD as measured by NTA-FL, is shown in dark green. From top to bottom subfigure, a shift in the measured size is indicated by the arrow. b) The fitting parameters are depicted. Global parameters, i.e. the maximum position and the standard deviation, are indicated by dashed lines, while the solid lines represent the intensities of each curve, which are adjusted for each measurement individually. It can be seen that a change in intensity of the curves leads to the size shift indicated in a).

4.3 Six-Helix Bundle DNA Origami

DNA origami has been shown to serve as a precise and versatile nanosensor for diffusion measurements in the last section. The DNA origami structures used in the context of this thesis are called Six-Helix Bundle (6HB). In this section, their structure is presented, as well as the detailed base sequences of the used overhangs. The fabrication process is described. We further examined the effect of the intercalating dye on the structures, which is used for the NTA-FL measurements.

4.3.1 Overview of 6HB

As their name suggests, the 6HB origami structures are made up of six dsDNA helices that are arranged in a honeycomb pattern as depicted in figure 4.6a.[194] The helices are shown schematically as cylinders. The resulting worm-like structure has a length of around 440 nm as obtained from Molecular Dynamics (MD) Simulations using oxDNA.[209–211]

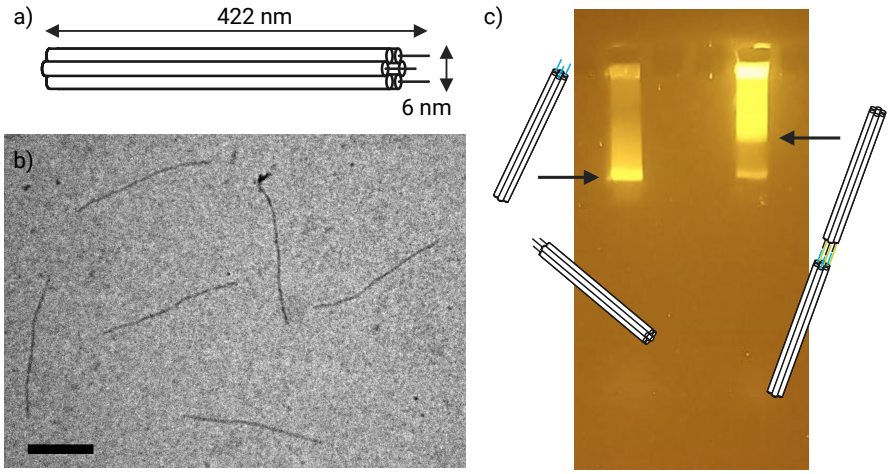

Figure 4.6: 6HB origami structure and methods for validation of successful folding. a) The structure of a 6HB is shown schematically. Each double helix is represented as a cylinder. Only three overhangs are shown, which are intended to bind to another structure as discussed in section 4.3.2. b) TEM image of a 6HB-A structure. The sample preparation and measurement are outlined in the text. The scale bar is 200 nm. c) Result of gel electrophoresis using a structure comparable to 6HB-A (left column) and a sample of dimerized 6HB (see section 4.4.1) (right column). Created with BioRender.com.

The simulations were performed by Erik Poppleton. The diameter is around 6 nm as can be deduced from the corresponding caDNAno file.[164]

The basis of the 6HB structures is a 8064 base DNA strand strand. This circular viral scaffold strand ordered from *Tilibit* is commonly used for DNA origami.[158,212–215] Using caDNAno[164], a total of 192 body staples and eight edge strands were designed to connect the scaffold and form the intended structure of the six double helices. The design was provided by Kerstin Göpfrich. The folding was performed in a TE/$MgCl_2$ buffer (see section A.1.4 for buffer recipe). The scaffold was used in a concentration of 10 nM. Staples and edge strands were added in a 10-fold excess. Everything was then temperature cycled as shown in figure 4.7. The heating to 70 °C leads to breaking of all unintended bindings. The slow temperature ramp down to 20 °C allows the system to self-assemble by finding the energetically best and most stable configuration. The suspensions containing the folded origami structures were then washed using 100 kDa Amicon size exclusion filters, performing three cycles of five minutes at 13000 rcf and 4 °C. Size exclusion filters have been shown to give good results in DNA origami purification.[216–218] The washing was done with a 0.5x TA/$MgCl_2$ buffer. After the filtering process, the concentrations were

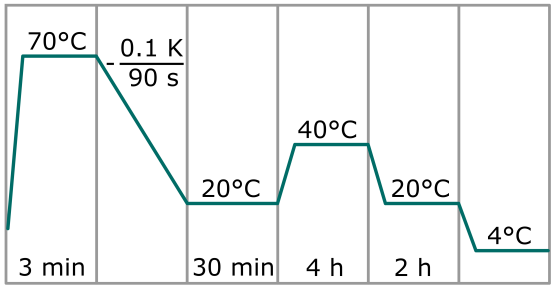

Figure 4.7: Protocol of the temperature cycling protocol used for the folding of the DNA origami.

adjusted to the final buffer concentrations of the TA/$MgCl_2$ buffer. Finally, the origami concentration was measured using a UV-Vis *Nanodrop ND-1000*. The whole fabrication process follows a workflow that was applied in our group earlier.[194]

To test the achievement of correctly folded origami structures, TEM and gel electrophoresis are commonly used.[154,158,159,194] The TEM grids were prepared by glow discharge, using 15 mV and 10 mA for 30 s at 0.39 atm. The DNA origami samples were diluted to a final concentration of 0.1 nM. A volume of 3 µl of the sample was left on the grid for 2 min. After that, filter paper was used to remove the liquid. The grid was then stained with uranyl acetate. Two droplets of 7 µl were added. The first droplet was removed immediatly, the second droplet was left on the grid for 30 s before removing the liquid. The samples were allowed to air-dry before performing TEM. The images were taken on a *Philips CM200*, using a LaB6 electron gun and a voltage of 200 kV. This procedure is applied for all TEM samples mentioned in this chapter, unless otherwise specified.

Figure 4.6b shows a TEM image of a 6HB-A sample (see section 4.3.2 for the overhang specifics). Six 6HB origami structures can be seen, which all seem to have the same length and thickness. The length of folded 6HB origami structures measured from TEM images is 445 nm, which agrees well with the value calculated by the MD simulations. This is an indicator that the folding worked nicely. In addition, figure 4.6c shows an example of a gel electrophoresis result on 6HB-A (left column). It has to be noted that this is an older version of overhangs used in this example compared to what is given in section 4.3.2.[4] 10 µl of a sample containing 6HB-A (left) and a dimer sample (discussed in section 4.4.1) were filled in the cavities of a 2 % agarose gel in TAE/$MgCL_2$ buffer

[4]The 6HB used here has each three polyT(5) and polyA(15) overhangs on the O1 side, and each three overhangs of polyT(5) and the random sequence *AAT ATC TGT ATG TCT A* at O2.

(buffer recipe given in section A.1.4) stained with SYBR gold. TA/$MgCl_2$ was used as a running buffer. The experiment was run with a voltage of 72 V and protected from light for around 1 h 30 min. In gel electrophoresis, all charged particles are attracted by the oppositely charged electrode. Dependent on their size, the particles move faster or slower through the gel, generating a separation of the particles by their size.[110] The picture shows a bright, narrow band. This is an indicator for particles that have the same (hydrodynamic) size, which in turn causes them to move through the sample with the same speed, ending up in a narrow band. This gives evidence that the origami structures are correctly folded. However, there is a small amount of smearing between the band and the cavity visible. It is assumed to be caused by different orientations of the structures. While the ones that are oriented in the direction of travel are assumed to slip through the holes of the gel nicely, the structures that are oriented transverse to the direction of motion can get stuck more easily and are therefore assumed to move slower.

4.3.2 Design of the used 6HB Structures

While the sequences of the inner DNA staples that keep the origami in shape are important to keep constant, the overhanging parts of some edge strands are not needed to fold the origami. These parts that are sticking out of the structure can therefore be modified as desired. The 6HB are designed in a way that each side (called O1 and O2) has four DNA strands that contribute to the edge part. Figure 4.8 shows a snapshot of caDNAno[164], where the different strands are coloured differently. It can be seen that for both sides two strands face out with either the 5' or the 3' end, while the other two have both ends sticking out. These in total eight strands are denoted as overhang strands and can be exchanged in the folding process as needed for the experiments. For the projects discussed in the following, some origami structures are intended to bind to another object or DNA strand, while other ends should not bind to anything.

At the 'active end', three overhangs (either the ones sticking out with their 5' end or the ones with the 3' ends) are intended to bind to a well-defined other DNA sequence, while the other three overhangs, as well as the six overhangs at the 'passive end' are designed to show the non-binding (NoB) sequence *ACAGA*. This NoB sequence is chosen to avoid unintended binding to another present DNA strand. In figure 4.6a, only the three binding

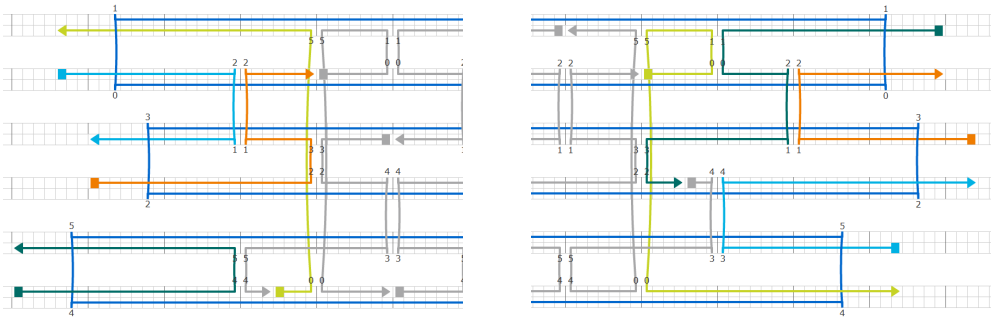

Figure 4.8: Snapshot of both ends of a 6HB structure as shown in caDNAno.[164] The dark blue line represents the scaffold, gray lines show internal staple strands, and all other colored lines represent the different overhang staples. For each side, there are four ssDNA strands, that produce each three overhangs at 5' and three at 3' ends.

overhangs are shown. The overhangs that are used in the presented experiments and the names of the corresponding 6HB structures are given in table 4.1. All DNA sequences are per convention written starting from the 5' end. The overhangs of most types of origami that have O1 as the 'active end' have the 5' end facing out (except for the 6HB-T), while for the O2 'active ends', the overhangs end on 3'.

In the later discussed experiments, the 6HB-A and 6HB-T are intended to directly bind to each other, while the 6HB-IM1 and 6HB-IM2 or 6HB-Oxa1 and 6HB-Oxa2 can be connected via the so called IM strand *GGA ATG ATG ACG GAG GAT GAA TGA GTG AGC* or Oxa strand *GTT GGA ATG CTC ACT TTA CTG AAC ATC AAT CAC AGG GCG T*, respectively. The formation of these complexes is schematically depicted in figure 4.9, where only one overhang is shown exemplary. The IM strand shows a random, non self-dimerizing DNA sequence, while the Oxa strand is a unique part of an antibody resistance gene blaOxa-48.[195–198] The connector strands used in section 4.5.4 have the sequences *CTC CGT CAT CAT TCC TTT TTT TTT TTT TTT* and *TTT TTT TTT TTT TTT GCT CAC TCA TTC ATC*.

4.3.3 Effect of an Intercalating Dye

The main measurements in this project to obtain the particle size distribution are performed by NTA-FL, which requires fluorescent labeling of the DNA origami structures. This is done by using SYBR gold, which is a dye that intercalates into the DNA double

Table 4.1: DNA sequences of the different overhangs of the 6HB structures used in the context of this thesis. The column 'end' gives the active end which defines on which end of the origami the binding sequences are attached. The other three, as well as the six overhangs on the passive end show the sequence *ACAGA*. If the active side is O1, the overhangs end on a 5' end, except for the 6HB-T. If O2 is the active side, the sequences have their 3' end facing out. All DNA sequences are written starting from the 5' end.

Name	Overhang sequence	End	Drawing
6HB-A	*AAA AAA AAA AAA AAA*	O2	
6HB-A'	*AAA AAA AAA AAA AAA*	O1	
6HB-T	*TTT TTT TTT TTT TTT*	O1	
6HB-IM1	*CTC CGT CAT CAT TCC*	O1	
6HB-IM2	*GCT CAC TCA TTC ATC*	O2	
6HB-Oxa1	*AGT AAA GTG AGC ATT CCA AC*	O1	
6HB-Oxa2	*ACG CCC TGT GAT TGA TGT TC*	O2	

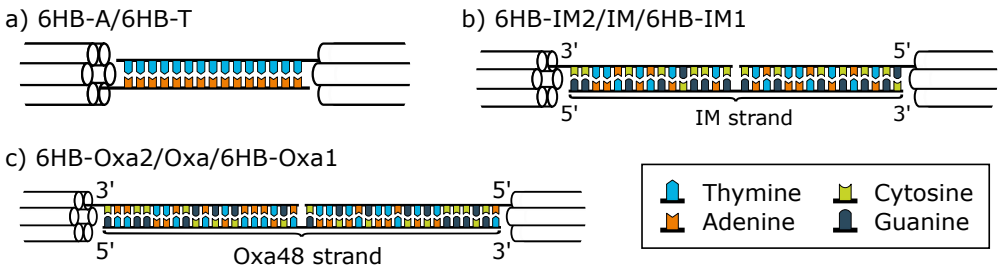

Figure 4.9: Schematic presentation of the different types of 6HB structures and their intended binding partners. Only one of the three binding overhangs per 6HB is shown for the sake of simplicity. a) 6HB-A and 6HB-T are used in the experiments described in section 4.4. b) 6HB-IM1 (left) and 6HB-IM2 (right) can be connected by the IM strand as shown in section 4.5. c) Analogously the Oxa strand can dimerize the structures 6HB-Oxa1 and 6HB-Oxa2 as discussed in section 4.6.

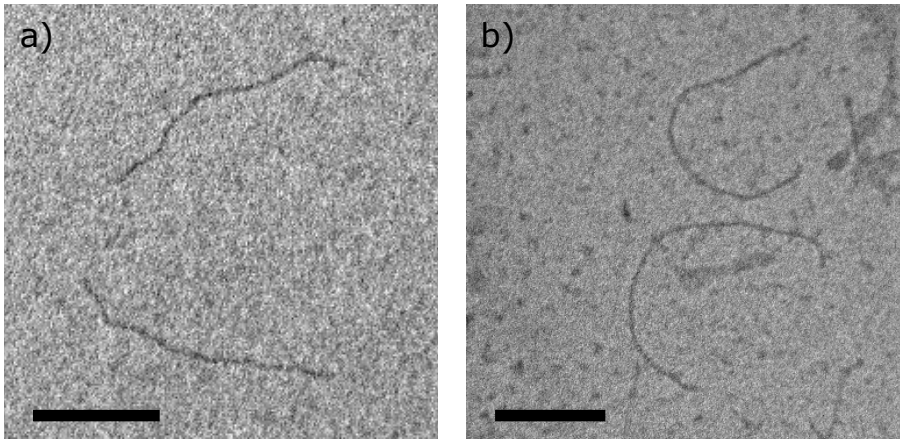

Figure 4.10: Comparison of 6HB-IM2 structures with (b) and without (a) SYBR gold staining as shown by TEM. Scale bar is 200 nm.

strand.[219] According to literature, intercalating dye can be assumed to generate unwinding of the DNA double helix, leading to an elongation of the double strand.[219,220] Kolbeck et al. measured an unwinding angle of 19.1° per molecule and a length increase by a factor 1.7.[219] While this effect of intercalating dye on a double stranded DNA is known, the corresponding impact on a DNA origami is less understood. As Kim et al. assume, the unwindig of the dsDNA is compensated by winding of the whole 6HB structure.[220] In the following it is therefore assumed that the intercalating dye leads to an elongation an unknown factor, and winding of the 6HB structure.

We therefore tested for elongation of the 6HB structures upon adding SYBR gold by comparing the length measured from TEM images of a sample with and a sample without dye, using 6HB-IM2 origami structures from the same folding batch. The concentration of origami was 0.1 nM each. For the stained sample, the SYBR gold was diluted to 80x, which is the same amount of SYBR gold per origami structure as used for the standard NTA-FL measurements. TEM was performed as outlined in section 4.3.1. Exemplary images are shown in figure 4.10, where figure 4.10a represents unstained structures, while the structures shown in figure 4.10b is stained with SYBR gold. The mean lengths of the structures are

$$l_{\text{no dye}} = 439\,\text{nm}$$

$$l_{\text{with dye}} = 675\,\text{nm}.$$

A number of 25 and 18 origami structures were analyzed. The dye can therefore be assumed to cause an elongation of the 6HB structures by a factor of around 1.5. However, for the NTA-FL measurements, which are performed in solution, it remains unclear what the exact dimensions of the structures are. For the analyte detection discussed in the following, only a relative size change is measured, so that knowledge on the exact size of the origami is not required. For the theoretical considerations that are given later, the length obtained from the caDNAno estimation in absence of the dye is therefore used.

While the 6HB structure allows for using the intercalating dye and is assumed to react by twisting and elongation (which keeps the stability of the structure), other structures are less compatible with this sort of dye. A DNA origami cube, that has more connected layers and therefore more intersections, can be assumed to not being able to stay in a nice cubic form upon intercalating the dye. This can be observed when measuring NTA-FL or running gel electrophoresis. We observed a broader signal (PSD curve or bright band in the gel, respectively) for the cubes. The obtained signal of the 6HB, although their diffusion can be considered to be more orientation-dependent than the one of cubes, is therefore better suited for the shown experiments.

4.4 Formation of 6HB Dimers

The idea of this project is to detect the presence of a specific DNA analyte by measuring diffusion of DNA origami. If the connecting analyte strand is present in the solution, it is supposed to connect two origami structures, causing an increase in size. This is observed by measuring the diffusion coefficient of the DNA origami. The first question that has to be discussed in this context is if the change in size from a single 6HB to a dimerized 6HB is big enough to be detectable by diffusion measurements.

To investigate this, two designs of 6HB were used, that can dimerize directly, without the need for an analyte strand. The structures 6HB-A and 6HB-T have each three overhangs of 15 adenine or thymine bases, respectively. All ‘binding’ overhangs have the 3’ ends facing out. The overhangs are intended to bind to an origami structure of the complementary overhang and therefore lead to dimer formation. This system is simplified compared to the later discussed analyte sensing experiments in a way that only

two objects (i.e. two origami structures) need to encounter in solution, while for the later experiments, a third structure (i.e. the analyte) needs to meet the others in the solution. This simple system is used as a proof of concept for the possibility to distinguish between monomers and dimers by measuring their diffusion using NTA-FL.

4.4.1 Proof of Dimer Formation by TEM and Gel Electrophoresis

While in principle the complementary overhangs consisting of 15 adenine and thymine bases should couple by themselves very nicely, we supported the process by temperature cycling to achieve best results. Both types of origami (6HB-A and 6HB-T) were added to a TA/$MgCl_2$ buffer at concentrations of 1 nM. The dispersion was then cycled ten times between 27 °C and 34.5 °C, which is close to the expected melting temperature of the overhang strands. This process takes around 15 min. It helps the DNA strands to find their energetically preferred arrangement. If less than the maximum of 15 bases are coupled, the increase in temperature will melt the structure. By decreasing the temperature, the DNA strands have the possibility to couple again, in a (hopefully) more stable state. The temperature cycling procedure is shown schematically in figure 4.11.

To prove that the coupling procedure was successful, two methods were applied: The first one is gel electrophoresis, which was performed as described in section 4.3.1. In the context of figure 4.6c the successful folding of 6HB structures was already discussed for the 6HB-A sample in the left column. The right column shows a dimer sample, prepared from two structures comparable to the aforementioned 6HB-A' and 6HB-T[5], where the 6HB structures are assumed to be coupled via their complementary overhangs. Different to the coupling procedure outlined before, a higher concentration of 2.9 nM of each type of origami was used. Two bands can be observed for this sample in the gel. The heigth of the first one is close to the band in the monomer sample on the left. It shows that some 6HB are still present as monomers. The second band represents the dimerized structures.

[5]The structure comparable to 6HB-A' used here has each three polyT(5) and polyA(15) overhangs on the O1 side, and each three overhangs of polyT(5) and the random sequence *AAT ATC TGT ATG TCT A* at O2. The 6HB-T like structure has three polyT(5) overhangs and three overhangs of the random sequence *GAG TGA TAC CTT ACC G* on the O1 side, and each three overhangs of polyT(5) and polyT(16) at O2.

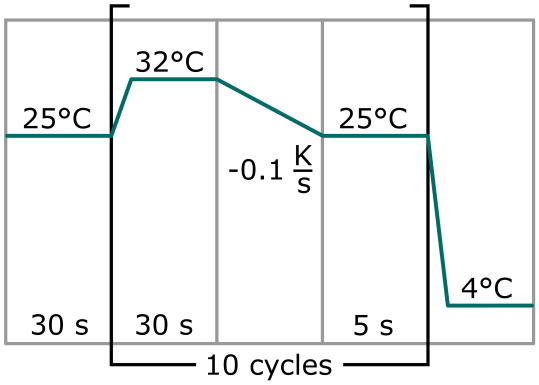

Figure 4.11: Temperature cycling protocol applied for the coupling of two DNA origami structures. The upper temperature is adjusted depending on the system.

Because of their bigger size, they travel less far in the gel. The smearing suggests that there could also be some aggregates forming.

The second method to show the successful coupling is visualization of the structures by TEM. The sample preparation for the TEM process is done as described in section 4.3.1. Figure 4.12 shows exemplary TEM images of the monomer samples 6HB-A and 6HB-T, as well as of the dimer samples. From the length of the structures, it can be clearly distinguished between a 6HB monomer of a length around 440 nm and a 6HB dimer, having a length of nearly 900 nm. The images of the monomer samples show that folding of the 6HB structures was successful and yields 6HB structures of a well-defined shape and size. The dimer images show structures of around double the length, which proves the coupling to be successful and couple structures (at least to some extent) as intended.

To estimate the ratio of coupled structures versus 6HB monomers, more TEM pictures were taken (over 30 images for the monomer samples, 70 for the dimer sample), which corresponds to a total number of over 330 6HB particles. The number of monomers, dimers, and multiples were counted and compared. Is has to be noted that separate structures were counted, where a dimer or a multiple count as one structure, not as two or more. The resulting numbers are given in table 4.2. It can be seen that the number of dimers increases from around 10 % in the monomer samples to about 55 % in the dimer sample. This again shows that the coupling procedure leads to a notable amount of dimers.

Table 4.2: Numbers of monomers, dimers, and multiples as counted in TEM images. The samples, containing 6HB-A, 6HB-T, and the corresponding dimer sample are defined in the text. More than 30 images for the monomer samples and 70 for the dimer sample were taken, which corresponds to a number of more than 330 particles in total.

Sample	Monomers	Dimers	Multiples
6HB-T	77.7 %	12.1 %	10.1 %
6HB-A	83.7 %	9.4 %	6.9 %
6HB-T + 6HB-A	22.6 %	54.8 %	22.6 %

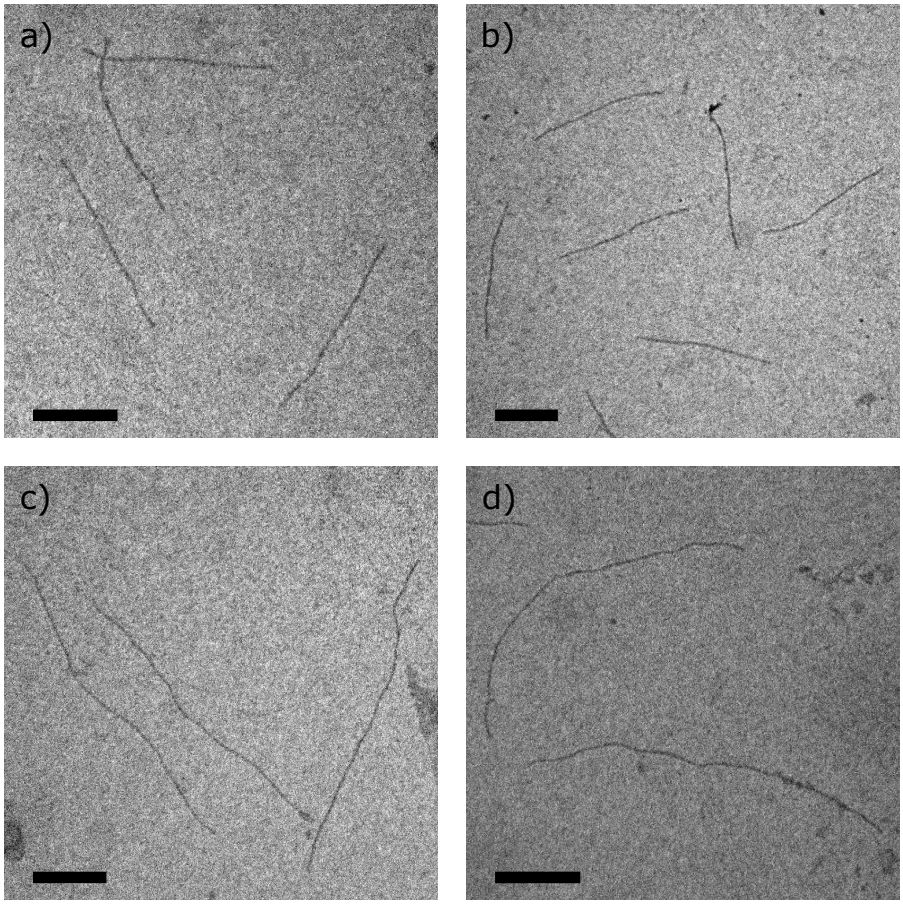

Figure 4.12: TEM images of 6HB monomers and dimers, obtained from the samples a) 6HB-T, b) 6HB-A, c) and d) dimer sample 6HB-A + 6HB-T as decribed in the text. Scale bar is 200 nm.

In the monomer samples, between around 7 % and 12 % dimers and multiples are present. This is assumed to be caused by unstable, short-lived conjugates that form upon binding of a small number of nucleobases in the overhangs between two origami structures, or due to unspecific binding. Moreover, the origami structures are assumed to be able to form multiples by mechanically generating knots. Further, it is unclear how much the drying for the TEM samples affects the aggregation. Some multiples can be found to be trimers, which occur in a small number of cases (around 2.4 % for the dimer sample). The trimers form by connecting one origami structure to two others instead of only one. This is possible due to the three binding overhangs. In the dimer sample, around 23 % of the 6HB remain uncoupled. The high number of dimers, however, is promising for the diffusion measurements.

4.4.2 Diffusion Measurements of Dimerized Samples

In the last section, it was shown that it is possible to couple two origami structures 6HB-A and 6HB-T using their complementary overhangs. Gel electrophoresis and TEM were used to prove the successful coupling and revealed a number of around 55 % dimerized structures. It can therefore assumed that the increased size of the dimers is visible in diffusion measurements by NTA-FL. Two monomer samples, 6HB-A and 6HB-T, were compared with a dimer sample prepared as discussed above. The NTA-FL measurements were performed as discussed in section 4.2.2.

Figure 4.13 shows the resulting PSD curves of 6HB-T, 6HB-A, and the dimer sample. The fit follows the log-normal distribution as given in equation (4.1). The maximum values of the PSD curves are $d_{\mathrm{max,6HB\text{-}T}} = (105.9 \pm 0.5)\,\mathrm{nm}$, $d_{\mathrm{max,6HB\text{-}A}} = (99.9 \pm 0.3)\,\mathrm{nm}$, and $d_{\mathrm{max,dimers}} = (147.2 \pm 1.3)\,\mathrm{nm}$. The maximum values of the monomer samples are very close to each other, which again shows the high reproducibility of the DNA origami folding, independently from the used overhangs. The maximum value of the dimer sample is clearly shifted to a higher value. This means that monomer and dimer sample can be distinguished by diffusion measurements, which should provide a good basis for the later discussed analyte sensing experiments.

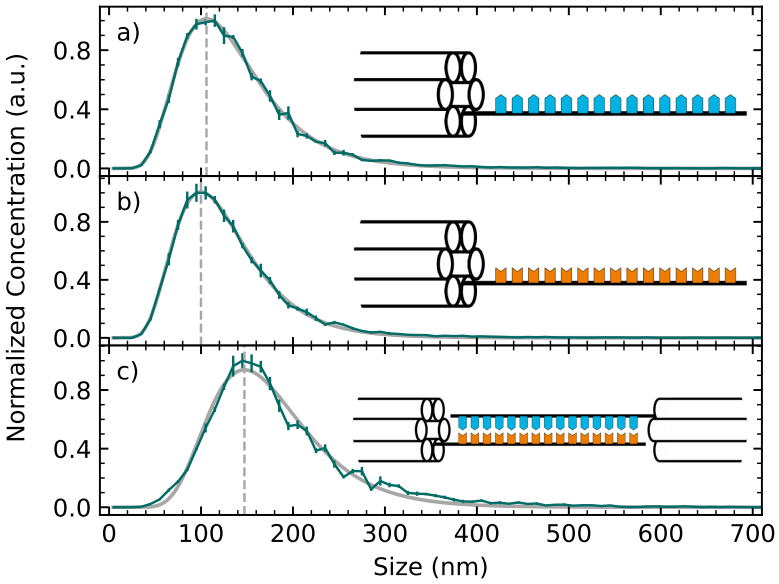

Figure 4.13: NTA-FL measurements show the size shift upon binding two origami structures as measured for the system of 6HB-A/6HB-T. a) PSD of the monomer sample 6HB-T, the maximum of the fit is at $d_{\mathrm{max,6HB\text{-}T}} = (105.9 \pm 0.5)\,\mathrm{nm}$. b) PSD of the monomer sample 6HB-A, the maximum is at $d_{\mathrm{max,6HB\text{-}A}} = (99.9 \pm 0.3)\,\mathrm{nm}$. c) PSD of the dimer sample 6HB-A + 6HB-T, the maximum is at $d_{\mathrm{max,dimers}} = (147.2 \pm 1.3)\,\mathrm{nm}$. Five measurements per sample were performed and averaged. The error bars represent the standard error of the five measurements. All samples were measured at a concentration of 5 pM of each origami structure. The gray fit follows the log-normal distribution as given in equation (4.1).

4.4.3 Theoretical Estimation of Diffusion Coefficients and Size Shifts

The first question to answer when discussing the idea of analyte sensing via measurement of size changes of DNA origami, is about the expected change in size. In the last section, it was shown experimentally that it is possible to distinguish between a monomer and a dimer sample by measuring their diffusion. The expected size shift can also be modelled theoretically, as shown in the following. To estimate the hydrodynamic radius of a single 6HB and the size shift that can be expected when dimers form, a model system of a stiff cylinder is applied. Although the 6HB structures seem to have some flexibility according to the TEM pictures, their persistance length is longer than the particle itself, which suggests a very stiff structure.[221] This stiffness is further confirmed by Molecular Dynamics (MD) simulations, which were performed by Erik Poppleton at the Max Planck Institute for Medical Research in Heidelberg.

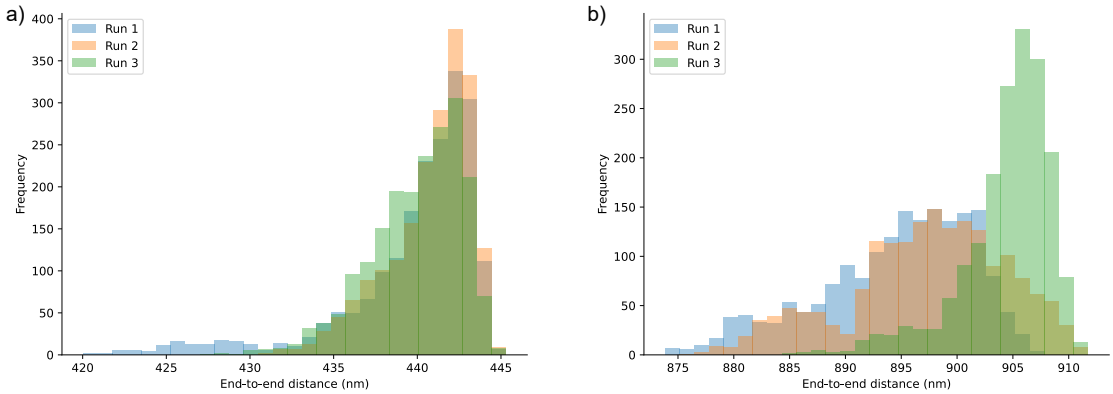

Figure 4.14: Results of the MD simulations. a) end-to-end distance of a single 6HB structure (6HB-Oxa1) and b) of a dimerized structure (6HB-Oxa1/Oxa/6HB-Oxa2). Details about the structures are given in section 4.3.2. The mean values are (440.1 ± 3.2) nm and (898.7 ± 6.2) nm, respectively. Calculations were performed by Erik Poppleton.

MD Simulations To investigate the dimensions and flexibility of the 6HB structures, MD simulations were performed by Erik Poppleton.[209–211,222–226] In a first step, the end-to-end distances of a single 6HB structure (6HB-Oxa1) and a dimerized structure (6HB-Oxa1/Oxa/6HB-Oxa2) were calculated (see section 4.3.2 for details about the structures used here). The results are shown in figure 4.14. While for the monomer, all three curves match nicely and give a mean length of (440.1 ± 3.2) nm, the end-to-end distance of the dimer structure is a bit less clear. However, the obtained mean length of (898.7 ± 6.2) nm is assumed to be a good estimate, since it matches nicely the doubled length of a single 6HB plus some more nanometers caused by the connecting analyte part.

Additionally, the flexibility of the 6HB structures was simulated as shown in figure 4.15. The 6HB are colored by their root-mean-squared-fluctuation (RMSF) per particle. The red colored ends of the structures are therefore – as can be expected – more flexible than the middle part. The maximum RMSF of 12 nm for the monomer shows – compared to the overall length of the 6HB – that the structures are quite rigid. The same holds for the dimer structure, that has a maximum RMSF of below 24 nm. According to the simulation, the thinner connecting part of the overhang-analyte bindings – consisting of only three instead of six double helices – does not have a striking impact on the flexibility of the dimer structure. It can be further observed that the structures have a small preferential curvature, which is assumed to be negligible.

Model of a stiff cylinder From the results of the MD simulations, the 6HB structure can be assumed to show a stiff geometry of around 440 nm in length and 6 nm in diameter. It can therefore in a simple geometrical model be treated as a stiff cylinder. Following this model, the translational diffusion coefficient can be calculated as following[227]

$$D = k_{\mathrm{B}}T(\ln p + \gamma) \cdot \frac{1}{3\pi\eta_0 L}, \tag{4.3}$$

where $p = L/2b$ is the axial ratio of cylinder length and b denotes the cylinder radius. The end-effect correction γ is given by eq. (75) in García de la Torre et al.[227] to be

$$\gamma = \frac{\gamma_{\parallel} + \gamma_{\perp}}{2} \tag{4.4}$$

$$\gamma_{\perp} = 0.50 + 4.2 \cdot \left(\frac{1}{\ln 2p} - 0.39\right)^2 \tag{4.5}$$

$$\gamma_{\parallel} = -0.58 + 7.4 \cdot \left(\frac{1}{\ln 2p} - 0.34\right)^2. \tag{4.6}$$

Using the dimensions obtained from the MD simulations, $L = 440\,\mathrm{nm}$ and $b = 3\,\mathrm{nm}$, an expected diffusion coefficient of $D_{\mathrm{monomer}} = 4.90 \cdot 10^{-12}\,\mathrm{m^2/s}$ can be calculated. This can be further transferred to an expected effective hydrodynamic diameter of $d_{\mathrm{h,\ monomer}} = 100\,\mathrm{nm}$ according to equation (2.6).

Since the MD simulations also show a low flexibility for the 6HB dimers, the same can be done for the dimer structure using $L_{\mathrm{dimer}} = 899\,\mathrm{nm}$. An expected hydrodynamic diameter of $d_{\mathrm{h,\ dimer}} = 174\,\mathrm{nm}$ can be calculated. As expected, this is not the doubled size of a monomer structure, but is larger by a factor 1.7. This shows that a clear separation of the two species (monomers vs dimers) in a diffusion or size measurement should be possible.

Combining Cylinder Model and TEM Data Finally, it is possible to combine the theoretical evaluation of the stiff cylinder model and the experimental values in form of the TEM statistics to predict the mean particle size of mixtures containing monomers, dimers, and multiples. The expected hydrodynamic size of the 6HB monomers and dimers is known from the stiff cylinder model, and the percentages of the monomers, dimers, and multiples can be estimated by counting of the TEM images. Combining both, the expected mean of the PSD can be modeled. This is done by summing up the sizes of

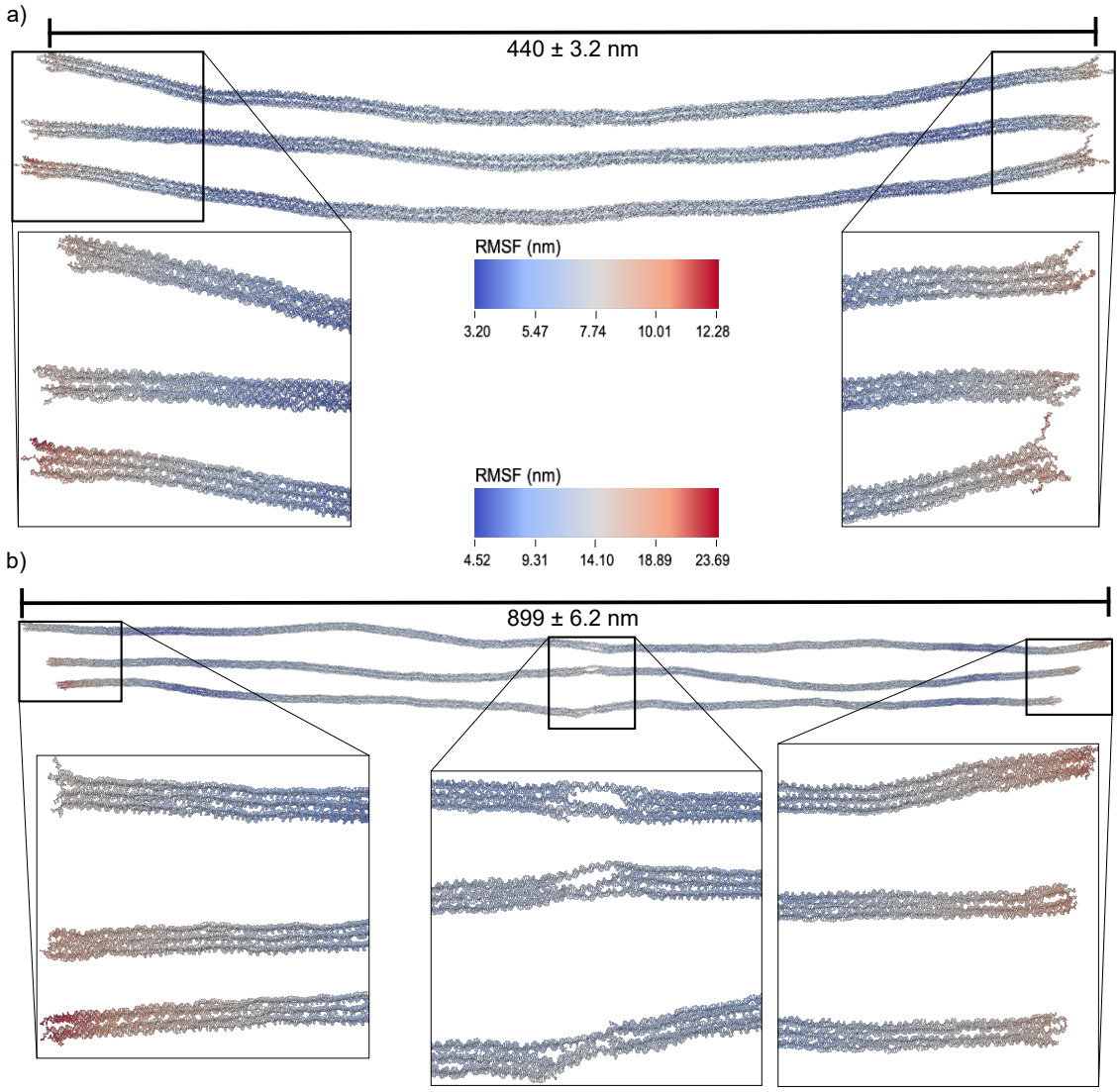

Figure 4.15: Results of the MD simulations. a) RMSF of a single 6HB structure (6HB-Oxa1). b) RMSF of a dimerized structure (6HB-Oxa1/Oxa/6HB-Oxa2) (bottom). Simulations were performed by Erik Poppleton.

Table 4.3: The first columns give the ratio of each species (monomers, dimers, multiples) as measured in the TEM statistics. The calculated size follows from adding up the sizes calculated by the stiff cylinder model, weighted by the ratio of each species. This is compared with the measured mean size that follows from NTA-FL measurements.

Sample	Monomers (%)	Dimers (%)	Multiples (%)	Calculated Size (nm)	Measured Mean Size (nm)
6HB-T	77.7	12.1	10.1	126	136
6HB-A	83.7	9.4	6.9	119	127
Dimers A+T	22.6	54.8	22.6	180	176

each component, weighted by their percentage. Only one parameter is missing for this procedure, which is the hydrodynamic size of a multiple. This is very hard to estimate, since the number of 6HB structures in the multiples ranges from three to larger numbers and their structure is variable. However, since the number of multiples is not too high according to the TEM statistics, this value should not be crucial. It is therefore set to 273.9 nm, which is the sum of monomer and dimer hydrodynamic diameter.

Summing up the size values of each component, weighted by its percentage for each sample gives the mean particle size expected for this sample. The results of these calculations are given in table 4.3 for the monomer samples 6HB-A and 6HB-T, as well as for the dimer sample of these two. The calculated mean size for the monomer samples is around 120 nm and increases clearly to a value of 180 nm for the dimers sample.

To test if these calculated values are reasonable, they are compared to the experimental PSD values measured by NTA-FL. It has to be noted, that the mean of the PSD curve has to be used here, since it represents all components present in the sample, including multiples. This is different to all other parts of this chapter, where the maximum value of the PSD is discussed, which depicts mainly the components that are present at high concentrations. The mean μ of the log-normal distribution as given in equation (4.1) is calculated as[228]

$$\mu = \exp\left(\ln(x_\mathrm{m}) + \frac{\sigma}{2}\right). \tag{4.7}$$

The mean of the NTA-FL measurements is given in the last column in table 4.3. The values slightly differ from the calculated values using the stiff cylinder model, but show

the same trend. For the monomer samples, the experimental values are bigger than the theoretical values, while for the dimer sample, the experimental value is smaller than the theoretical. This difference is assumed to be caused by the number of multiples. This number is hard to figure out exactly by the TEM statistics, since the structures in TEM are dried on the grid and might therefore form aggregates in a different way as they are present in solution for the diffusion measurements.

The calculation does not take care of some experimental details like the (small) flexibility of the 6HB structures, their behaviour in aqueous solution, or possible elongation by SYBR gold, as discussed above. However, the theoretical values clearly cover the trend of the experimentally observed sizes. We therefore find the stiff cylinder model to be a good approximation for the size measurements based on diffusion of the 6HB structures.

4.5 Analyte Sensing

The goal of this project is to sense an analyte DNA strand of well-known sequence by measuring the diffusion of 6HB DNA origami that can be connected in presence of the analyte, forming dimers with a slower diffusion coefficient than the monomers. In the last sections, it was shown that the increase in hydrodynamic size when 6HB structures are forming dimers is big enough to be detectable in diffusion measurements. For this, two species of 6HB were used that couple directly by their complementary overhangs, without the need for a connecting analyte strand. In the next step, the dimerization of 6HB via short analyte DNA strands is investigated. Therefore, two 6HB structures (namely, 6HB-IM1 and 6HB-IM2) were designed to bind a strand of the IM sequence as shown in figure 4.9. This idea is schematically depicted in figure 4.1, where the analyte strand is shown in light green, and the different colors of the overhangs stand for different DNA sequences.

In the following sections, not only the formation of dimers is discussed, which was investigated by TEM and NTA-FL, but the system was also tested under various conditions. Moreover, some ideas to further improve the method and make it more versatile are presented.

4.5.1 Dimer Formation using IM Strands

To couple the system consisting of 6HB-IM1, 6HB-IM2, and the IM strands, the IM strands were first added to 6HB-IM2 in a TA/$MgCl_2$ buffer. Both components were diluted to obtain a concentration of 2 nM in a volume of 20 µl. The suspension was cycled ten times between 25 °C and 32 °C, which is close to the expected melting temperature of IM stand and complementary overhangs of 6HB-IM2. The cycling protocol is the same as described for the coupling of 6HB-A and 6HB-T (see figure 4.11). After that, 20 µl of 6HB-IM1 in the same buffer were added to the mixture to obtain a 40 µl sample that contains 6HB-IM1, 6HB-IM2, and IM strands in a final concentration of 1 nM, each. The same temperature cycling protocol as described above was applied. This sample is referred to as the 'dimer' or '5 pM IM' sample in the following, where the concentration of 5 pM refers to the concentration of IM strands in the NTA-FL experiments. A second sample was prepared in the same way, using a threefold concentration of IM strands. Analogously, this will be referred to as the '15 pM IM' sample. As a reference sample, and to test for self-dimerization or unexpected binding of the two 6HB species, a 'monomer' or 'no IM' sample without the IM strands was prepared by applying the same procedure as for the dimer samples, leaving out the IM strands.

To validate the coupling of the 6HB-IM1 and 6HB-IM2 via the IM strands, TEM was performed in the same way as described in section 4.3.1. Two exemplary images are shown in figure 4.16, where figure 4.16a shows single 6HB structures in the monomer sample, and figure 4.16b represents the dimer sample. It can be observed that the folding of the structures is successful, and the coupling via the IM strand works. Similar as done for the 6HB-A and 6HB-T samples in section 4.4.1, the percentages of monomers, dimers, and multiples were examined by counting the structures in over 80 TEM images for each sample. This corresponds to a number of more than 700 structures for each sample. The results are shown in table 4.4. As can be seen, the sample without IM strands shows a low concentration of dimers (6.3 %) and multiples (5.1 %). These can be attributed to unstable coupling of small numbers of nucleobases in the overhangs, the mechanical generation of knots, and the drying process in the preparation of the TEM samples. The small percentage shows that the design of the overhangs is reasonable, so that self-dimerization or dimerization in absence of the analyte is neglibile. The number

Table 4.4: Amounts of the different species (monomers, dimers, multiples) of samples containing 6HB-IM1 and 6HB-IM2 and different amounts of IM strands. The Statistics are based on over 65 images and 700 counted particles for each sample. The first columns give the concentrations counted from TEM images. The calculated size follows from adding up the sizes calculated by the stiff cylinder model, weighted by the ratio of each species. This is compared with the measured mean size that follows from NTA-FL measurements.

Sample	Monomers (%)	Dimers (%)	Multiples (%)	Calculated Size (nm)	Measured Mean Size (nm)
no IM	88.6	6.3	5.1	113	130
5 pM IM	72.1	23.4	4.5	125	149
15 pM IM	48.5	35.2	16.3	154	161

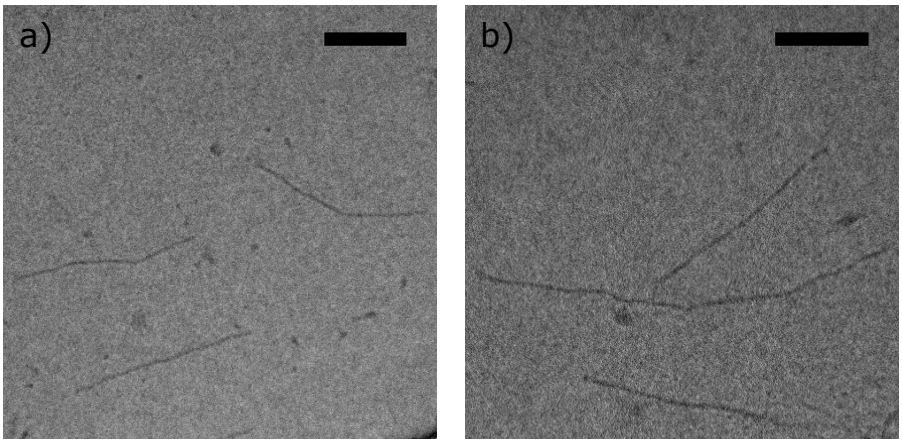

Figure 4.16: TEM images to investigate the dimer formation using IM strands. a) Monomer sample 'no IM', containing the origami structures 6HB-IM1 and 6HB-IM2. b) Dimer sample '15 pM IM'. Scale bar is 200 nm.

of dimers increases to 23 % for the 5 pM IM sample. This increase is less than for the control experiment using the 6HB-A and 6HB-T, where the ratio of dimers was nearly 55 % for the dimer sample. While in the latter case, the coupling happened directly between the origami overhangs, for the IM samples there is a third component present, which is the IM strand. For successful coupling, not only the two origami structures need to encounter in solution by means of diffusion, but also the analyte strand needs to meet the the origami structures to bind to them. This leads to an expected smaller probability of encountering and binding. Nonetheless, the formation of dimers clearly works as shown by the TEM statistics.

The stiff cylinder model can be applied for the IM system in the same way as discussed for the experiment using the 6HB-A and 6HB-T structures (see section 4.4.3). The results

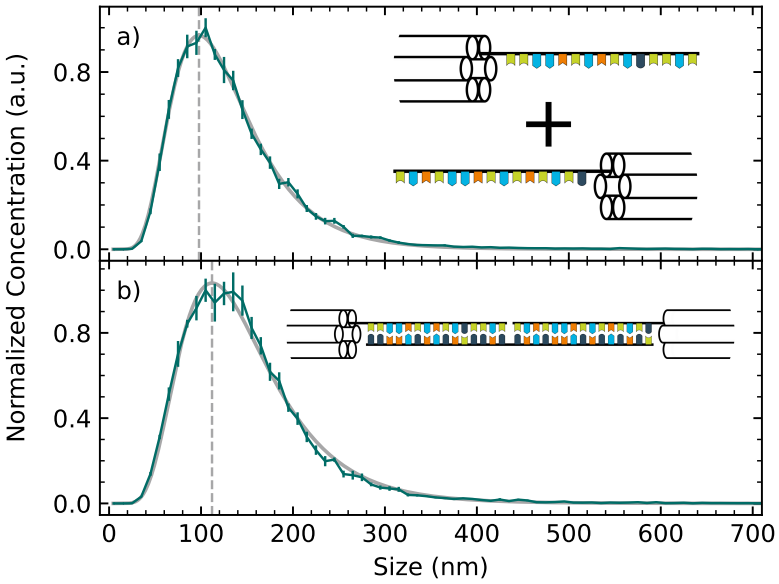

Figure 4.17: Measurement of the size shift by NTA-FL in the IM system when adding the analyte. a) Monomer sample 'no IM', which contains the 6HB structures 6HB-IM1 and 6HB-IM2. b) Dimer sample '5 pM IM', where the individual structures were dimerized by the IM analyte. All samples are measured at a concentration of 5 pM of both origami and IM strands (if present). Five measurements were performed and averaged per sample. The error bars represent the standard error of the five measurements. The maximum values obtained from the log-normal distribution (4.1) are $d_{\mathrm{max,monomers}} = (97.8 \pm 0.5)$ nm and $d_{\mathrm{max,dimers}} = (112.0 \pm 0.8)$ nm.

are shown in table 4.4. Here, the measured values are all larger than the theoretically calculated values. However, the trend is still reasonable and shows an increasing size for adding the IM strands.

In the next step, it has to be analyzed if the concentration of dimers that are forming in the presence of the IM strand is sufficient to see a change in diffusion. For this, NTA-FL measurements were performed on the monomer and the 5 pM IM samples. The samples were diluted to reach a final concentration of 5 pM of each DNA origami and IM strands, if present. The procedure was the same as described in section 4.4.2. The resulting PSD curves are shown in figure 4.17. The log-normal fitting function yields a maximum value of $d_{\mathrm{max,monomers}} = (97.8 \pm 0.5)$ nm for the sample without IM strands, which is close to the maximum of the distributions of the single monomers 6HB-A and 6HB-T as shown in figure 4.13. This again shows that there is no, or very little amount of dimerization of the origami structures in absence of the analyte. The 5 pM IM sample shows a clear shift in size, having a distribution maximum of $d_{\mathrm{max,dimers}} = (112.0 \pm 0.8)$ nm. As can

be expected from the TEM statistics (compare tables 4.3 and 4.4), the size shift is less pronounced than for the direct coupling of 6HB-A and 6HB-T. However, it shows that the binding efficiency is sufficient to see a change in the diffusion measurements. This system therefore allows for sensing of the IM strands by measuring the shift in size that is caused by the dimerization via the IM strands.

4.5.2 Concentration Dependence of the Size Shift

In the last section, it was shown that a random DNA strand can be detected by measuring the diffusion of 6HB DNA origami of the same concentration as the analyte. Another important question that comes up in this context is the binding efficiency when changing the analyte concentration with respect to the 6HB origami concentration. For this, samples of different IM concentrations were prepared following the fabrication discussed in section 4.5.1. The origami concentration was kept at 1 nM, while the IM concentration was varied from 0 nM to 20 nM. For the NTA-FL measurements, the samples were diluted to an origami concentration of 5 pM. Accordingly, the IM concentration varies from 0 pM to 100 pM. The name of the samples again refers to the concentration of IM strand after the dilution for the NTA-FL measurements.

Results of Concentration Series Figure 4.18a shows exemplary PSD curves of the different samples. It can be observed that the shape of the curve is nearly independent from the analyte concentration, while the maximum value shifts to bigger values for increasing analyte concentration. In figure 4.18b, the maximum values of the log-normal fit functions and their uncertainties are plotted with respect to the concentration of analyte at measurement conditions. The exact values are listed in the appendix in table A.3. The maximum size increases up to a concentration of 25 pM IM strands until the maximum size reaches a plateau. This behaviour is discussed in the following.

Every DNA origami has three binding overhangs of the same type that are complementary to a part of the IM strand. Each dimer can therefore incorporate three IM strands. Hence, it can be assumed that the ratio of dimers increases when increasing the IM strand concentration from 5 pM (1:1 ratio of IM and origami) to 15 pM (3:1 ratio). This behaviour is observed for our experiments as can be seen in table 4.4 and figure 4.18. The

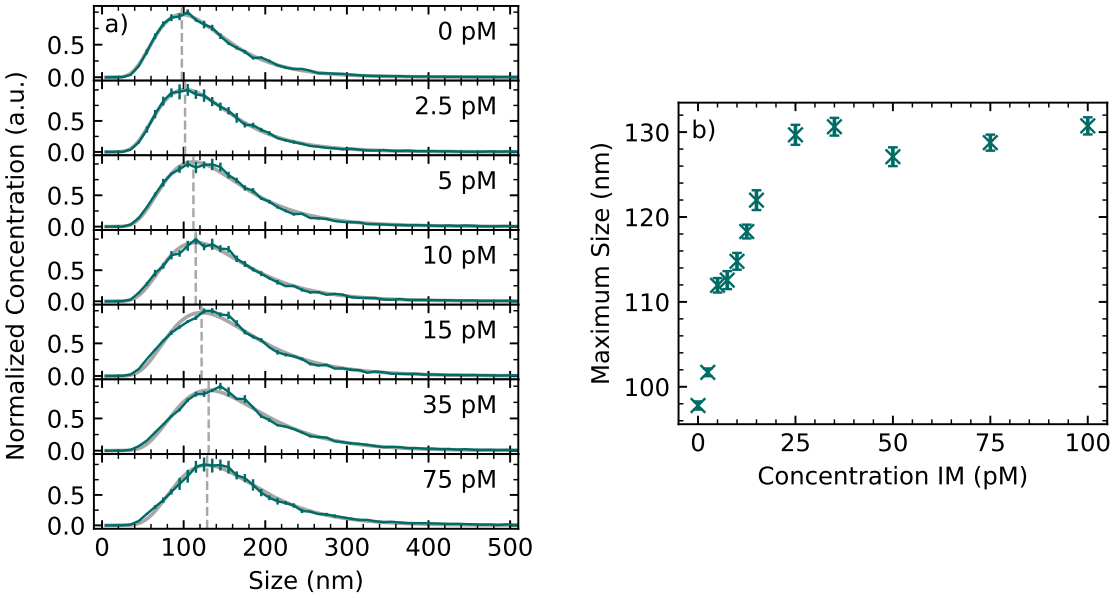

Figure 4.18: NTA-FL measurements on samples coupled by different amounts of IM strands. a) Exemplary measurements of samples containing 6HB-IM1 and 6HB-IM2, as well as different amounts of IM strands. The concentrations given refer to the concentration at the measurement, where the samples were diluted to 5 pM of each DNA origami structure. Five measurements were averaged for each sample. The error bars represent the standard error of these. The fits follow the log-normal distribution (4.1). b) The maximum values of the size distributions and their uncertainties as calculated from the fit with respect to the concentration of IM strands present in the sample after diluting for the NTA-FL measurements. The error bars represent the uncertainty of the maximum obtained from the fitting errors as explained in section A.2.1. A list of the exact values is given in table A.3.

number of monomers decreases from 72 % to 49 %, while the number of dimers goes from 23 % to 35 % when increasing the IM concentration from one- to threefold the origami concentration.

When further increasing the analyte concentration to above the 3:1 ratio, it can be expected that the high number of IM strands leads to a saturation of all available overhangs, which in turn can prevent the 6HB from coupling when all overhangs are occupied by IM strands. This expectation is further supported by literature, where this has been observed in similar cases.[53] This behaviour is not observed in figure 4.18 as we instead see a plateau of the maximum size for the higher concentrations of IM strands. This is assumed to be caused by a high number of mulitples that shift the size to higher values

than expected. This assumption is supported by table 4.4, where an increase in the number of multiples is observed when going from 5 pM IM to 15 pM IM strands.

Theoretical Evaluation using the global fit The concentration series shown in figure 4.18 can further be evaluated by the global fit model as described in section 4.2.4. Instead of fitting one log-normal distribution to each PSD, a sum of three distributions is fitted, each representing the species of monomers, dimers, or multiples, respectively. The size and standard deviation of each species are global fitting parameters, while the intensity of each species distribution is adjusted for every single measurement. Using this fit, a general size of each species can be calculated, as well as concentrations of each species for every measurement.

An example of the global fitting curves is shown in figure 4.19. The sample without IM strands and the measurement of the 15 pM IM sample are shown with their fit. The individual log-normal curves, that add up to the final fit curve, are also shown. It can be seen that from the first to the second plot the intensities of the dimer and the multiple curve increase, while the monomer curve becomes less intense. From the global fitting parameters, we obtain the hydrodynamic diameters $d_{\text{monomer}} = (91 \pm 2)\,\text{nm}$, $d_{\text{dimer}} = (142 \pm 1)\,\text{nm}$, and $d_{\text{multiple}} = (161 \pm 7)\,\text{nm}$. The percentages of each species as obtained from the intensities of the corresponding curves are shown in figure 4.19b with respect to the concentration of IM strands. As expected, the concentration of monomers decreases when increasing the IM concentration up to around 25 pM, while the percentage of dimers and multiples goes up. For the higher concentrations of IM strands the concentrations remain more or less constant, showing a high concentration of multiples between 40 % and 50 %. The fact that the multiples are dominating might explain the formation of the plateau in figure 4.18.

Using the global fit allows for a more detailed analysis of the results measured by NTA-FL compared to only focusing on the maximum of the PSD. However, the size shift of the maximum is the parameter that is easiest to access. It further does not need a series of measurements like the global fit to sense the analyte DNA strand when measuring and fitting individual samples. Therefore, the size shift of the maximum will be used again in the following to evaluate the measurements.

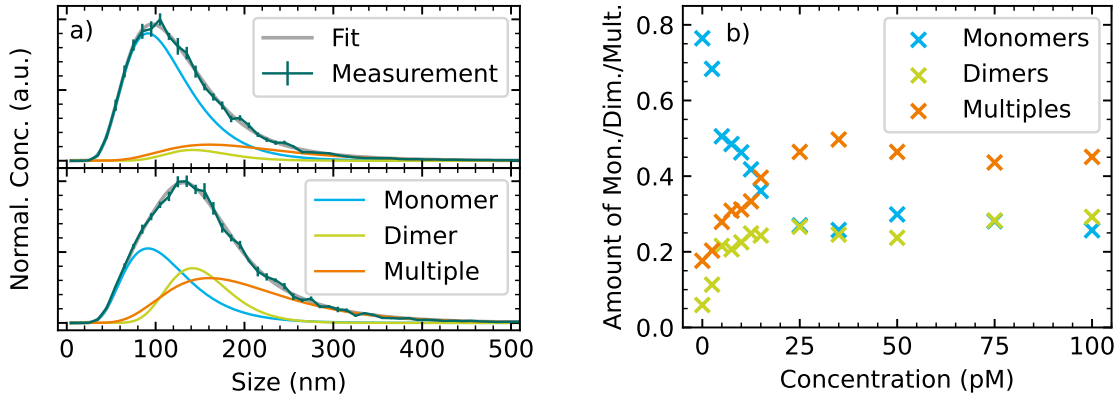

Figure 4.19: Evaluation of the global fit following equation (4.2) on the samples containing 6HB-IM1, 6HB-IM2 and variable amounts of IM strands. a) Exemplary representation of the fit to the NTA-FL measurements on the 'no IM' sample (top) containing monomers without the analyte and '15 pM IM' (bottom), where IM strands are added in a ratio 3:1 compared to the 6HB structures. b) Resulting numbers of monomers, dimers, and multiples for different concentrations of IM strands as obtained from the intensity values of each curve in the global fit.

4.5.3 Improving the System

Some practical considerations that have to be discussed in the context of the analyte DNA sensing are the lowest possible analyte concentration and the question, if the coupling process can be simplified. We first investigated, whether the temperature cycling can be avoided. We prepared samples of the 6HB-IM1, 6HB-IM2, and IM strands following the protocol given in section 4.5.1, but instead of the temperature cycling, the samples are left at room temperature for one hour. The NTA-FL measurements were performed as described above, using an origami concentration of 5 pM. The results are shown in figure 4.20b and can be compared with the results using temperature cycling as shown in figure 4.20a. The maximum values of the plots and their uncertainties are given in table 4.5. The size shift of the maximum is slightly less pronounced than for the measurements with temperature cycling, but is still significant. This means that one hour at room temperature is sufficient to form dimers that can be detected by diffusion measurements. The results shown here imply that for a practical implementation no machine for the temperature cycling is required.

From figure 4.18 it becomes clear that only 5 pM of IM strands are enough to generate a detectable size shift. This corresponds to a total amount of 5 fmol of analyte strands in

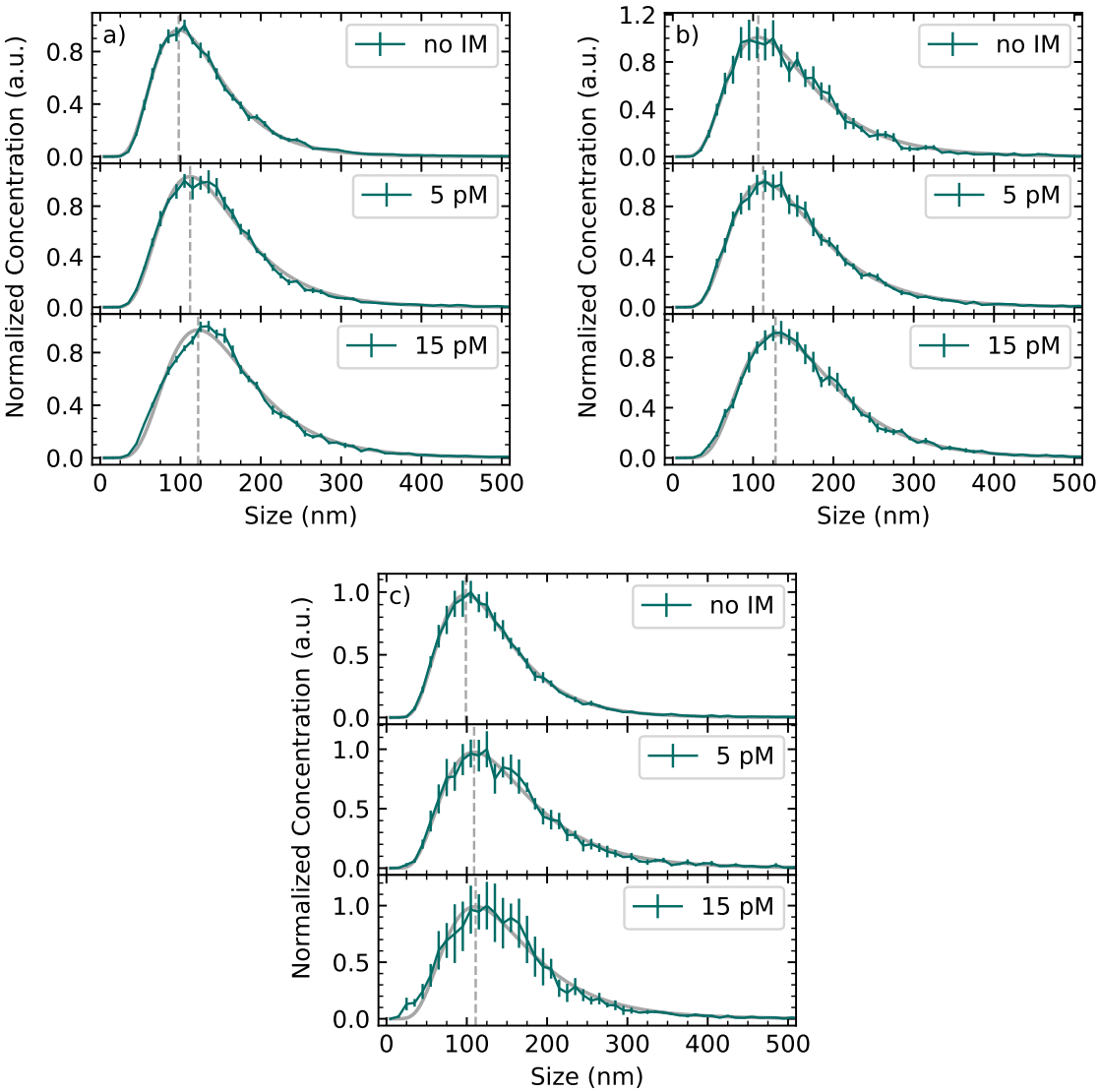

Figure 4.20: Size distributions as obtained from NTA-FL measurements on the system containing only 6HB-IM1 and 6HB-IM2 ('no IM'), and upon adding IM analyte in a ratio 1:1 ('5 pM IM'), or 3:1 ('15 pM IM') to the origami structures for different settings used for the coupling. a) Concentration of 6HB origami was 1 nM, temperature cycling was used. b) Concentration of 6HB origami was 1 nM, no temperature cycling was used. c) Concentration of 6HB origami was 10 pM, no temperature cycling was used. The measurements were performed at a origami concentration of 5 pM. Five measurements were averaged, with the error bars representing their standard error. The maximum values of the curves as obtained from the fit are given in table 4.5.

Table 4.5: Maximum values and their uncertainties as obtained from the log-normal fit following equation (4.1) for the samples shown in figure 4.20. All values are given in nanometers (nm). The header shows the coupling settings, i.e. the concentration of origami for the coupling and if temperature cycling (TC) was used.

Concentration	1 nM, with TC	1 nM, without TC	10 pM, without TC
no IM	97.8 ± 0.5	106.5 ± 1.2	98.9 ± 0.5
5 pM	112.0 ± 0.8	112.6 ± 0.7	109.1 ± 1.3
15 pM	122.0 ± 1.2	128.0 ± 0.9	111.1 ± 1.9

the 1 ml volume of the sample. However, these data have been acquired for samples that were coupled at concentrations of 1 nM and then diluted. To find out if the concentration for the coupling process can be reduced, we prepared samples of the IM system that were coupled differently to the settings given in section 4.4.1. A concentration of 10 pM of each origami species was used and 0 pM, 10 pM, or 30 pM of IM strands were added for the different samples. Same as for the aforementioned experiments, no temperature cycling was performed, instead the samples were left at room temperature for one hour. For the NTA-FL measurements, the samples were again diluted to 5 pM of DNA origami. The results of these measurements are shown in figure 4.20c. The maximum values of the log-normal fit and their uncertainties are listed in table 4.5. Again, the size shift is smaller than for the reference measurements, but a significant shift of the maximum in presence of the analyte is visible. This shows that successful detection of the analyte strand is possible at even smaller coupling concentration of around 10 pM.

4.5.4 Creating a Flexible System as a 'Detection Kit'

Another practical consideration for the DNA sensing method is the fabrication of a DNA origami 'detection kit' that is more flexible for application purposes. The idea behind this is to have an easy method to sense DNA strands of different sequences. In the method presented above, changing the analyte DNA sequence requires the folding of new origami structures with the corresponding overhangs, which is the most time-consuming part of the sensing method. We show that it is possible to use a basic set of 6HB structures, both having overhangs of 15 adenine bases, namely 6HB-A and 6HB-A' (see section 4.3.2 for details). Instead of coupling the two origami structures directly via

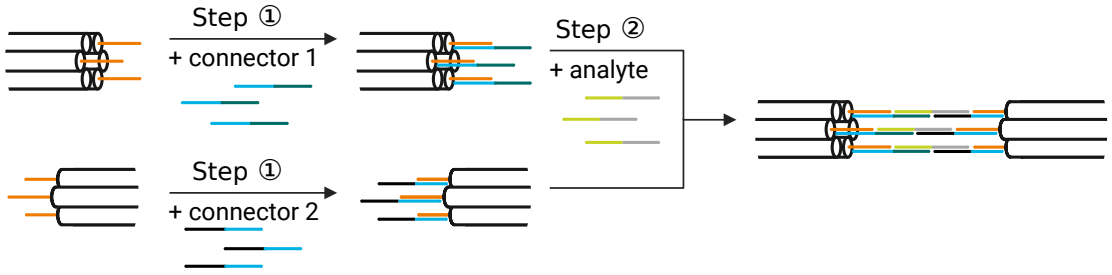

Figure 4.21: Schematic representation of the coupling process for the DNA origami 'detection kit'. The different colors denote DNA sequences, where the complementary parts of the strands are shown by the colour pairs light blue/orange, dark green/light green, and gray/black.

the analyte, two connector strands are introduced, which have 15 thymine bases and a sequence that is complementary to the IM strand (DNA sequences are given in section 4.3.2). The coupling procedure is schematically outlined in figure 4.21. The connector strands are first coupled to the corresponding origami structures at concentrations of 2 nM in 20 µl using the temperature cycling protocol (figure 4.11), adjusted by the lower and upper temperature of 27 °C and 34.5 °C. Using this method, the overhangs of the 6HB-A structures are extended to be complementary to the IM strand. The IM strand is then added to one of the solutions in the same way as described in section 4.5.1, before the solutions are added to form dimers. The system is now nearly the same as for the experiments shown in the lat sections, only a small 'spacer' of 15 bases was introduced by the connector strands.

Two samples, one without IM strands, the other one containing IM strands, were prepared as given in section 4.5.1 and measured by NTA-FL (compare section 4.2.2). The results are shown in figure 4.22. The error bars are more pronounced than for the IM sensing system that uses the 6HB-IM1 and 6HB-IM2 (figure 4.17). This assumed to be caused by the higher complexity of the system. However, a significant size shift from $d_{\mathrm{max,monomers}} = (111.4 \pm 0.9)$ nm to $d_{\mathrm{max,dimers}} = (122.4 \pm 1.6)$ nm can be observed, which means that this method is successful in detecting the analyte IM strand. This 'detection kit' allows for an easier change to sensing of another analyte structure, without the need to fold new 6HB structures.

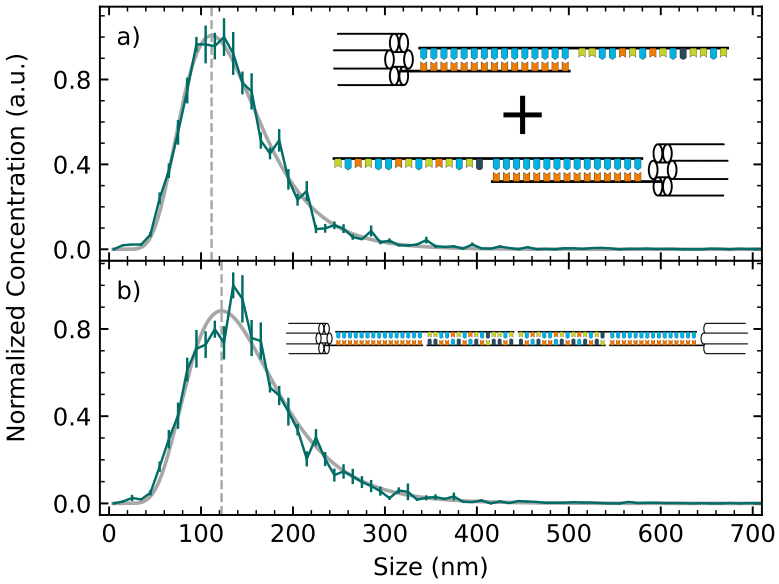

Figure 4.22: Measurements of a flexible system for analyte detection using connector strands between the IM analyte and the DNA origami overhangs. a) PSD measured by NTA-FL of a sample containing 6HB-IM1 and 6HB-IM2 and the coupled connector strands. b) PSD of the dimerized sample upon adding IM strands in the same concentration as the origami structures. Both samples were measured at an origami concentration of 5 pM. Five measurements were performed for each sample. The error bars show the standard error. The fit follows the log-normal distribution equation (4.1). The maximum values are $d_{\mathrm{max,monomers}} = (111.4 \pm 0.9)\,\mathrm{nm}$ and $d_{\mathrm{max,dimers}} = (122.4 \pm 1.6)\,\mathrm{nm}$.

4.6 Summary and Outlook

DNA origami shows well-defined shapes, is monodisperse, and highly reproducible. Using modification of chosen overhanging DNA strands, it further allows for specific binding to DNA of a known sequence. DNA origami can therefore serve as a precise nanosensor for diffusion measurements. The diffusion of fluorescently labeled structures can be measured sensitively and down to picomolar concentrations using NTA-FL. The PSD curves obtained from these measurements are narrow enough to measure size shifts of down to a few nanometers.

This can be used for fast and sensitive detection of a ssDNA analyte based on diffusion measurements of a specific DNA origami structure. In this thesis it was demonstrated that two 6HB nanosensors can be dimerized by an analyte made of ssDNA, if their overhangs are designed to be complementary to the analyte sequence. This leads to an

increase in the number of dimers in the sample suspension. By measuring the diffusion of fluorescently labeled DNA origami using NTA-FL, the presence of dimers can be observed by a shift in size, which traces back to the presence of the analyte. The size of the origamis and the size shift when dimers are formed is modeled by approximating the 6HB to stiff cylinders.

The method has been successfully applied to detect a random DNA sequence as presented in this chapter. Further, it has been shown that the process of coupling the 6HB structures and the analyte can be simplified and improved by coupling without temperature cycling and at lower sample concentrations, which delivers promising results. In another approach, a 'detection kit' is tested, which eliminates the need of time-consuming fabrication of new 6HB structures and provides 'ready-to-use' structures. By introducing connector strands that link the specific DNA sequence and the 6HB structures, a variety of analyte DNA sequences can be detected with the same 'detection kit'.

In most practical applications, the exact concentration of the analyte is unknown. As presented in section 4.5.2, the analyte can best be detected if its concentration is in the range of the nanosensor concentration. However, the following procedure should allow for DNA detection, even if the analyte concentration is much higher than the origami concentration. In this case, one of the origami structures is added in a known concentration to the unknown amount of analyte DNA. Using size exclusion filters, all unbound analyte strands are filtered out. By adding the second origami structure in the same concentration as the first one, the maximum number of dimers is obtained. This method should generate an ideal concentration of the nanosensors to obtain a maximum number of dimers, and hence the largest possible change in the measured diffusion coefficients.

The proposed procedure has been successfully applied to the IM sequence of picomolar concentration as discussed above, which represents a random 30 base DNA sequence. To test the method on a more realistic sample than a random DNA sequence, the case of antibiotic resistance was considered. An increasing number of antibiotics become inefficient due to antibiotic resistance. While this problem can temporarily be addressed by therapy with broad spectrum antibiotics, this will over time dramatically increase the incidence of antibiotic resistance. New methods for screening patients for antibiotic resistance are therefore of importance in medicine.[196,229,230] By choosing a DNA sequence from a suit-

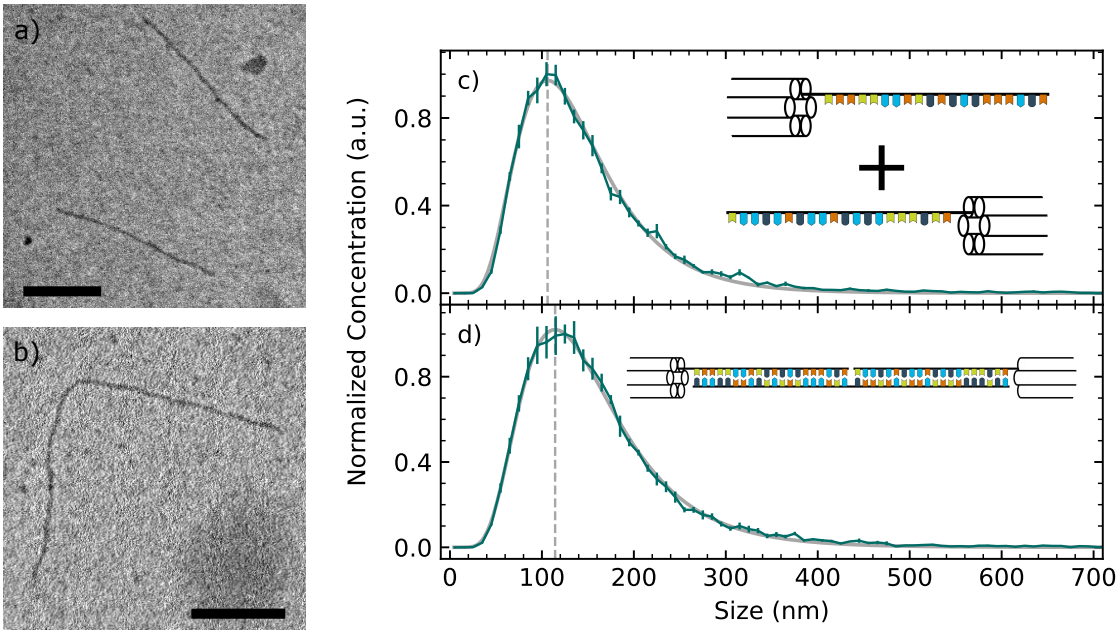

Figure 4.23: Validation of successful coupling of 6HB structures via the Oxa analyte. Monomer samples contain 6HB-Oxa1 and 6HB-Oxa2, for the dimer sample ('5 pM Oxa') they were coupled using Oxa strands in the same concentration as the origami structures. a) TEM of the monomer sample shows individual 6HB. b) TEM of the dimer sample shows a dimer, consisting of two connected 6HB. The scale bar for both figures is 200 nm. c) Size distribution of the monomer sample without Oxa strands, measured by NTA-FL. d) The size distribution of the dimer sample shows a size shift. Both NTA-FL measurements were performed at an origami and Oxa concentration of 5 pM. Five measurements were performed per sample, with the error bars representing their standard error. The maximum values obtained from the log-normal fit as given in equation (4.1) are $d_{\mathrm{max,monomers}} = (106.2 \pm 0.7)$ nm and $d_{\mathrm{max,dimers}} = (114.4 \pm 0.6)$ nm.

able antibiotic resistance gene, assisted by my colleague Izar Schärf, the proposed method is tested on a DNA sequence that is encoding medically relevant information.

The OXA-48 enzyme carbapenemase (UniProt: Q6XEC0) is of importance in antibiotic resistance due to its capability of inactivating beta-lactam and carbapenem antibiotics.[195–198] A 40 base sequence of the blaOXA48 gene, denoted as the Oxa strand, was therefore investigated using the diffusion based sensing method as outlined in this chapter. Its sequence, as well as the DNA origami structures 6HB-Oxa1 and 6HB-Oxa2, were defined in section 4.3.2. The nanosensors were designed to be complementary to the Oxa strand. To dimerize the 6HB structures via the Oxa strand, the coupling protocol as outlined in section 4.5.3 was applied, using 1 nM of each 6HB and the Oxa

strands. The sample was incubated at room temperature for one hour, after all components were added. TEM samples were prepared following section 4.3.1, and NTA-FL measurements were performed as described in section 4.2.2. The results of these measurements are shown in figure 4.23, where it is clearly seen that the dimer formation is successful in this system. The maximum sizes of the PSD curve, measured by NTA-FL as presented in figure 4.23c and 4.23d, show a shift from $d_{\mathrm{max,monomers}} = (106.2 \pm 0.7)\,\mathrm{nm}$ to $d_{\mathrm{max,dimers}} = (114.4 \pm 0.6)\,\mathrm{nm}$. This difference is slightly smaller than for the case of the IM strand system (see figure 4.17), but is still statistically significant. The method has thereby been shown to successfully detect a 40 base DNA sequence that serves as a marker for antibiotic resistance.

It has been shown that the diffusion of origami nanosensors can be used to directly and relatively quickly sense the presence of a biomarker DNA. The biomarker leads to a change in the diffusion coefficient of the nanosensors, which can be measured sensitively by NTA-FL and at a concentration down to the picomolar range. An overall amount of 5 fmol of analyte in a 1 ml aqueous solution is enough to be detected by the presented method. This chapter shows that diffusion of nanosensors is a sensitive and direct tool for sensing other nanoparticles or macromolecules and potentially also bacteria and viruses.

5 Nanoparticle Diffusion Measurements in Complex Media using ^{19}F PFG NMR

In this chapter, the possibility of measuring nanoparticle diffusion by PFG NMR in various media is presented in order to draw conclusions on diffusion mechanisms of nanoparticles and the structural properties of the environment. The concepts and results discussed in this chapter are the basis of a paper
Ida Bochert, Camila Vacas Betancourt, Dimitris Missirlis, Nicolás Moreno-Gómez, and Peer Fischer. "Absolute Measurement of Nanoparticle Diffusion Using 19F PFG NMR in Complex Media", that is being prepared for publication.

5.1 Introduction

The diffusion of nanoparticles in synthetic or biological hydrogels as well as in tissue is of importance in biological and biomedical processes like the delivery of drugs.[57,58,231–233] The polymer network hinders the mobility of the nanoparticles by steric, hydrodynamic, or non-covalent interactions.[69–74] Being able to investigate and understand diffusion mechanisms of nanometer to micron sized particles is a challenging task for colloid and interface science. Three-dimensional diffusion studies on nanoparticles are commonly performed by optical methods.[75–85] However, due to scattering and light absorption, these methods are not universally applicable in opaque or complex media.[86,87]

As will be shown in this chapter, PFG NMR can be used to measure absolute diffusion coefficients of nanoparticles of around 200 nm in different aqueous and complex media. The method is not light-based and therefore not dependent on the use of fluorescent labels. Instead, the signal from nuclear spins of the nanoparticles is used for the diffusion

measurements. PFG NMR therefore offers a label-free, non-invasive method that can measure diffusion in bulk media and is applicable even in optically opaque systems. Moreover, NMR is a direct, model-free method and inherently measures a large ensemble of nuclear spins. PFG NMR is commonly applied for the diffusion of molecules in a liquid. For the case of colloidal particles the effect of dipolar coupling complicates the collection of NMR signals.[119,123,135,234] While PFG NMR has been applied to investigate diffusion of nanoparticles in complex media on a small nanometer range by measuring the diffusion of molecules[73,74,88–96], the significance for larger scales on the order of tens of nanometers to microns is limited when using such small diffusing species. To probe diffusion in media of larger characteristic length scales, the investigation of bigger nanoparticles as diffusion nanosensors is of interest.

The microstructure of hydrogels is defined by parameters like porosity, fibre length and thickness, crosslinking density, or polymer conformation. Two characteristic parameters to define the structure are the mesh size and the pore size. While the pore size describes the size of the micro- to macroscale voids in the gel, the mesh size is defined as the distance between two neighbouring cross-links.[75,235] Different methods are applied to investigate these quantities. Direct detection methods range from SEM based techniques over confocal microscopy to atomic force microscopy. While they allow for visualisation and estimation of the pore size in both the dehydrated and the swollen state, all of them can only probe an area or a volume close to the surface.[236,237] The pore size or mesh size can further be estimated by indirect methods. SAXS (small-angle X-ray scattering) or SANS (small angle neutron scattering). Both methods can be used to obtain the size of the crosslink domains, but they require substantial modeling.[237] Using rheology measurements, the mesh size can be estimated from the storage modulus.[75,237] One of the techniques that is easiest to access is based on swelling experiments in conjunction with Flory-Rehner theory to estimate the mesh size. However, this is based on several assumptions and can therefore only be used to estimate the order of magnitude of the mesh size.[64,72,235,238,239] Finally, the diffusion of nanoparticles in a hydrogel can be analyzed to estimate the mesh size of a gel, which promises a non-invasive approach to assess the characteristic structure in bulk media.[69,71,235,240]

However, to be able to measure nanoparticles bigger than a few nanometers by PFG NMR, the problem of dipolar coupling has to be addressed. Prior studies tried to tackle

this problem by attaching polymer strands to the surface of the nanoparticles, which provide the needed number of detectable nuclear spins. Liposomes and particles with mobile surface chains of PEG or other polymers were also investigated.[144,241–243] While this was shown to work, it restricts the surface chemistry to the attached polymer chains and limits the possibility of surface modification. An alternative method presented in the literature makes use of particles mostly made of mobile polymer chains that therefore do not show dipolar coupling.[234,244]

Another strategy that offers a wide range of possibilities is the use of hollow particles that are filled with a liquid, which is trapped inside the nanoparticle. Here, the liquid molecules provide an adequate NMR signal. The diffusion of water-containing liposomes in aqueous solutions has for instance been studied by PFG NMR.[97–99] However, these particles are often leaky, which makes it difficult to draw accurate conclusions on the diffusion.[97–99,144,243] A liquid can also be encapsulated inside a polymeric shell. Oil-filled core-shell particles are stable and, if suspended in water, the different hydrophilicity of the liquids inside and outside prevent leaking. While this idea of using liquid filled particles is not new, up to now they have only been studied by flow-assisted PFG NMR due to their relatively large size which is in the micron range.[100–106] However, to mimic diffusive behaviour in biologically relevant systems and to measure diffusion of nanoparticles non-invasively, diffusion measurements without the need of using flow are of interest. We are not aware of a previous study that allows for non-invasive PFG NMR measurements in complex media on the scale of tens to hundreds of nanometers.

The principle of the diffusion measurements of liquid core particles in different media is presented schematically in figure 5.1. The molecules inside the liquid core of a particle, shown as a gray circle, provide a signal that consists of one (or more) sharp peaks in the NMR spectrum. If the particle diffuses, the molecules inside follow the displacement of the particle shell, creating an attenuation of the peak intensity. The magnitude of the attenuation is dependent on the covered distance, which can be used to calculate the diffusion coefficient of the whole particle. If the particles are located in a medium of higher viscosity or in the presence of obstacles, the diffusion is slowed down, which is observed from a smaller attenuation of the NMR peak. The signal of the liquid core can therefore be used to measure the diffusion coefficient of the particle itself by PFG NMR.

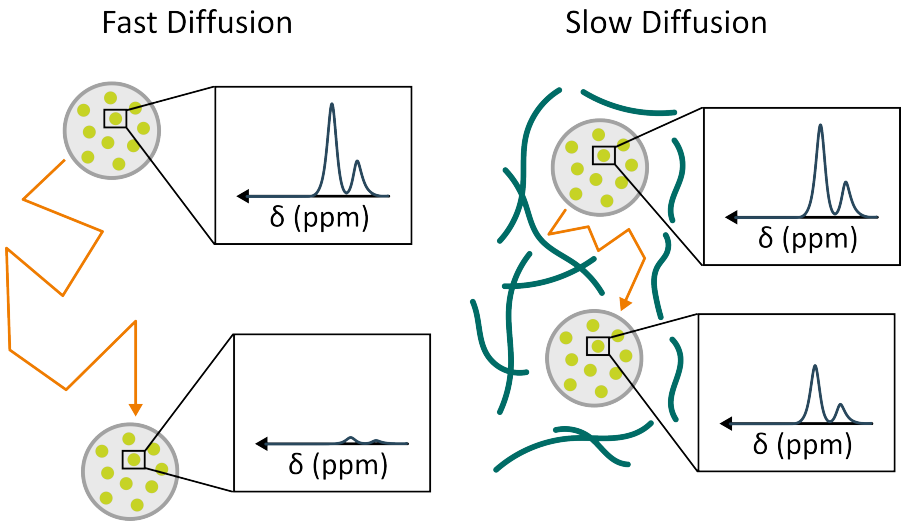

Figure 5.1: Schematic explanation of the measurement principle for diffusion measurements of liquid core nanoparticles using PFG NMR. The shell of the particles is shown in gray, and the light green dots represent molecules of the liquid in the core. These molecules provide an 'NMR active' signal that generates one (or more) sharp peaks in the NMR spectrum. Their attenuation is dependent on the mean covered distance of the particles, which allows for the measurement of fast or hindered diffusion. On the right-hand side, the green lines schematically represent fibres of a hydrogel that slow down the particles' diffusion.

Section 5.2 outlines a suitable particle system based on oil-filled core-shell particles[165] that is robust and shows a strong NMR signal, hence making them an attractive choice for the use as diffusion nanosensors in PFG NMR. The fabrication and characterization are presented. The presence of different 'NMR active' species is described and their role in measuring the diffusion of the particles is discussed. Finally, limitations of the system arising from relaxation times of the nuclear spins, as well as possible effects that restrict the useful measurement range are summarized.

The diffusion measurements of the particles in aqueous solution by PFG NMR can be observed to give well-defined diffusion coefficients that can also be used for an evaluation of size distributions as presented in section 5.3. To show that the supposed method allows for the determination of systemic parameters like viscosity or microstructure, the diffusion of the particles is measured in aqueous glycerol solutions of different concentrations as shown in section 5.4. Finally, the diffusion in a complex polymer network of hyaluronic methacrylate (HAMA) gel is investigated. The results suggest that the proposed method

can be beneficial in the evaluation of diffusion mechanisms of nanoparticles in hydrogels and in the estimation of microstructural parameters like the mesh size.

5.2 Characterization of the Nanoparticle System

Liquid filled particles provide a core that offers a nuclear spin signal that can be used to measure the diffusion of the whole particle. However, there are some requirements and limitations about this system, which are discussed in this section. The fabrication used for the nanoparticles discussed in this chapter is outlined, as well as different methods to characterize the nanoparticles and their diffusion by PFG NMR.

5.2.1 Requirements of a Diffusion Tracer in PFG NMR

Performing diffusion measurements by PFG NMR requires the particles to contain 'NMR-active' nuclear spins. As a rule of thumb, around 10^{18} nuclear spins in a total sample volume of 500 µl are known to give good results in PFG NMR. On the other hand, the particle concentration must not be so high that particle-particle interactions and collisions dominate the movement of the particles. Therefore, the number of 'NMR-active' nuclear spins per particle has to be maximized. Another requirement on the particles for potential future experiments is chemical variability of the surface to allow for the investigation of different interaction mechanisms between particles and their surrounding.

For other methods to measure particle diffusion, solid nanoparticles can be utilized.[123] However, this is not possible for PFG NMR, since the particles do not show enough 'NMR-active' spins. The dipolar coupling (as discussed in section 2.2.1) of all spins inside the particle (i.e. except for the surface molecules) leads to broadening of the NMR signal, which makes it hard to perform PFG NMR on such systems without modification of the particles.[234] Performing NMR with magic angle spinning, as done in solid state NMR[135], also should not allow for diffusion measurements on solid colloids, since they reorient on shorter timescales than the diffusion measurements are performed, which is expected to cancel the effect of the magic angle spinning.

Some diffusion NMR experiments have therefore been reported for particles whose 'NMR-active' nuclear spins are located in chains at the surface.[144,241–243] However, this does not

fulfil the requirement of a chemically functionalizable surface since the chains cannot be removed. Another approach is therefore to fabricate liquid filled particles and use the nuclear spins in the liquid core for the NMR experiments.[97–106] As long as the liquid is trapped inside the particle, the nuclear spin of the liquid molecules can be used as a tracer to measure the diffusion of the whole particle.

Some liquid filled particles have been used in the context of diffusion NMR.[97–106] These include liposomes, but many of these studies emphasize that there is fast exchange between the liquid on the inside and the outside.[97–99,144,243] Therefore another method of fabricating liquid filled particles is needed.

As discussed previously[100–106], promising particles for diffusion NMR are oil-filled core-shell particles, as described by Loxley and Vincent in 1998[165]. In the following, this type of particle will be denoted as 'liquid core particles'. A detailed description of the fabrication method is given in section 3.2. In short, a polymer shell is formed around an oil, which is hexadecane. This has the advantage that the core liquid – unlike the hydrophilic liquid surrounding the particles – is hydrophobic. Hence the two liquids show a lower affinity to mix, which can be assumed to lead to a lower leakiness of the particles compared to liposomes.

The original recipe leads to particles in the micron size range.[165] However, we aimed for particles in a size range of 100 nm to 300 nm in diameter to optimize results by PFG NMR. The fabrication of liquid core particles is very sensitive to the individual components and processes.[165–169] It is therefore important to find good working conditions and to carefully modify the particles. Slightly changing the fabrication process cannot only lead to different particle sizes, but also to various particle morphologies, like acorn-shaped particles, inverted core-shell particles, or even separated droplets. Different parameters in the fabrication have therefore been tested and improved. These tests were done by my colleagues Dr. Nicolás Moreno-Gómez and Camila Vacas Betancourt. Starting from the method outlined by Loxley and Vincent[165], it was possible to reduce the particle size by changing the temperature during homogenization, reducing the amount of hexadecane, and increasing the energy of the homogenization process by introducing ultrasonic dispersion. We further decided on adding a fluorinated silane, namely 1H,1H,2H,2H-Perfluorooctyltriethoxysilane, to the hexadecane mixture to include a fluorinated com-

ponent in the particle core that therefore shows a signal in the ^{19}F NMR spectrum. It will be denoted as SilF7 in the following. The molecule is soluble in hexadecane and shows a high number of ten chemically equivalent fluorine nuclei per molecule, making it a suitable tracer for ^{19}F NMR. The chemical structure of this molecule in shown in figure 5.4d.

The final protocol yields particles of around 200 nm in diameter, as will be investigated in the following sections, and follows the procedure outlined in the appendix (section A.1.2). The hexadecane and SilF7 provide nuclear spins that show sharp and intense peaks in the ^{1}H and ^{19}F NMR spectra, respectively, as will be discussed in section 5.2.3. Since the liquid is trapped inside the particle shell and follows its diffusion, the long-time diffusion can be assumed to mimic that of the whole particle. As will be shown in the following sections, particles fabricated by this method allow for accurate diffusion measurements by PFG NMR.

5.2.2 Analysis of Nanoparticles

To validate the successful particle fabrication of liquid core particles using the aforementioned fabrication method, different methods can be applied. SEM is used for visualization, while DLS and NTA allow for measuring the particle size distribution and the concentration.

Validation of successful fabrication by SEM The hexadecane and SilF7 filled PMMA particles were visualized by SEM to draw conclusions on their size and shape. For this, the particles were diluted in water to obtain a final concentration of $2 \cdot 10^8$ particles/ml. 10 µl of the diluted sample was transferred on a silicon wafer, allowed to completely dry, and finally sputtered with a 3 nm iridium layer. The sputtering, as well as the imaging was performed by Ulrike Waizmann and Bernhard Fenk from the Nanostructuring lab at Max Planck Institute for Solid State Research.

An exemplary SEM image of hexadecane and SilF7 filled PMMA particles is shown in figure 5.2. It can be observed that a nearly spherical shape can be achieved using this fabrication method. Because of the spherical appearance of the particles, in the context of this chapter all sizes determined as a hydrodynamic radius R_h of these particles are

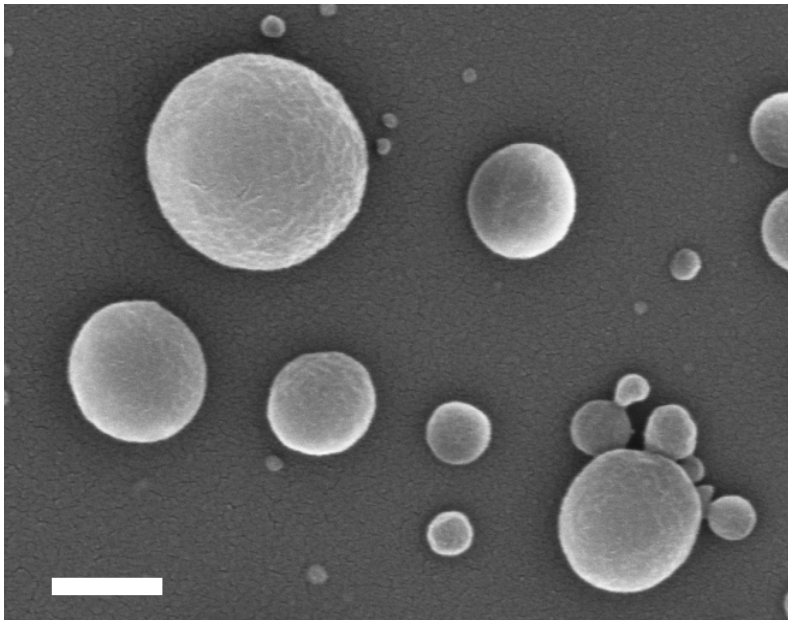

Figure 5.2: SEM on the liquid core nanoparticles filled with hexadecane and SilF7 and diluted in water shows successful fabrication. The particles were dried on a silicon wafer and sputtered with iridium. The sputtering and imaging was performed by the Nanostructuring lab at Max Planck Institute for Solid State Research. The scale bar is 200 nm

treated as the 'real' particle radius R. The surface of the particles appears to be slightly structured. However, the size is not very uniform, showing particle diameters ranging from around 30 nm up to 400 nm. This polydispersity can be analyzed in more detail by DLS and NTA.

Measurement of particle size by DLS and NTA To further verify the successful particle fabrication and evaluate the particle size, the PSD was measured by DLS and NTA. For DLS, the stock solution was diluted in water by a factor 1000. The measurements were performed on a *Malvern Zetasizer Nano Z* using a scattering angle of 173° and a temperature of 25 °C. The number-weighted hydrodynamic diameter was calculated as the average of ten measurements. For NTA, the particles were diluted in water by a factor of 10 000. Using a flow speed of 2.4 µl/s, the movement was recorded two times for 3 min. A camera level of 11, detection threshold of 10, blur 5x5, max jump distance of 20, and min track length of 8 were used.

The resulting number-weighted PSD curves are shown in figure 5.3a and 5.3b. Both measurements show one population, represented by a single maximum. This is – in

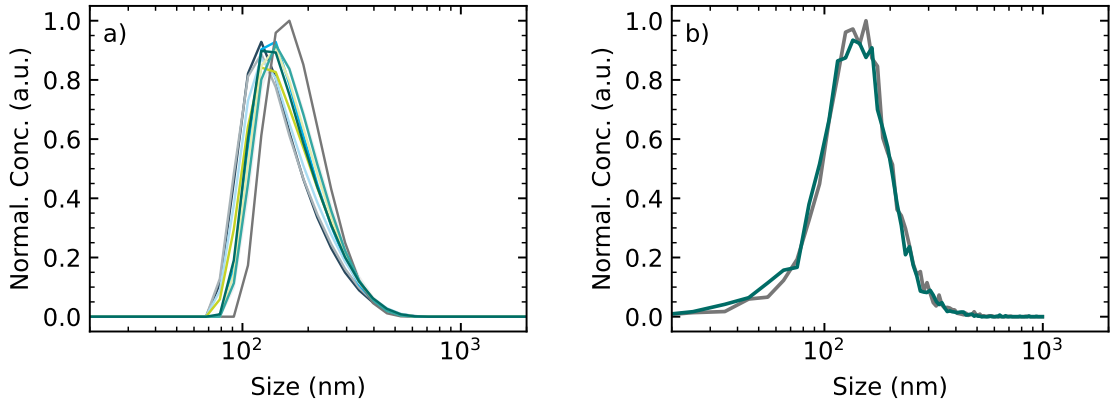

Figure 5.3: Size measurements of liquid core particles using optical methods. The particles consist of a PMMA shell and a core of hexadecane and SilF7. a) Number-weighted PSD as obtained by DLS. The particle stock solution was diluted to around $5 \cdot 10^9$ particles/ml. Ten measurements were performed and are shown. The mean of the curve is $d_{\mathrm{DLS}} = 170\,\mathrm{nm}$. b) PSD measured by NTA on a sample containing around $5 \cdot 10^8$ particles/ml. Two measurements of 3 min were performed. The mean diameter is $d_{\mathrm{NTA}} = 166\,\mathrm{nm}$. Both plots are normalized to the maximum of the most intense curve.

addition to the SEM pictures – an indication for the successful fabrication of the liquid core particles. The mean values of both curves agree well with each other and show values of $d_{\mathrm{DLS}} = 170\,\mathrm{nm}$ and $d_{\mathrm{NTA}} = 166\,\mathrm{nm}$. The shape of the curve, especially representing the amount of particles in the size range around 300 nm, shows slight differences. These can be assumed to be caused by the different methods of measurement and the used settings in the evaluation.

Measurement of particle concentration by NTA The NTA method further offers the possibility to evaluate the particle concentration. The conditions used for these measurements were the same as for the size measurements mentioned above. Concentrations of the stock solutions between around $2 \cdot 10^{12}$ particles/ml and $7 \cdot 10^{12}$ particles/ml were obtained for different batches. For the PFG NMR measurements shown in this chapter, the stock solution was always diluted in water to $5 \cdot 10^{11}$ particles/ml, unless otherwise specified. Given the particle size as measured by DLS and NTA, this concentration corresponds to a volume fraction of around 0.13 %.

To estimate, whether collision processes could play a role at these concentrations, the collision of gas molecules is taken as a reference. The particles are modeled as smooth, rigid, and elastic spheres that only interact by collision. The mean free path length can

be estimated to be in the range of 15 µm by considering the radius and concentration of the particles.[245] Estimating the mean covered distance $\sqrt{\langle r^2 \rangle}$ of the particles at room temperature in water using equations (2.4) and (2.6) yields values between around 450 nm and 3.7 µm for the diffusion times between 12 ms and 800 ms investigated in this chapter. These are much smaller than the mean free path length. Therefore, collisions are assumed to be negligible in the present system.

5.2.3 NMR Spectra

The just introduced liquid core particles are intended to be investigated by (PFG) NMR. For this, knowledge about the different chemical components present in the sample is important to evaluate the NMR spectra. In the environment of the samples, there is water and a small amount of SDS. Other samples discussed later might also contain glycerol, or HAMA polymer and other chemicals going along with the hydrogel. The particle shell consists of PMMA. The core is filled with hexadecane and SilF7. A schematic overview of these components is shown in figure 5.4a. A colour coding is introduced here for the NMR spectra.

NMR spectra of different samples are shown in figure 5.4. They were recorded using particle concentrations of $4.1 \cdot 10^{11}$ particles/ml (for 5.4b), and $5 \cdot 10^{11}$ particles/ml (for 5.4c and d). For the ^{1}H spectra, eight scans were recorded, while for the ^{19}F spectrum, 64 scans were performed. Since for PFG NMR, an exact knowledge of the chemical shift is not important, no reference standard is used. The only requirement in PFG NMR is to be able to associate each peak with the corresponding chemical component. For this, a rough adjustment of the x axis is sufficient. The water peak is therefore used as a reference and shifted to a chemical shift $\delta = 4.8$ ppm. This is done for all NMR spectra shown in this chapter. An ^{1}H NMR spectrum of the particles in 0.2 % SDS solution is shown in figure 5.4b. As expected from the high amount of water, the water peak at a chemical shift of $\delta \approx 4.8$ ppm is dominant in the spectrum. The triplet at $\delta \approx 4$ ppm, as well as the peaks at $\delta \approx 1.7$ ppm, $\delta \approx 1.3$ ppm, and $\delta \approx 0.9$ ppm are assumed to be caused (amongst others) by SDS.[246] The peaks are assigned to the different parts of the chemical structure as shown in the spectrum. The last two peaks, namely the ones at $\delta \approx 1.3$ ppm and $\delta \approx 0.9$ ppm overlap with the hexadecane signals.[247] The intensity

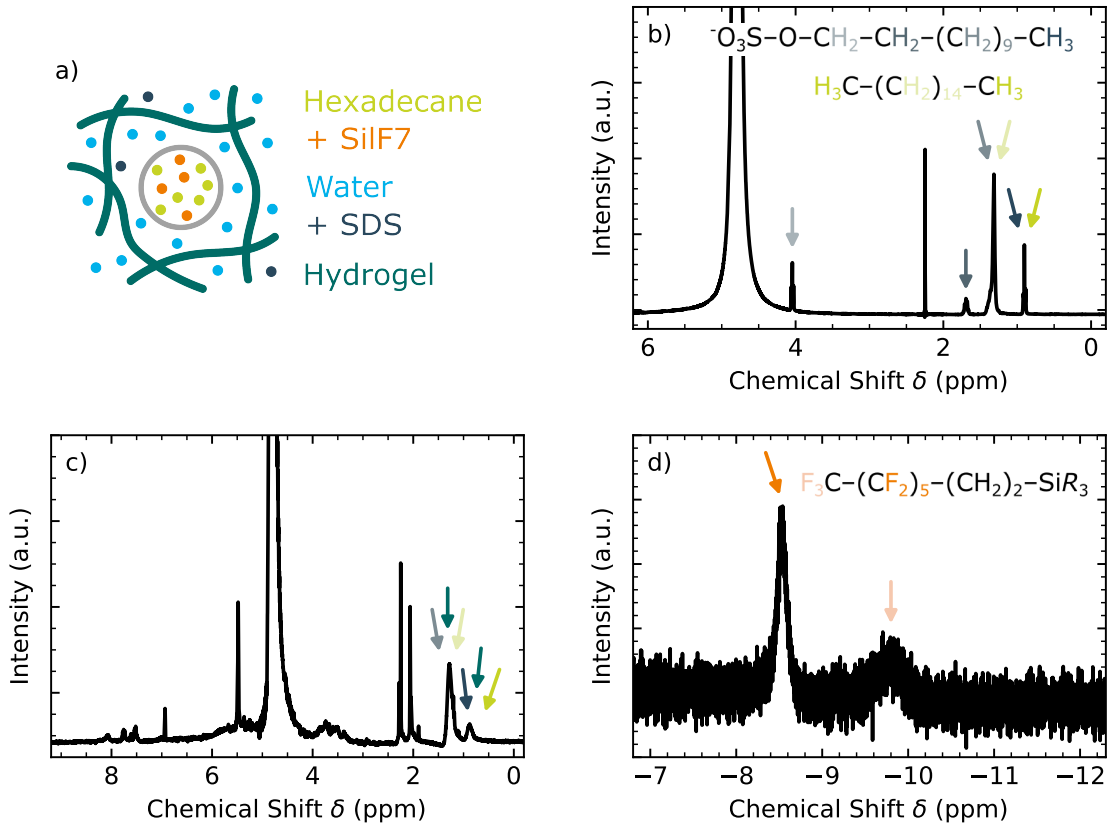

Figure 5.4: NMR spectra of the liquid core particles in different environments. a) Colour coding of the arrows shown in the spectra. The dots represent liquid molecules. b) ^{1}H NMR spectrum of particles containing hexadecane, dissolved in 0.2 % SDS solution at a concentration $4.1 \cdot 10^{11}$ particles/ml. Eight scans were performed and summed. The chemical structures shown in the plot represent SDS (top) and hexadecane (bottom). The peaks are assigned by colored arrows to the different hydrogen atoms in the molecules. c) ^{1}H NMR spectrum of particles in a 1 % HAMA hydrogel at a particle concentration of $5 \cdot 10^{11}$ particles/ml. The liquid core contains hexadecane and SilF7. Eight scans were performed. While the peaks of hexadecane and SDS are still visible, there might be overlapping peaks caused by the hydrogel. d) ^{19}F NMR spectrum of particles in water. The particle core consists of hexadecane and SilF7. The particles were diluted to a concentration of $5 \cdot 10^{11}$ particles/ml. 64 scans were performed. For the structure of SilF7 given in the plot, R stands for the 'rest' that is not relevant here, which is an $-O-CH_2-CH_3$ chain.

of the peaks is therefore the sum of the SDS and the hexadecane concentration. The spectrum shown here does not contain SilF7. When diluting the particles in water as done in the experiments decribed below, the concentration of SDS becomes smaller and the intensity of the SDS peaks decreases. A small amount of SDS is always present due to the fabrication process. However, the question might arise how the hexadecane and the SDS can be distinguished in the diffusion measurements. This important question will be answered in section 5.2.4.

While it is easy to distinguish and assign the peaks to the chemical components in the sample in water or SDS solution, the case of particles in a hydrogel becomes much more complex. An ^{1}H NMR spectrum of particles in 1 % HAMA gel is shown in figure 5.4c. As can easily be seen, this spectrum is very crowded, and the peaks cannot readily be assigned to the different chemicals present. This is caused by the more complex molecules present in this sample, that show many chemically different hydrogen atoms, which gives rise to peaks at various chemical shifts in the spectrum. There are peaks visible at $\delta \approx 1.3\,\text{ppm}$ and $\delta \approx 0.9\,\text{ppm}$, which can be assumed to be caused by the hexadecane. However, it is not guaranteed that the peaks are only caused by hexadecane (and SDS) and that they do not contain contributions from the hydrogel. Therefore, it is not possible to reliably measure the diffusion inside a complex environment like a hydrogel by ^{1}H NMR.

Instead, a fluorinated liquid component can be introduced to the core of the particles, so that it can serve as a distinct tracer for the diffusion of the particles. This is done here by adding SilF7 to the hexadecane. Figure 5.4d shows a ^{19}F NMR spectrum of the particles in water. Two peaks are visible, the more intense one belonging to the nuclear spins of the CF_2 chain, the smaller peak from the trifluoromethyl group CF_3 of the SilF7 molecules.

5.2.4 Diffusion Measurements by PFG NMR

The method of PFG NMR allows for label-free and non-invasive diffusion measurements and is used in the context of this chapter to measure the diffusion of around 200 nm sized liquid core particles. As discussed above, this is only possible due to the liquid molecules in the core of the particles, which provide the 'NMR-active' nuclear spins needed for

using the particles as diffusion tracers and nanosensors. Because of the smaller size of the liquid molecules compared to the particle radius, their diffusion is much faster than the diffusion of the particles themselves according to the SES equation (2.6). However, the movement of the liquid is limited to the space inside of the particle shell as described in section 2.1.2 and follows the diffusion of the particle for long enough diffusion times. The hexadecane and SilF7 are therefore assumed to serve as tracer molecules to measure the diffusion of the particles.

As described in section 2.2.1, in the process of a PFG NMR experiment, spectra of the sample are recorded for different magnetic field gradient strengths. An exemplary 'waterfall' plot of the stacked ^{1}H NMR spectra is shown in figure 5.5a. The sample used here contains liquid core particles suspended in a 0.2 % SDS solution using a concentration of $4 \cdot 10^{11}$ particles/ml. 128 scans were performed. By measuring the intensity of a peak using the area below the peak, the diffusion coefficient of the corresponding chemical component can be calculated following equation (2.17). The faster the peak decreases with increasing gradient strength, the faster is the diffusion of this component. In the case of the hexadecane trapped inside the particles, and SDS moving freely outside the particles, it can be assumed that the diffusion coefficient of SDS is larger than that of the hexadecane. This is experimentally verified as shown in figure 5.5. The peaks at $\delta \approx 4\,\text{ppm}$ and $\delta \approx 1.7\,\text{ppm}$, which belong to SDS, decrease within the first few applied gradient strengths, as does the water peak, which attenuates even faster. Since an SDS molecule is bigger than a water molecule, its diffusion coefficient in the same environment is slightly smaller according to equation (2.6). The peaks at $\delta \approx 1.3\,\text{ppm}$ and $\delta \approx 0.9\,\text{ppm}$, which can be assigned to both the hexadecane and the SDS, attenuate much slower with increasing gradient strength. This indicates a smaller diffusion coefficient. However, since the peaks of hexadecane overlap with peaks generated by SDS, a fast decay attributed to the overlying fast diffusion of SDS can be observed for the smaller gradient strengths.

To measure the diffusion coefficient quantitatively, the area under the peak at $\delta \approx 1.3\,\text{ppm}$ is plotted with respect to the parameter b, which contains the gradient strength squared as given in equation (2.18). This is shown in figure 5.5b. For a single chemical component, the measured values are assumed to follow a single exponential decay according to equation (2.17), which is represented as a linear slope due to the logscale on the y axis. The case shown here is different, due to the overlapping peaks of SDS and hexadecane.

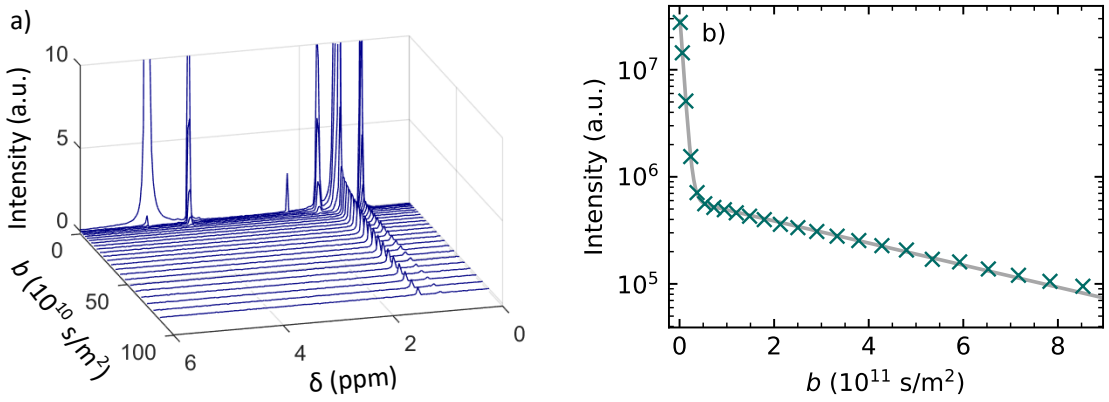

Figure 5.5: ^{1}H PFG NMR measurements on liquid core particles suspended in a 0.2 % SDS solution in a concentration of $4.1 \cdot 10^{11}$ particles/ml. The liquid core of the nanoparticles contains hexadecane. The PFG NMR experiment was performed using $\Delta = 23\,\text{ms}$, $\delta_g = 4.1\,\text{ms}$, and performing 128 scans for each gradient strenght. a) Stacked spectra that were recorded for different gradient strength as given by parameter $b \propto g^2$. While the peaks assigned to water and SDS decrease within a few gradient strengths, the peaks at $\delta \approx 1.3\,\text{ppm}$ and $\delta \approx 0.9\,\text{ppm}$ assigned to hexadecane show a slower attenuation, indicating a slower diffusion coefficient. Since they overlap with SDS peaks, an overlying fast diffusion can be observed for the first values of b. b) The area under the peak at $\delta \approx 1.3\,\text{ppm}$ is calculated and plotted with respect to parameter b. A bi-exponential attenuation can be observed, which is fitted with a sum of two exponential decays as given in equation (2.17).

Therefore, a sum of two exponential decays is fitted here, describing two species with different diffusion coefficients. From the fitting parameters of the bi-exponential decay, the diffusion coefficients $D_1 = (1.51 \pm 0.15) \cdot 10^{-10}\,\text{m}^2/\text{s}$ and $D_2 = (2.38 \pm 0.04) \cdot 10^{-12}\,\text{m}^2/\text{s}$ can be derived (calculation of the uncertainties is discussed in section A.2.1). The faster D_1 belongs to the diffusion of SDS in water, while the slower D_2 describes the displacement of the hexadecane molecules and therefore the diffusion of the particles. In the experiments shown in the following chapters, the amount of SDS is reduced, so that the peak is mostly caused by hexadecane. However, depending on the range of gradient strengths measured, in some experiments the data points for the first one or two gradient strengths are left out for the fit when the effect of SDS is visible.

For the evaluations of the ^{1}H measurements in the following sections, both peaks caused by hexadecane are used for the evaluation of the diffusion coefficient and the results are averaged, unless otherwise specified. Alternatively, ^{19}F NMR can be performed to measure the signal of SilF7, which is mixed with the hexadecane inside the core of the

particles. It is shown in the appendix A.3.2 that the diffusion coefficients of the particles in water observed by ^{1}H NMR are comparable to those obtained by ^{19}F NMR. The PFG NMR measurements were performed on a *Bruker AVANCE III 400 MHz* spectrometer using a wide-bore magnet. A DiffBB broad-band diffusion probe and a Great60 gradient amplifier from *Bruker BioSpin* were used to generate the magnetic field gradients of up to 17 T/m. The highest gradient was chosen dependent on the sample and its expected diffusion coefficient, combined with the diffusion time Δ and gradient duration δ_g. Unless otherwise specified, 32 signals for the ^{1}H and 64 signals for the ^{19}F measurements were added up for one experiment. Three experiments on the same sample were performed after each other and averaged. All measurements were performed at a temperature regulated to $(25 \pm 0.1)\,^{\circ}$C using a digital PID controller. A thermocouple below the sample was used to monitor the temperature. It was calibrated to ± 0.1 K with a high-precision platinum resistor.

A stimulated echo pulse sequence with spoiler gradients was used for all diffusion measurements. For the plots shown in figure 5.5 the measurements were performed at a diffusion time $\Delta = 23$ ms and effective gradient length $\delta_g = 4.1$ ms. The values used for other measurements were adjusted according to the sample and are mentioned in the respective sections.

5.2.5 Estimation of Shell Thickness

The volume of liquid inside the particles is of importance for the PFG NMR experiments, since it defines the number of 'NMR active' spins. However, it is not obvious to estimate the shell thickness of the individual particles. In the fabrication, the number of polymer molecules that later form the shell, are proportional to the volume of the individual particles, and therefore to the radius cubed. All these polymer molecules then move to the outside of the particle to generate the particle's shell, whose volume is in turn dependent on the outer particle radius and the concentration of polymer in the starting solution. It can be therefore assumed that the shell thickness is proportional to the (outer) radius of the particle.[165]

While this gives a hint on the relative shell thickness, the quantitative thickness, compared to the overall radius of the particle, cannot be determined exactly. However, the

intensity of NMR peaks in the ^{1}H NMR spectrum as shown in figure 5.4b can be compared to estimate this quantity. Knowing the concentration of a component visible in the NMR spectrum, the concentration of another component can be estimated by comparing the area under the corresponding peaks. The spectrum shown in figure 5.4b shows a sample that is diluted in 0.2 % SDS. While the peak at 1.7 ppm (peak 1) can be attributed to a -CH_2- group of SDS, containing two hydrogen atoms per SDS molecule, the peaks at 1.3 ppm (peak 2) and 0.9 ppm (peak 3) are caused by both SDS and hexadecane. Peak 2 is caused by a sum of 18 hydrogen atoms in a SDS and 28 in a hexadecane molecule, while peak 3 contains three protons of a SDS and six of a hexadecane molecule. The peak at 4.2 ppm, which can also be attributed to SDS, is left out of the calculation due to the baseline offset caused by the water peak.

Comparing the intensity of these peaks, a relative concentration of the hexadecane compared to the SDS can be calculated. It is supposed that the amount of SDS inside the particles is negligible. As the core of the particles is assumed to be completely filled by the oil, an absolute concentration of hexadecane can be calculated. The total volume of hexadecane can be devided by the concentration of particles as obtained from NTA to yield the inner radius, which can be calculated to be around (61 ± 6) nm. Comparing this to an outer radius of around 120 nm for the particles investigated in this experiment, this yields a particle shell thickness of around (59 ± 6) nm, which is around 50 % of the overall radius. Compared to the literature, this value is reasonable.[100] A detailed calculation of the value and the error are given in the appendix A.2.1. Since the shell thickness should be a relative measure compared to the particle size, the inner radius is assumed to be around half of the outer radius for different batches of particles.

5.2.6 Measurement Range for PFG NMR

When performing PFG NMR, a lot of parameters come into play that can be optimized for an accurate diffusion measurement of each sample. The maximum gradient strength $g_{\max}$, the diffusion time Δ, and the gradient duration δ_g play a role in the analyzed range of attenuation of the NMR signal as shown by equation (2.18). They should be chosen in a way that they allow for a reasonable range of the echo attenuation in order to be able to fit the attenuation using a maximum number of significant values. Preliminary experi-

ments on the system and a theoretical estimation of the expected diffusion coefficient are therefore helpful. The three discussed parameters are interdependent and should fulfill several properties to achieve optimal results as discussed in the following for the special case of liquid core particles.

First, the diffusion time Δ should be long enough that the particles cover a reasonable distance during this time. From equation (2.4), this can be estimated for a known diffusion coefficient. It can be assumed that the best results are obtained for covered distances larger than the particle diameter $\sqrt{\langle r^2 \rangle} > 2 \cdot R$, otherwise the displacement of the liquid molecules inside the particles contributes significantly the observed displacement. Assuming particles of radius $R \approx 100\,\mathrm{nm}$ diffusing freely in water, this leads to $\Delta \gtrsim 3\,\mathrm{ms}$ using equation (2.6). In principle, it should also be possible to measure a smaller MSD, for example for particles less mobile inside a complex medium. However, for the present case of liquid core particles, the diffusion of the liquid molecules hexadecane and SilF7 inside the particles comes into play. They are able to diffuse within the particle, and generate an (apparent) diffusion coefficient. The free diffusion coefficient of hexadecane is well tabulated.[248] The diffusion of free SilF7 in hexadecane has been measured using ^{19}F PFG NMR. Both components have diffusion coefficients for the free diffusion in hexadecane of around $3 \cdot 10^{-10}\,\mathrm{m^2/s}$. Even for a very short diffusion time of 1 ms, the mean covered distance of free hexadecane or SilF7 dissolved in hexadecane is in the range of $\sqrt{\langle r^2 \rangle} \approx 880\,\mathrm{nm}$. This means that the liquid molecules cover the whole interiour of the particles in the measurement time, which should generate a measurable mean covered distance in the range of 0.6 times the inner diameter of the particles as given in the literature[113,119], even if the particles themselves are immobile. It is therefore assumed that it is possible to measure small displacements of the particles, however, one needs to keep this effect in mind when discussing the resulting diffusion coefficients.

The diffusion time Δ and the gradient duration δ_g are further dependent on the relaxation times in the system. If the overall experiment time, represented approximately by the diffusion time, exceeds the longitudinal relaxation time T_1, most of the signal generated by the precessing nuclear spins will get lost. The same holds for the gradient duration and the transverse relaxation time T_2. Since the stimulated echo sequence is applied, spin-spin relaxation is only active in the time range around the gradient duration. To investigate the impact on the possible values of Δ and δ_g, the relaxation times in the given

liquid core particles system were examined as discussed in section 2.2.1. The particles were suspended in water. The longitudinal relaxation time was obtained from Inversion-Recovery experiments using equation (2.14). For the hexadecane signal, the T_1 relaxation time measured by ^{1}H NMR was around 800 ms, as obtained from five measurements. For the ^{19}F signal of SilF, the value was in the same range (720 ms), as measured twice. The effective transverse relaxation times T_2^* were obtained from an evaluation of the linewidth as given in equation (2.15). For ^{1}H NMR of hexadecane, a relaxation time in the range of 34 ms to 58 ms was calculated, while ^{19}F spectra yielded values of around 10 ms for SilF7, as taken from three spectra, each. The transverse relaxation time T_2 for hexadecane was measured three times by ^{1}H NMR using the Hahn echo following equation (2.16) and was determined to be around 50 ms. This is in the same range as the effective transverse relaxation time T_2^*. Since the Hahn echo experiments of SilF7 by ^{19}F did not give significant results, maybe due to a inadequate choice of the time scales in the performed experiments, the effective relaxation time is used here for an estimate of the limits of the experimentally useful time scales. Since the diffusion time should not exceed T_1, it can be concluded that $\Delta < 800$ ms, to avoid a significant signal loss due to longitudinal relaxation. Analogously, the gradient duration should be smaller than the lowest T_2 relaxation time, so that $\delta_g < 10$ ms. From the maximum diffusion time Δ we can further estimate that the lower limit of possible diffusion coefficients that can be measured in this system could in theory be on the order of $5 \cdot 10^{-15}$ m^2/s, which is in agreement with the literature.[122]

The gradient duration is limited to technical restrictions on the lower end, which leads to $\delta_g \gtrsim 1$ ms. Together with the maximum gradient strength, which can be adjusted in a range $0\,\mathrm{T/m} \leq g_{\max} \lesssim 17\,\mathrm{T/m}$ for the present PFG NMR setup, δ_g generates the phase shifts needed for the diffusion measurements. Both values together have to be adjusted to measure at suitable conditions for the expected diffusion coefficient. However, one has to take care that the gradient intensity, given by the gradient strength and the gradient length, is not too large compared to the diffusion of the spin-bearing molecules. If the molecules show a considerable displacement during the time the gradient is applied, the phase shift that a particle at a given location should obtain is no longer well-defined, but becomes blurred due to the motion of the particles.[113] Since the gradient intensity is adjusted to map the diffusion coefficient of the particles, which are much slower than the

liquid in their core, this puts a lower limit to the diffusion coefficient of the particles that can be measured. Assuming a gradient strength of $g = 17\,\mathrm{T/m}$ and a length of $\delta_\mathrm{g} = 5\,\mathrm{ms}$, which matches the measurements performed for the case of slowly diffusing particles in a hydrogel as shown in section 5.4, a simple geometric argument can be performed to estimate the distance that a particle has to cover during the gradient pulse to obtain a phase shift of 2π. This gives an order of magnitude estimate for the covered distance that would lead to a wrong labeling of the position by the gradient due to motional dephasing. In the present case this can be calculated to be 260 nm. Assuming an inner diameter of the particles of around 120 nm and a covered distance of the molecules within the particle of around $0.6 \cdot 120\,\mathrm{nm} = 72\,\mathrm{nm}$, it can be concluded that the measurements at these high gradients have to evaluated with care as there may be phase loss due to the diffusion of the molecules inside the liquid core during the time the gradient is applied.

5.3 Size Distribution Measurements by PFG NMR

Since the translational diffusion of a particle is directly related to its hydrodynamic radius according to equation (2.6), diffusion measurements on nanoparticles by PFG NMR can be used to measure particle size. In this context, it is useful to characterize the particles and their diffusion first in a simple aqueous environment. Further, a validation of the method via a direct comparison with other methods, such as DLS or NTA, becomes possible.

As described earlier, the hydrogen nuclear spins of the hexadecane in the core of the nanoparticles can be used as tracers to measure the diffusion of the whole particle using PFG NMR, which in turn relates to the particle size. However, as can be seen in the SEM image of the liquid core particles (figure 5.2), the particles are not monodisperse and should therefore show a distribution of sizes. Further, the core volume of the bigger nanoparticles is larger than for the smaller ones, which leads to a higher weighting of the bigger particles in the measured diffusion coefficient. These problems are not well accounted for by evaluating a single diffusion coefficient as described in section 5.2.4. The following section therefore outlines a method to obtain a particle size distribution from a PFG NMR measurement. In the following, the resulting PSD is compared with

size measurements using DLS and NTA to prove the reliablity of the size measurement by PFG NMR.

5.3.1 Obtaining a Number Distribution from PFG NMR

To evaluate the diffusion of polydisperse particles, the gamma distribution model of the diffusion coefficient $P(D;\kappa,\theta)$ can be applied as described in section 2.2.1. However, from this model, a volume weighted distribution of the nanoparticle diffusion coefficients is obtained since the signal intensity of each particle is dependent on the number of spins inside and hence on its inner volume. We therefore introduce a modified, number-weighted gamma distribution that compensates this volume effect, which is scaled by $r_0^3/r^3 \propto D^3/D_0^3$ as

$$\tilde{P}(D;\kappa,\theta) = P(D;\kappa,\theta) \cdot \frac{D^3}{D_0^3} = D^{\kappa-1}\frac{\exp(-D/\theta)}{\Gamma(\kappa)\theta^\kappa} \cdot \frac{D^3}{D_0^3} = \frac{D^{\kappa+2}}{D_0^3}\frac{\exp(-D/\theta)}{\Gamma(\kappa)\theta^\kappa}. \tag{5.1}$$

Here, $\Gamma(x)$ is the gamma function, and κ and θ are shape and scale parameters, respectively. The parameter $r_0 \propto 1/D_0$ is a reference radius. D_0 (or r_0 analogously) can be chosen to normalize the distribution so that

$$\int_0^\infty \tilde{P}(D)\mathrm{d}D = 1. \tag{5.2}$$

The signal attenuation of a PFG MR measurement including this distribution of diffusion then becomes

$$I(b) = I_0 \cdot \int_0^\infty \tilde{P}(D)\exp(-bD)\mathrm{d}D = I_0(1+b\theta)^{-\kappa}. \tag{5.3}$$

The calculation leading to this result is shown in the appendix A.2.2. By calculating the weighted mean of the obtained distribution $\tilde{P}(D;\kappa,\theta)$, we can get the number-weighted mean diffusion coefficient $\langle D\rangle$. The standard deviation σ_D is calculated by the square root of the second moment of the distribution. The results of measurements evaluated using this number-weighted gamma distribution fit are in the following always presented together with their standard deviation. Since the uncertainty from fitting errors is assumed to be smaller than the standard deviation (see section A.2.1 for details), it will

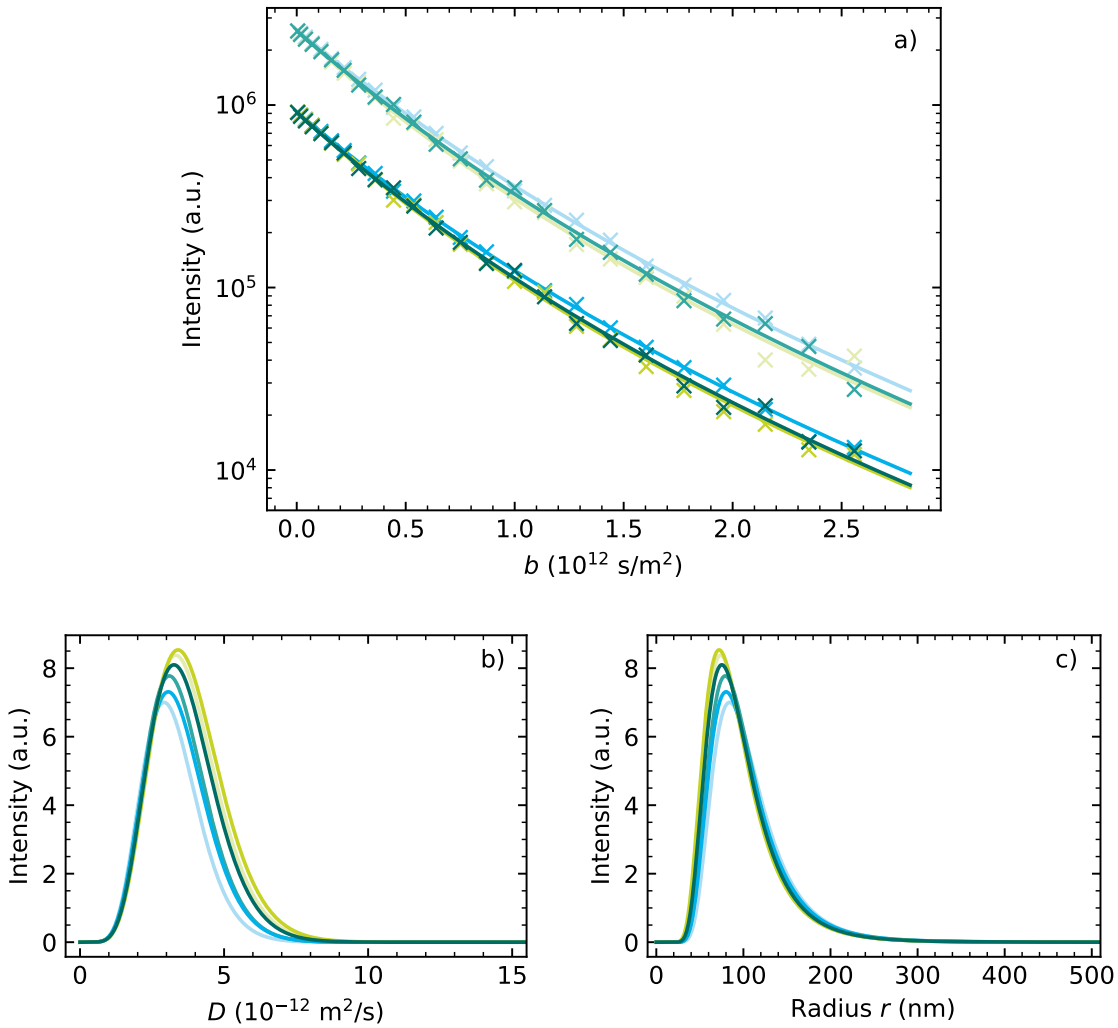

Figure 5.6: ^{1}H PFG NMR measurements on liquid core particles diluted in water showing the evaluation assuming a number-weighted gamma distribution of diffusion coefficients. The liquid core of the used particles contains hexadecane and SilF7. 32 scans were performed for each gradient strength, and the parameters $\Delta = 50\,\text{ms}$ and $\delta_g = 2.5\,\text{ms}$ were used. a) Intensity attenuation as obtained from the area under the two peaks assigned to hexadecane in the spectra recorded for different gradient strengths. The peaks at $\delta \approx 1.3\,\text{ppm}$ and $\delta \approx 0.9\,\text{ppm}$ were evaluated. Three measurements were performed. The fit follows the signal attenuation for a number distribution of diffusion coefficients as given in equation (5.3). b) From the fitting parameters, the number distribution of diffusion coefficients can be calculated following equation (5.1). The obtained averaged mean diffusion coefficient is $\langle D \rangle = 3.55 \cdot 10^{-12}\,\text{m}^2/\text{s}$ and the corresponding standard deviation is $\sigma_D = 1.15 \cdot 10^{-12}\,\text{m}^2/\text{s}$. c) Analogously, the number PSD is obtained from the fitting parameters as given in equation (5.4), showing an averaged mean radius $\langle D \rangle = 101\,\text{nm}$ and its standard deviation $\sigma_r = 43\,\text{nm}$.

be left out to improve readability. Also, from converting the distribution of diffusion coefficients to a distribution of radii $\tilde{P}(r;\kappa,\theta)$ using the SES equation (2.6) as

$$\tilde{P}(r;\kappa,\theta) = \frac{(\alpha/r)^{\kappa+2}}{(\alpha/r_0)^3}\frac{\exp(-\alpha/(r\cdot\theta))}{\Gamma(\kappa)\theta^\kappa}, \quad \alpha = \frac{k_\mathrm{B}T}{6\pi\eta}, \tag{5.4}$$

the mean particle radius $\langle r\rangle$ and its standard deviation σ_r can be calculated in the same way as for the distribution of the diffusion coefficients.

Figure 5.6 shows the results of ^{1}H PFG NMR measurements of liquid core particles in water. They are measured using a diffusion time $\Delta = 50\,\mathrm{ms}$, gradient length $\delta_\mathrm{g} = 2.5\,\mathrm{ms}$, and performing 32 scans. In figure 5.6a, the intensity of the two peaks belonging to hexadecane ($\delta \approx 1.3\,\mathrm{ppm}$ and $\delta \approx 0.9\,\mathrm{ppm}$) is plotted with respect to the parameter b, representing the gradient strength squared. Since the particle stock solution, which contains remaining SDS from the fabrication process, is diluted in water, the intensity of the signal by SDS is reduced compared to figure 5.5. Note the logscale on the y axis, which represents an exponential decay as a linear slope. The curve of the measured values does not follow an exponential decay as given in equation (2.17), which would be the case for a diffusing species that has only one size. Instead, the curve is slightly bent, indicating the presence of differently sized diffusing species. A fit following equation (5.3) is therefore used to calculate a distribution of diffusion coefficients. The resulting plot that shows the number of particles over their diffusion coefficient, as calculated from the fitting parameters following equation (5.1), is shown in figure 5.6b. This result can be further transferred into a PSD plot, which is shown in figure 5.6c. To validate the results obtained by this method, the PSD is in the following compared to the distribution obtained by DLS and NTA.

5.3.2 Comparison with DLS and NTA

To assess the validity of the PSD obtained by fitting the PFG NMR results using a number-weighted gamma distribution of the diffusion coefficients, particles from the same batch were measured with DLS and NTA. Details about the DLS and NTA measurements are given in section 5.2.2. It has to be mentioned that the particle concentrations used in DLS and NTA are smaller than for PFG NMR, which is due to the restrictions of the different methods. However, as explained in section 5.2.2, all concentrations are

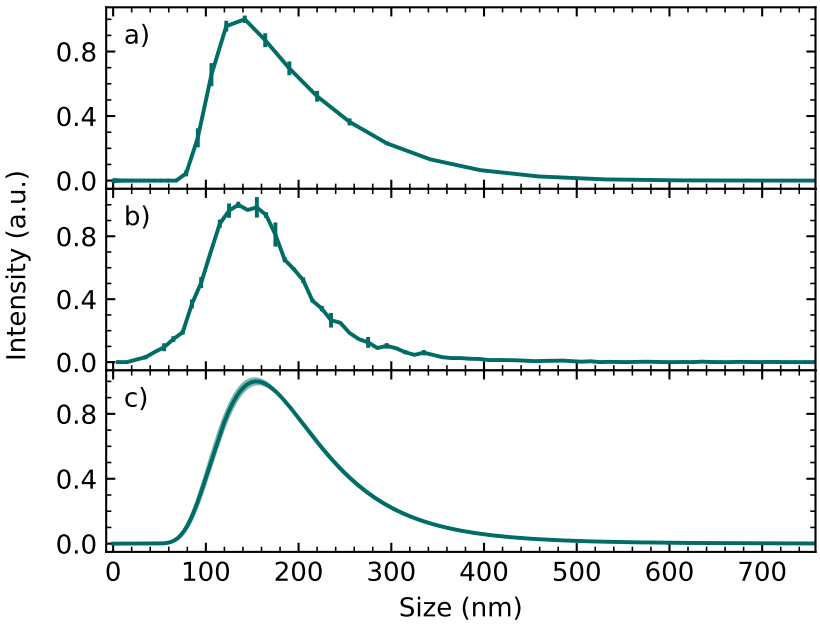

Figure 5.7: Comparison of different methods for size measurement to validate the evaluation of PFG NMR results using the number-weighted gamma distribution model. The liquid core particles containing hexadecane and SilF7 were diluted in water. a) Averaged results of ten DLS measurements as shown in figure 5.3a. b) PSD obtained by NTA, averaged over two measurements. The individual measurements are shown in figure 5.3b. c) ^{1}H PFG NMR results, averaged over the three measurements with two peaks, each. Original data was shown in figure 5.6c and is adjusted here to show the diameter instead of the radius. The error bars or shaded area in the plots represent the standard error of the mean for each bin or size value in analogy to equation (A.5).

small enough that the effect of particle collisions is negligible. The methods are therefore assumed to be comparable.

The resulting PSD plots with respect to the particle size (diameter) are shown in figure 5.7. The three curves show slight differences in their shape, which is assumed to be caused by the different methods of measuring. In principle, however, their position is very similar and the peaks are strongly aligned. It has to be noted that the curves obtained by DLS and PFG NMR are very smooth compared to the NTA curve. This is due to the difference in the method of measuring. In contrast to NTA, where an evaluation of individual particles is performed, the particles in the sample are measured as an ensemble, which causes the smooth (artificial) curve of the size distribution.

This evaluation shows that the fitting method using a number-weighted gamma distribution of the diffusion coefficients on the PFG NMR measurements as outlined above gives

reliable results and can be used to obtain a PSD by evaluating the NMR signal of the nuclear spins.

5.4 Diffusion Measurements by PFG NMR in Complex Systems

While the measurements discussed in section 5.3 are performed in water with the purpose of determining the dimensions of the used particles, the power of PFG NMR measurements is that they also allow one to draw conclusions about the surrounding medium by using the particles as diffusion nanosensors. Now that the particle size and their diffusive behaviour in water have been determined, they can be used to probe other liquid-like complex media. In a first step, isotropic glycerol solutions with varying viscosity are examined.

5.4.1 Diffusion in Media of Different Viscosity

According to the SES equation (2.6), the diffusion coefficient of a diffusing species is inversely proportional to the viscosity of the surrounding medium. If temperature and particle size are well-known, it is possible to determine the viscosity of the medium using the diffusion coefficient obtained by PFG NMR. To test this, the diffusion of the liquid core particles is measured in aqueous glycerol solutions of different concentrations. The higher the concentration of glycerol, the higher is the viscosity. This system is well tabulated and can therefore serve as a model system to test if the measurements are reliable.[249] Glycerol is a molecule that is miscible with water due to its three hydroxyl groups. In ^{1}H NMR it shows peaks at chemical shifts in the range of $\delta \approx 3.3\,\text{ppm}$ to $\delta \approx 3.8\,\text{ppm}$ and at $\delta \approx 5.2\,\text{ppm}$ as shown in figure 5.8a.[250,251] There is no peak of the glycerol overlapping with the hexadecane peaks of the oil enclosed in the particle shell. The PFG NMR measurements on the particles in aqueous solutions of glycerol can therefore be performed by ^{1}H NMR, using the characteristic peaks of hexadecane.

The glycerol solutions are assumed to be homogeneous and isotropic on the covered length scales. Therefore the diffusion should not be dependent on the diffusion time (different to the case of diffusion in a more complex medium as discussed in the following section).

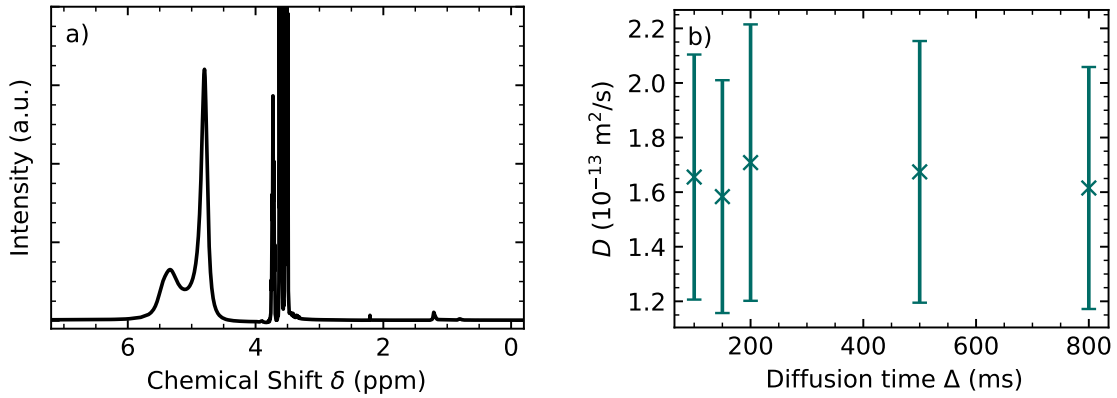

Figure 5.8: ^{1}H NMR spectrum of liquid core particles containing hexadecane and SilF7 suspended in an aqueous 60 % v/v glycerol solution. The peaks in the range of $\delta \approx 3.3$ ppm to $\delta \approx 3.5$ ppm and at $\delta \approx 4.5$ ppm are assigned to the glycerol. Since there are no peaks overlapping with the hexadecane peaks, these are evaluated in the PFG NMR experiments to measure the diffusion of the nanoparticles. b) The diffusion coefficients of the particles were measured for different values of the diffusion time Δ. Three measurements were performed for each diffusion time performing 32 scans at $\delta_g = 5$ ms. The intensity attenuation was evaluated using the number-weighted gamma distribution model given in equation (5.3). The resulting mean diffusion coefficients and their standard deviations were averaged and shown in the plot. The error bars represent the standard deviation of the distribution of diffusion coefficients.

To prove this, the diffusion coefficients of the particles in a 60 % v/v aqueous glycerol solution were investigated for different diffusion times. In the following, all glycerol samples are given in volume percent. Three measurements were performed for each sample using $\delta_g = 5$ ms and performing 32 scans. A fit following the number-weighted gamma distribution of diffusion coefficients as presented in section 5.3.1 was applied for each individual measurement. The results are listed in table A.5 and shown in figure 5.8b. For the measurements at $\Delta = 100$ ms, the last six gradient values were left out due to dephasing problems. Because the gamma distribution model is more delicate than just fitting an exponential decay, the fits of single measurements did not converge and are therefore not part of the average values shown here. Nevertheless, each average is calculated from at least three fits. Fits using the exponential decay (equation (2.17)) show comparable values for the measurements where the more complex fit did not converge to the ones where the gamma distribution fit converged. They are therefore assumed to be consistent with all measurements and the small differences in the respective fits are expected not to alter the results significantly.

As can be seen in figure 5.8b, the mean diffusion coefficient does not change with the increasing diffusion time. In the glycerol solutions, there is no spatial inhomogeneity on the length scale that the particles are covering in the given diffusion times, which range from $\sqrt{\langle r^2 \rangle} = 315\,\mathrm{nm}$ for $\Delta = 100\,\mathrm{ms}$ to 880 nm for $\Delta = 800\,\mathrm{ms}$. Glycerol solution can therefore be assumed to be isotropic and homgeneous on the probed length scale, and the diffusion of the particles is independent of the diffusion time.

It has further been tested to measure the diffusion coefficient in the given sample for even shorter diffusion times between 11.93 ms and 50 ms using the same gradient length $\delta_\mathrm{g} = 5\,\mathrm{ms}$ than for the just discussed measurements. To compensate for the shorter diffusion time, but still be able to cover a significant range of b values, the gradient strength had to be increased up to around $g = 17\,\mathrm{T/m}$ for these measurements. It has to be noted that these are conditions, as discussed in section 5.2.6, where the impact of a high gradient intensity on the liquid core particles has to be considered. As is also discussed in section A.3.3, the signal interpretation is complicated for large gradients. For the regime of high gradient intensity, given by the gradient length and strength, the critical distance that the spin-bearing liquid molecules must not cover within the gradient time is on the order of magnitude of 200 nm. For the present case of particles in a 60 % glycerol solution, the mean covered distances of the molecules in the core is given by the movement inside the particle core and the movement of the particle, which is very close to the mentioned critical regime. Indeed it can be observed for the measurements at short diffusion times and high gradient strengths that the signal attenuation near this limit shows an unphysical behaviour for the higher gradients. After a slow attenuation for the first data points, the decay for the higher gradients is steeper, which cannot be explained by another diffusive species and leads to an overestimation of the diffusion coefficient. It is therefore assumed that we are reaching the lower limit of the method concerning the detectable diffusion at high gradient intensity with the 200 nm liquid core particles. Additional effects that could cause this unphysical behaviour of the echo attenuation are carefully examined and discussed in section A.3.3. The aforementioned effect of dephasing due to a high gradient intensity is found to be the most likely artifact, but also diffusive diffraction could play a role in explaining the observed effects.

In a next step, the diffusion coefficient of the particles in aqueous solutions of different volume concentrations of glycerol is investigated. This is done using ^{1}H PFG NMR with

a diffusion time $\Delta = 100\,\text{ms}$, gradient length $\delta_g = 5\,\text{ms}$. Three experiments of 32 scans each were performed. Since the diffusion coefficient is not dependent on the diffusion time as shown above, higher diffusion times of 150 ms and 500 ms were chosen for the solutions of 60 % and 80 % glycerol to be able to reach higher values of b. This is needed to compensate for the slower diffusion in the media of higher viscosity. Figure 5.9a shows exemplary intensity attenuation plots for the different concentrations of glycerol as evaluated for the peak at $\delta \approx 1.3\,\text{ppm}$. It has to be noted that only a section of the whole plot is shown for better visibiliy of the curves' slopes. For the two higher glycerol concentrations, some gradient values are not shown, but are nevertheless part of the evaluation. A plot with all data points is shown in figure A.2a.

It is clearly seen that the slope decreases with increasing viscosity (i.e. with increasing concentration of glycerol), indicating a slower diffusion in more viscous media. The fits follow the number-weighted gamma distribution model as given in section 5.3.1 and yield diffusion coefficients and standard distributions as listed in table A.5. These values are shown in figure 5.9b with respect to the concentration of glycerol. The error bars represent the standard deviation obtained by the gamma distribution model. It has to be noted that for the 20 % glycerol sample, the fit did not converge for two values (out of six) which are therefore not included. However, fitting an exponential decay following equation (2.17) shows that the obtained values of the diffusion coefficient for these points are fully consistent with the other data points.

Knowing the PSD of the used particles, the diffusion coefficient can be utilized to estimate the viscosity. Here, this is done by varying the value of η in the calculation of the PSD in the presence of glycerol and searching for the lowest difference to the PSD in water. The RMS for the difference of the two curves is calculated and minimized to obtain the closest fit. The known value of the viscosity in pure water is thereby taken as a reference. The obtained values are given in table 5.1 and compared to the literature values.[249] Although the values do not completely match, the trend is clear and the experimentally obtained values are comparable to the literature. The inverse of the literature values of the viscosity of aqueous glycerol solutions are also shown in Fig 5.9b as a guide to the eye. The two axes are not correlated. However, it can again be seen that the PFG NMR measurements follow the trend of the viscosity clearly.

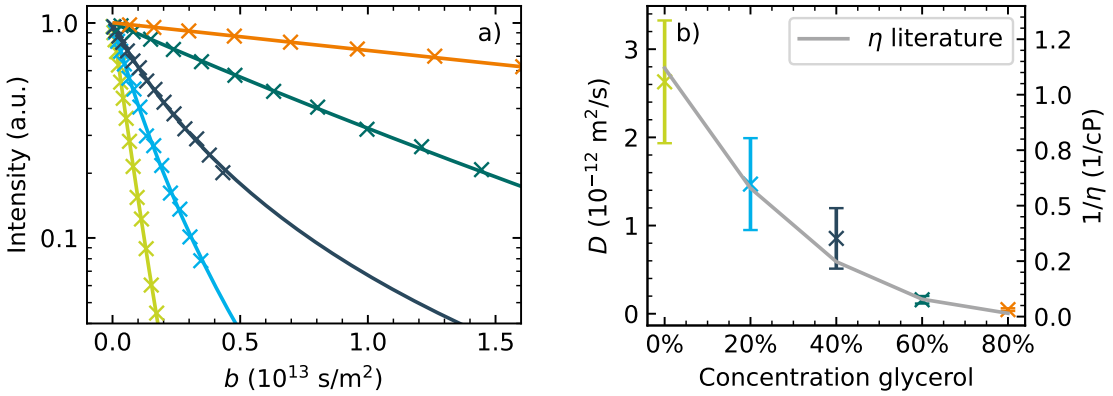

Figure 5.9: Results of ^{1}H PFG NMR measurements of liquid core particles in glycerol solutions of different concentrations. The particle core consists of hexadecane and SilF7. Three PFG NMR measurements were performed for each sample and evaluated individually to obtain the mean diffusion coefficient and its standard deviation from the fit assuming a number-weighted gamma distribution of diffusion coefficients following equation (5.3). Parameters of $\Delta = 100\,\text{ms}$ and $\delta_g = 5\,\text{ms}$ were used, and 32 scans were recorded. For the samples in 60 % and 80 % glycerol, the diffusion times were increased to 150 ms and 500 ms to compensate for the higher viscosity. a) Exemplary intensity attenuation plots for different concentrations of glycerol. The colour coding is given the second plot. A plot showing all measurement points is given in figure A.2a. b) Averaged mean diffusion coefficients obtained from the fit on the intensity attenuation for samples of different concentration of glycerol. It has to be noted, that this refers to a volume concentration. The error bars show the averaged standard deviation of the distribution. The viscosity of aqueous solutions of glycerol is well tabulated[249] and the inverse is shown in gray as a guide to the eye. It has to be noted that the two y axes are not correlated.

The presented results show that PFG NMR on the liquid core particles can be performed in a range of viscosities that cover nearly two orders of magnitude. Knowing the particle size and the temperature, the viscosity of the liquid can be determined. While this is easy to do for isotropic systems, the case of diffusion in complex media becomes much more complicated and will be discussed in the following.

5.4.2 Diffusion in Hydrogels

As was shown in the last section, the diffusion coefficient of particles diffusing in isotropic media is independent from the diffusion time. In a complex medium like a hydrogel, this can be expected to be no longer valid. Instead, the diffusion will now appear to be time-dependent as described in section 2.1.2. It is assumed that conclusions on the

Table 5.1: Comparison of the viscosity of aqueous glycerol solutions of different concentrations. The literature values for the given temperature of 25 °C are calculated following N. Cheng[249]. The measured viscosity is calculated from the results of the PFG NMR measurements of the liquid core particles in the glycerol solutions as outlined in the text. The viscosity in water is thereby taken as a reference and hence not listed in the table.

c_{glyc}	η_{lit} (mPas)	η_{meas} (mPas)
0 %	0.89	
20 %	1.73	2.0479
40 %	4.04	3.346
60 %	12.74	16.991
80 %	66.56	55.048

microstructure of the surrounding mesh can be drawn by evaluating the behaviour of the diffusion nanosensors.

Out of the large pool of hydrogels, we decided to test our diffusion method on methacrylated hyaluronic acid (HAMA) gel. My colleague Dr. Dimitris Missirlis functionalized the polymers following the protocol outlined in section A.1.3. Hyaluronic acid is a polymer naturally occuring in our body.[252] The polymers can be chemically adjusted to obtain partly synthetic HA methacrylate (HAMA) polymers, that can be covalently crosslinked by photopolymerization.[252–255] HAMA gels, also called MHA, or MeHA in the literature, are widely used in biomedical applications due to their good biocompatibility, the fast synthesis, and the possibility of inducing the crosslinking process by a photoinitiator.[253] They have broad application in tissue engineering[252,253,256–260], drug delivery[252,261] , or cell encapsulation[260,262–265].

Since HAMA gels have widespread applications, their microstructure is of interest. However, determining the mesh size of the hydrogel structure is challenging. To the best of my knowledge, only two methods can be found in the literature when searching for the microstructure of HAMA gels. Estimating the pore size from SEM images is a commonly used technique for hydrogels.[236,237] Pore sizes in a broad range between around 24 µm and 600 µm, in individual studies up to nearly 1 mm, are reported in the literature for pure HAMA gels[265–269], which is comparable to values that can be found for modified HAMA gels or composite gels, that contain HAMA besides others.[270–276] To be able to perform SEM, the samples need to be dehydrated. It can therefore be assumed that the values, although obtained from good quality images, are not reliable. A second method

for mesh size estimation is based on evaluation of the swelling. From the amount of water that is uptaken by the hydrogel compared to the dry mass the average molecular weight between two cross-links is calculated. The mesh size is then estimated using a model that includes the interaction between solvent and polymer. Mesh sizes between around 540 nm and 1.2 µm are reported for different concentrations of polmer and different magnitudes of methacrylation, while another study obtains mesh sizes between 20 nm and 60 nm. As is pointed out in the literature, swelling assessment is just a model and includes assumptions that have to be made. The obtained mesh sizes should hence be understood as an estimate of their order of magnitude.[238,239,277] The literature is therefore indicating a mesh size that is probably in the range of some tens of nanometers up to a few microns. Further, individual studies of diffusion measurements of nanoparticles in HAMA gels have appeared, though none of them is used to estimate the mesh size.[254,278,279]

The motivation of the present work is that the apparent diffusion coefficients of liquid core particles, if interpreted correctly, can give valuable information about the mesh size in a hydrated state of hydrogels and HAMA gels in particular. This will be investigated in the following. It has to be noted that the terms 'pore size' and 'mesh size' seem to be often used interchangeably in the literature, especially for the case of nanoparticle diffusion in complex structures like hydrogels.[57,59,69–72,75,76,79–81,84,85,88–90,95,280–286] As we are probing short length scales by the method of PFG NMR, it appears that using the term 'mesh size' is more appropriate for the following discussion.

To investigate the diffusion of nanoparticles in HAMA gels and estimate the mesh size of the gel, the (apparent) diffusion of liquid core particles was measured by PFG NMR for different diffusion times. The size of the particles was determined beforehand and found to be $R \approx 120\,\text{nm}$ by performing PFG NMR on the particles in water and using the number-weighted gamma distribution model to yield a number distribution as discussed in section 5.3.1. The HAMA samples used in this section were prepared by mixing HAMA polymer, particles, water, and the photoinitiator LAP to obtain samples of HAMA gel containing $5 \cdot 10^{11}$ particles/ml of the liquid core particles. A 4 % stock solution of HAMA was used and diluted using the other components to obtain final concentrations of 0.8 %, 1.0 %, and 1.2 % HAMA gels. The purity of the polymer stock solution will influence the final concentrations, however this can be estimated to have a minor effect as briefly outlined in section A.1.3. The photoinitiator was always added in the same amount to

reach a concentration of 2.5 mg/ml. After adding the photoinitiator, the samples were illuminated by UV light at 405 nm for around 1 min. The PFG NMR measurements were performed using ^{19}F PFG NMR to measure the signal of SilF7. 64 scans were performed for each measurement. A gradient length of $\delta_g = 5$ ms was used. For each diffusion time, two measurements (three for the diffusion time of 500 ms) were performed, evaluated, and averaged. An exemplary plot of the intensity attenuation is shown in figure A.2. The ^{19}F spectra recorded in the PFG NMR experiments show a low S/N ratio, presumably due to the long gradient duration and the short T_2 and T_2^* relaxation times (discussed in section 5.2.6), as well as the lower concentration of SilF7 compared to hexadecane. Due to the low S/N, the intensity attenuation plot with respect to parameter b is fitted with a single exponential decay, following equation (2.19). The resulting values are listed in table A.4. It has to be noted that this evaluation is different from the last sections, where a gamma distributed diffusion coefficient was assumed instead of a single value of D. This leads to smaller error bars compared to the plots shown before, since they represent only the fit error as outlined in section A.2.1, and not the standard deviation, as used above.

The resulting apparent diffusion coefficients with respect to the diffusion time are shown in figure 5.10a. Different to figure 5.8b, where an independence of the diffusion coefficient from the diffusion time was observed for glycerol, a decay of the apparent diffusion coefficient with increasing diffusion time can be observed. This is a typical behaviour of diffusing species in confined environment as discussed in section 2.1.2. The mean covered distance for each diffusion time can be calculated from the measured apparent diffusion coefficients using equation (2.4). The obtained mean covered distances are in a range of $\sqrt{\langle r^2 \rangle} = 109$ nm (for $\Delta = 500$ ms and 800 ms), increasing as the diffusion time reduces to 188 nm (for $\Delta = 20$ ms). The calculated values of the MSD, that do not show an increase with the diffusion time, give rise to the assumption, that the particles are not moving freely, but are trapped inside the hydrogel mesh. It is assumed that the particles are allowed to diffuse inside a void of the mesh in a small free volume, but are not able to move to another void as it is assumed in some hydrodynamic models.[69–74] It is important to mention that the particles were measured to show a negative zeta potential (measured using a *Malvern Zetasizer Nano Z*), which is the same polarity as the negatively charged HAMA polymers.[253,279,287,288] It can therefore be assumed that

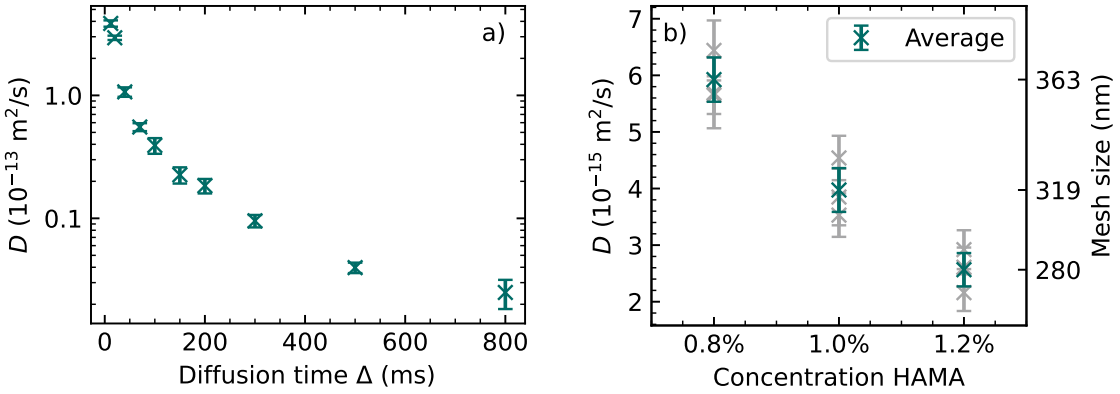

Figure 5.10: ^{19}F PFG NMR measurements on liquid core particles in HAMA hydrogels. The signal of SilF7 in the core is used for the measurement and evaluation. 64 scans were performed for each measurement using $\delta_g = 5\,\text{ms}$. The intensity attenuation was fitted using an exponential decay following equation (2.17). An exemplary plot of the intensity attenuation is shown in figure A.2b. The mean value of D and its uncertainty ΔD are evaluated as outlined in section A.2.1. The error bars represent this uncertainty. The values shown in both plots are listed in table A.4. It has to be noted that the apparent diffusion coefficient may be slightly overestimated due to possible artifacts in the PFG NMR measurements as described in the text. a) Apparent diffusion coefficients in 1 % HAMA gel for different diffusion times Δ. Two measurements were performed for each diffusion time, except for 500 ms, where three measurements were done. The diffusion coefficient in water, measured by ^1H PFG NMR and evaluated using an exponential decay is $(1.92 \pm 0.03) \cdot 10^{-12}\,\text{m}^2/\text{s}$. b) Apparent diffusion coefficients of HAMA gels for different polymer concentrations. The measurements were performed at $\Delta = 500\,\text{ms}$ to ensure that the long-term diffusion is measured. Three measurements were performed and averaged. The results of the individual measurements are shown in gray. The estimated mesh size of the hydrogel as calculated by equation (2.7) is indicated on the right y axis.

the particles are not electrostatically attracted by the polymers, but rather experience a repulsive interaction. However, the decrease of the mean covered distance with increasing diffusion time is unphysical and careful analysis of possible artifacts has to be performed. This is done in detail and with consideration of the effects observed for the glycerol measurements at small diffusion times in section A.3.3. Two effects are considered that could cause a loss of the phases coherence in an NMR signal, namely a dephasing due to non-negligible diffusion during a high intensity gradient pulse, or diffusive diffraction of the liquid molecules inside the particle. Both effects are assumed to generate an overestimation of the apparent diffusion coefficient, if they are playing a role in the HAMA measurements. The measurements shown in figure 5.10 should therefore be interpreted with care and the reader has to keep in mind that the diffusion coefficients could be overestimated. For the case of dephasing due to high intensity gradient pulses, it can be assumed that the effect increases for smaller diffusion times, as can be seen for the glycerol measurements discussed in section A.3.3. Nevertheless, the overall trend of the decreasing apparent diffusion coefficients gives rise to the interpretation, that the particles are not freely diffusing, but trapped inside the hydrogel mesh.

Since the particles seem to be trapped in voids in the mesh, the mesh size of the HAMA hydrogel can be estimated by modeling the voids to have a spherical shape in analogy to what is found in the literature.[113,120–122] The mesh size can then be estimated using equation (2.7), which is valid for long-term diffusion coefficients and the condition of small q values. To fulfill the first requirement, only the apparent diffusion coefficients obtained at $\Delta \geq 500\,\mathrm{ms}$ were taken into account for the calculation. The used q value, defined by $q = \gamma \delta_\mathrm{g} g$, is estimated to fulfill the small q limit condition.[113] A discussion can be found in the context of diffusive diffraction in section A.3.3. In our special case, the MSD is determined only from the diffusion of the liquid core, which cannot sample the whole volume of the mesh void due to the particle shell acting as a spacer. It is therefore assumed that the mesh size obtained by this model underestimates the real mesh size by the thickness of the particle shell of around 60 nm on both sides. Taking these considerations into account, the mesh size obtained by this model is

$$\xi = 2 \cdot a + 2 \cdot R_\mathrm{shell} = 2 \cdot \sqrt{5 \Delta D} + 2 \cdot 60\,\mathrm{nm} \approx 319\,\mathrm{nm}, \tag{5.5}$$

which lies in between the values given in the literature. To estimate the uncertainty of the evaluated mesh size, error propagation is performed using the standard deviation of the diffusion coefficient and the particle radius, and the uncertainty of the core radius as obtained in section 5.2.5. A detailed calculation is shown in the appendix A.2.1. The resulting uncertainty of the mesh size is $\Delta\xi = 70\,\mathrm{nm}$, which is mostly caused by the particle size distribution. However, when estimating this mesh size, it has to be noted that the apparent diffusion coefficient could be overestimated due to the discussed artifacts. The obtained mesh size is therefore considered as an upper limit, so that the estimated mesh size can be written to be $\xi \leq (319 \pm 70)\,\mathrm{nm}$.

The mesh size obtained by equation (5.5) can further be supported by a simple geometric consideration. Comparing the measured apparent diffusion coefficients in the presence of a HAMA gel with that in water ($D_0 = (1.92 \pm 0.03) \cdot 10^{-12}\,\mathrm{m^2/s}$), as evaluated using an exponential decay fit, shows that even the smallest investigated diffusion time of 11.93 ms leads to a notable slowdown of the particles by around one order of magnitude. If the particles diffuse freely in water, they would cover a mean distance of $\sqrt{\langle r^2 \rangle} \approx 371\,\mathrm{nm}$ in 11.93 ms according to equation (2.4). They cannot move across this distance without (at least some of them) noticing the presence of the gel network. It can therefore be assumed that the mean mesh size is less or not notably larger than 371 nm. The calculated value of $\xi \leq (319 \pm 70)\,\mathrm{nm}$ agrees with this limit and can therefore be assumed to be a reasonable estimate for the given system.

While the reader has to keep in mind that the used models and estimations simplify the structure of the hydrogel mesh to spherical voids in the gel mesh, the presented results are nevertheless assumed to give good estimates for the maximum average mesh size. Diffusion measurements of liquid core particles by PFG NMR have therefore been shown to yield valuable information of the microstructure of HAMA gels. For the specific 1 % HAMA gel, an average mesh size of around 320 nm was obtained, which is on the same order of magnitude than values given in the literature as obtained by a swelling assessment.[238,239,277] However, for the present system of the 200 nm sized particles in a HAMA gel, we are presumably reaching the lower limit of this method due to the size of the liquid core particles.

Since the concentration of polymer, besides others, can alter the microstructure of a hydrogel, we finally investigated the diffusion of our particles in HAMA gels of 0.8 % and 1.2 % HAMA polymer content. The samples were prepared as described above. The PFG NMR measurements were performed at diffusion times of 500 ms, to make sure that the long-term diffusion is observed. 64 scans per measurement were performed for $\delta_g = 5$ ms. Three measurements were performed and averaged for both samples, together with the 1 % HAMA sample. The resulting apparent diffusion coefficients are shown in figure 5.10b. A decay in the apparent diffusion coefficients with increasing polymer concentration can be observed. An increasing polymer concentration is expected to yield a smaller mesh size of the hydrogel, causing the particles to be less mobile within the hydrogel. This agrees well with the observed behaviour of the apparent diffusion coefficient. The mesh sizes are estimated using equation (2.7) and indicated on the right-hand y axis. Error propagation gives uncertainties of around 70 nm for all three mesh sizes, which are not included in the plot to maintain a clear presentation. Again, it has to be noted that the diffusion measurements performed here seem to be at the lower limit of the method and could therefore be subject to artifacts. As discussed before, this could create an overestimation of the measured diffusion coefficients. There is no indication that the measurements in the three gel concentrations could be affected by possible artifacts in a different way. It can therefore be assumed that the apparent diffusion coefficients, although possibly overestimated, show a clear trend to slower diffusion when increasing the hydrogel concentration. This is particularly useful for the investigation of diffusion mechanisms of nanoparticles in hydrogels.

5.5 Summary and Outlook

Nanoparticles can be used as diffusion nanosensors to draw conclusions about the microstructure of fluid-like media as well as about possible interactions of the particles with the medium. To be independent from optical properties of the used particles and their environment, PFG NMR can be used as a direct, non-invasive, and model-free method to measure diffusion coefficients of 'NMR active' nuclear spins in bulk and without the need for a fluorescent label. By fabricating oil-filled core-shell particles, the liquid core

trapped inside the particle shell provides nuclear spins and a sharp NMR peak that can be investigated by PFG NMR.

It has been demonstrated that the hexadecane/SilF7 liquid core gives characteristic signals in both ^{1}H and ^{19}F NMR spectra. Both molecules can be used to measure diffusion of the particles since their location is restricted to the inside of the particle shell. The successful particle fabrication was not only confirmed by SEM, but also by measuring the PSD of the particles in water by optical methods, namely DLS and NTA. A method to evaluate a number PSD using PFG NMR is presented and shown to give particle sizes comparable to the other methods. The particles have been successfully tested to survive in an environment of higher viscosity and complexity. In aqueous glycerol solutions of different viscosity, the diffusion coefficients have been observed to mirror the known viscosity of the surrounding medium. When introduced in a HAMA gel, which shows a more complex ^{1}H NMR spectrum, the fluorinated component SilF7 can be used for the diffusion measurements. It has been observed that the apparent diffusion coefficient of the particles becomes time dependent in the complex environment of the hydrogel. This is an indication for a tightly packed hydrogel mesh, that effectively hinders particle diffusion. The method has been tested in HAMA gels of different concentration and shows a decreasing apparent diffusion coefficient with increasing concentration of polymer, which mirrors a decreasing mesh size of the hydrogel.

While the given system of around 200 nm particles in a HAMA hydrogel has been shown to allow for an investigation of the diffusive behaviour of the nanoparticles, it was observed that this system is reaching the limit of the analyzable diffusion coefficients where the mesh size is small. The combination of fast diffusion of the liquid core molecules combined with the slow diffusion of the whole particle creates a complex system, that has to be carefully analyzed. While free particle diffusion in water or aqueous glycerol solutions allows for measurements at high diffusion times and low and/or short gradient pulses, the gradient strength and pulse length have to be increased when slower diffusion is to be measured. While for the measurement of simpler systems like freely diffusing molecules, it should be possible to measure diffusion coefficients down to the range of $5 \cdot 10^{-15}\,m^2/s$ by application of high and long gradients[122], the measurement of liquid core particles is restricted by dephasing effects of the liquid molecules during the gradient pulse or by diffusive diffraction. The lowest diffusion coefficient measured in this thesis

that is assumed to be free of artifacts is on the order of $1 \cdot 10^{-13}\,\mathrm{m}^2/\mathrm{s}$. Therefore the quantification of apparent diffusion coefficients inside the HAMA gel samples is assumed to be at the lower limit of the method or below, which could lead to artifacts in the measurement resulting in an overestimation of the diffusion coefficient. Nevertheless, the measurements presented in this chapter show that the system of liquid core particles measured by PFG NMR can serve as a tool to estimate diffusion mechanisms of nanoparticles in complex environments that are larger than conventional PFG NMR probes. For hydrogels with a mesh size in a range of some hundreds of nanometers to a few microns, the presented 200 nm particles are assumed to be perfectly suited. However, if the size of the nanoparticles is reduced, even smaller mesh size may also be probed. If, for example, the particle sizes were further reduced to 100 nm, the diffusion increases by a factor of two and the effect of dephasing of the liquid molecules in the core would be reduced due to smaller covered length scales of the molecules inside the core. In addition, smaller gradients could be used and possible effects of diffusive diffraction would be reduced. On the other hand, a higher particle concentration would be required due to the smaller inner volume.

Hence, the method holds a great potential in characterizing media like biologically relevant hydrogels or real tissue and investigating diffusion mechanisms of different nanoparticles inside such media. While other methods suffer from a limited optical penetration depth in opaque or complex media, and might require fluorescent particle labeling, diffusion measurements by PFG NMR offer a non-invasive, direct, and label-free method to draw conclusions on the sub-micron structure of complex or opaque media, independently from the optical properties of the nanoparticles and the medium.[86,87,119,123] Changing the particle size by modifying the fabrication protocol, or varying their surface chemistry using the layer-by-layer technique[289–291] may give rise to a broad spectrum of systems suitable for investigation of diffusive properties inside a given medium.

6 Conclusions and Outlook

Different methods of diffusion measurements in biologically relevant systems are examined in this thesis. DNA origami is presented to serve as a precise and well-defined probe for diffusion mesurements, which can be performed fast and sensitively down to picomolar concentrations using NTA-FL. DNA origami benefits not only from a highly uniform size and shape, but also from the possibility of specific binding to an analyte DNA. It is shown that this can be used to detect the presence of characteristic DNA biomarkers in a suspension, which is of interest in medical diagnostics of infections and diseases. The DNA nanosensors can be carefully designed to bind the analyte strand, leading to a connection of two origami structures via the analyte. This causes an increase in the hydrodynamic size, which can be measured by NTA-FL as a slower diffusion. Within only a few minutes of measurement time, an analyte strand of an overall amount of five femtomole can be detected as shown for a random 30 base sequence, as well as for a 40 base sequence characteristic for a gene encoding antibiotic resistance. The proposed method shows that nanoparticle diffusion can be used as a tool for detecting characteristic DNA sequences and suggests the utilization in the detection of other biomarkers, as well as nanoparticles, macromolecules, bacteria, or viruses.

Diffusion measurements of nanoparticles can further be applied to investigate the viscosity or microstructure of complex media. PFG NMR is known as a non-invasive, direct, and absolute method that can measure diffusion coefficients of an ensemble of molecules in bulk solutions without being dependent on the optical properties of the medium and the particles. While the application for solid nanoparticles is limited due to line broadening because of dipolar coupling, it is shown that liquid core particles show a sharp NMR signal provided by the mobile molecules in the core, which can be used to measure the diffusion of the whole particle. It is shown that adding a fluorinated silane in the liquid core allows for ^{19}F NMR measurements, which open the door for the investigation of

nanoparticle diffusion even in complex media, that often show a complicated ^{1}H NMR spectrum. This can be used to measure particle diffusion in systems of different viscosity, as shown for aqueous glycerol solutions of different concentrations, and to investigate the diffusion mechanism of the particles in a hydrogel, as shown for HAMA gels of different polymer concentrations. This allows for quantifying the viscosity and for estimating the mesh size of the hydrogel. Although the 200 nm sized particles in HAMA gel were found to be at the lower limit of the method, the results can be interpreted qualitatively. As the liquid core particles offer the possibility for changing the particle size and surface functionalization, they provide a powerful system to measure nanoparticle diffusion in different biologically relevant environments.

As pointed out by Franconi[96], diffusion measurements by PFG NMR could be highly beneficial in the field of nanomedicine. Making nanoparticles in the range of hundreds of nanometers accessible for the investigation by PFG NMR allows for the use in different applications. For drug delivery, drug carrier vehicles in the size range of $< 200 - 500$ nm are often used to encapsulate a drug.[292–294] This is done in order to prevent the cargo from enzyme-mediated degradation and to be able to functionalize the surface.[294] A detailed understanding of the diffusion mechanism of nanoparticles in model hydrogels or biological tissue is therefore of importance to predict the diffusive behaviour of drug carriers and their interaction with the surrounding medium. Since information on the sub-micron structure of a biological hydrogel or tissue can be obtained from diffusion measurements of suitable diffusion nanosensors, the field is also of interest for tissue engineering. A deep knowledge and understanding of the microstructure is important to mimic the structure and mechanical properties of biological tissues.[295–298] Biological and artifical tissue can be compared by measuring the diffusion of nanoparticles with various sizes and surface chemistries.

The diffusion of nanoparticles has been shown to be highly affected by the material properties of the medium in which they are suspended. This includes physical properties of the medium like the viscosity, structural characteristics like the microstructure, as well as the presence of a characteristic molecule in the solution. Measuring nanoparticle diffusion further permits to draw conclusions on diffusion mechanisms and interactions between the particle and its environment. For the characterization of biological systems, diffusion measurements on nanoparticles can therefore serve as a valuable tool. With the methods

presented in the context of this thesis, the toolbox of diffusion measurements in biological systems is extended by the introduction of DNA origami as a diffusion nanosensor measured by NTA-FL, and the application of PFG NMR to liquid core particles of a biologically relevant size of around 200 nm. PFG NMR offers the possibility to examine complex and optically inaccessible systems. If correctly implemented, the presented diffusion methods provide valuable information regarding the presence of analytes and the structure of complex biological samples.

A Appendix

A.1 Methods

A.1.1 Settings for NTA-FL of DNA Origami

The measurements were performed on a *Nanosight NS300* machine from *Malvern Panalytical* that is equipped with a microscope objective attached to a sCMOS camera with a frame rate of 25 frames/s. The camera level was set to 15. The focus was set individually for each sample. A laser wavelength of 488 nm was used. For the NTA-FL measurements on the DNA origami, SYBR gold was used to obtain fluorescent staining of the nanosensors. A 500 nm high pass filter was used to restrict the measured signal to the emitted light of the fluorophore. The same laser wavelength was used for NTA measurements. The laser power was less than 55 mW. Unless otherwise specified, the measurements were performed at 20 °C. The built-in software *Nanosight NTA 3.4* was used for analysis of the captured videos. Unless further specified, the settings were chosen to be a detection threshold of 5, blur 5×5, max jump distance of 12, and min track length of 5.

To prevent bleaching of the fluorophore, the sample was flushed through the flow chamber at a flow speed of 2 µl/s, which corresponds to an infusion rate of 50. Each sample was measured five times for 60 s each unless otherwise noted. Between two repeats, the flow cell was flushed for 10 s at an infusion rate of 200 (flow speed 8 µl/s). The flow chamber was flushed with the pure, filtered buffer between two samples. For DNA origami concentrations of 5 pM, the number of tracked origami structures per experiment was around 50 000 (83 zeptomole).

A.1.2 Fabrication of Oil-Filled Core-Shell Particles

Oil-filled core-shell nanoparticles with solid shells made of PMMA polymer and liquid cores containing hexadecane and SilF7 were fabricated using a phase separation method optimized for the PFG NMR measurements.

An aqueous solution of 0.2 % SDS was prepared by dissolving 0.1 g SDS in 50 ml water. In a second vial, 0.166 g PMMA and 4.582 g DCM were mixed. 0.25 g hexadecane and 100 µl SilF7 were added to this mixture, which was gently stirred in order to generate a uniform organic phase. To form a stable oil-in-water emulsion, the resulting liquid was slowly added over 60 s to the SDS solution, which was stirred meanwhile using an ultrasound homogenizer (cycle 0.5, amplitude 100 %). 0.25 g acetone were added in order to reduce foaming. Another 40 s of ultrasonication were applied to achieve a reduction of the particle size down to the range of a few hundreds of nanometers. Afterwards, the sample was diluted using 7.5 g of the aqueous SDS solution to stabilize the dispersion. Finally, this was transferred to a flat beaker and left in a fume hood overnight to evaporate the DCM and acetone. This protocol allows for the fabrication of nanoparticles with a solid PMMA shell that encapsulates a liquid core of hexadecane and SilF7.

A.1.3 Preparation of HAMA Gels

The functionalization of HA polymer to obtain methacrylated HA was performed by my colleague Dimitris Missirlis. The following protocol was used in analogy to the literature.[299] Sodium hyaluronate with 100 kDa molecular weight was dissolved in milliQ water at a final concentration of 1 % w/v.The pH was adjusted to 9 and the solution was continuously and vigorously stirred while monitoring the pH. A 5x molar excess of methacrylic anhydride to the repeat unit were slowly added, and the solution turned opaque due to phase separation. 1 N NaOH was regularly added to keep the pH of the reaction mixture between 7 and 9. After 2.5 h, the reaction mixture was centrifuged and the hyaluronic acid methacrylate was precipitated in 5x volume excess of cold acetone, and washed 2 times with cold acetone. Finally, the precipitate was dissolved in milliQ water and lyophilized to obtain a white powder that was stored at −20 °C. A stock solution of 4 % w/v in PBS was used for gel preparation. Finally, the degree of functionalization was investigated by me using ^{1}H NMR, which yielded a degree of 14 %. The NMR spectrum

showed that the product contained a small amount of methacrylic anhydride at around half the molar concentration than the methacrylate bound to the polymer. However, this can be estimated to have a minor effect of $< 3\,\%$ when estimating the mass ratio of the polymer, causing e.g. an actual concentration of $0.97\,\%$ in the gel of nominal $1.0\,\%$.

A.1.4 Used Buffers

Information about the components in the different buffers used in the context of this thesis are given in table A.1.

Table A.1: Buffer information

	$TE/MgCl_2$	$TA/MgCl_2$	0.5x $TA/MgCl_2$	$TAE/MgCl_2$
Tris (mM)	5	40	20	40
Acetic Acid (mM)		20	10	20
EDTA (mM)	1			1
$MgCl_2$ (mM)	14	14	7	14

A.2 Evaluation Methodology

A.2.1 Calculation of Uncertainties

The uncertainties of the different measures evaluated from NTA, NTA-FL, and PFG NMR experiments are calculated using the Gaussian error propagation,

$$\Delta f(x_i) = \sqrt{\sum_i \left(\frac{\partial f}{\partial x_i}\right)^2 \Delta x_i^2} \tag{A.1}$$

for any function f dependent on error-bearing measures x_i. Alternatively, a maximum error estimation based on error propagation is used, which follows

$$\Delta f(x_i) = \sum_i \left|\frac{\partial f}{\partial x_i}\right| \Delta x_i. \tag{A.2}$$

Maximum of Log-Normal Distribution

As mentioned in section 4.2.3, the results of NTA or NTA-FL experiments are always presented with the standard error of the (in most cases) five performed measurements as evaluated by the used software *Nanosight NTA 3.4*. To compare different measurements, the maximum of the log-normal distribution fit is calculated following

$$d_{\max} = \exp(\ln(x_{\mathrm{m}}) - \sigma^2). \tag{A.3}$$

The uncertainty is calculated from the fitting errors of the parameters $\ln(x_{\mathrm{m}})$ and σ using a maximum error estimation given by equation (A.2).

PFG NMR Exponential Decay

For the PFG NMR experiments, three experiments were performed in most cases. For ^{1}H measurements, two peaks for hexadecane were evaluated, while for ^{19}F NMR only the larger peak of SilF7 was taken into account. They were evaluated individually to obtain the diffusion coefficient D and its uncertainty ΔD, given as the standard error of the fitting parameter, if the evaluation was performed using a single exponential fit as given in equation (2.17).

To calculate the mean diffusion coefficient $\bar{D}$ and its uncertainty out of the $N = 6$ (^{1}H) or $N = 3$ (^{19}F) values of D and ΔD, different sources of uncertainty are taken into account. First, the mean value $\bar{D}$ is calculated as the arithmetic mean following

$$\bar{D} = \frac{1}{N} \sum_{i=1}^{N} D_i. \tag{A.4}$$

The standard error of the mean diffusion coefficient was calculated using

$$SEM_{\bar{D}} = \frac{1}{\sqrt{N}} \sqrt{\frac{1}{N-1} \sum_{i=1}^{N} (D_i - \bar{D})^2}. \tag{A.5}$$

Since the results of the individual measurements are not correlated, Gaussian error propagation is used to calculate the uncertainty of the mean diffusion coefficient $STD_{\bar{D}}$ following equation (A.1). Here, this leads to

$$STD_{\bar{D}} = \sqrt{\sum_{i=1}^{N} \left(\frac{\partial \bar{D}}{\partial D_i} \right)^2 \Delta D_i^2} = \frac{1}{N} \sqrt{\sum_{i=1}^{N} \Delta D_i^2}. \tag{A.6}$$

The results of equations (A.5) and (A.6) can be added using Gaussian error propagation to yield

$$\Delta \bar{D} = \sqrt{SEM_{\bar{D}}^2 + STD_{\bar{D}}^2}. \tag{A.7}$$

For the sake of simplicity, the mean values $\bar{D}$ and their uncertainty $\Delta \bar{D}$ are given as $D = \bar{D} \pm \Delta \bar{D}$ in the text.

PFG NMR Gamma Distribution

For the evaluation of PFG NMR measurements using the gamma distribution of the diffusion coefficient, not only the mean $\langle D \rangle$ of the distribution can be obtained, but also its standard deviation σ_{D}. Both values are averaged using the arithmetic mean equation (A.4). For the standard form of the gamma distribution model, which is not number-weighted as given in section 2.2.1, a clear connection between fitting parameters and diffusion coefficient is given in the literature.[145] However, for the number-weighted form of the fit model as derived in section 5.3.1, this connection is no longer valid. Therefore, the mean diffusion coefficient and its standard deivation were obtained from the weighted mean squareroot of the second moment of the distribution. Giving an uncertainty of both measures arising from fitting errors is therefore not straightforward. Instead, from the quality of the fit, it is assumed that the error of the mean diffusion coefficient should be in the range of, or smaller than the uncertainty from the fitting error in case of the exponential fit, which is smaller than 3 % as evaluated for measurements in different glycerol solutions.

Uncertainty of Shell Thickness (Oil-Filled Core-Shell Particles)

The shell thickness of the oil-filled core-shell particles is calcualted by comparing the intensities of two NMR peaks, namely the peak at $\delta_1 \approx 1.7\,\mathrm{ppm}$, which is assigned to SDS, and $\delta_2 \approx 1.3\,\mathrm{ppm}$, where peaks of SDS and hexadecane are overlapping. Two hydrogen atoms per molecules SDS are included in δ_1, while 18 atoms of SDS and 28 of an hexadecane molecules contribute to δ_2.

The relative areas under these peaks are $A_1 = 100$ and $A_2 = 1030.6197$. Using these and the information of the number of contributing atoms per molecule, the radius of the core can be calculated, assuming that SDS in only present inside the core, and SDS is limited to outside of the particles. The calculation follows

$$\tilde{N}_{\mathrm{SDS}} = \frac{A_1}{2} \tag{A.8}$$

$$\tilde{N}_{\mathrm{hex}} = \frac{1}{28}(A_2 - 18 \cdot \tilde{N}_{\mathrm{SDS}}) \tag{A.9}$$

where $\tilde{N}_{\mathrm{SDS}}$ and $\tilde{N}_{\mathrm{hex}}$ are the relative numbers of SDS and hexadecane molecules. Using the known mass of SDS contained in the solution, which is 1 mg in 500 µl, the number of SDS molecules $N_{\mathrm{SDS}} = m_{\mathrm{SDS}}/M_{\mathrm{SDS}}$ in the samples can be used to calculate the total number of hexadecane molecules as

$$N_{\mathrm{hex}} = N_{\mathrm{SDS}} \cdot \frac{\tilde{N}_{\mathrm{hex}}}{\tilde{N}_{\mathrm{SDS}}}. \tag{A.10}$$

This number corresponds to a total volume of hexadecane of

$$V_{\mathrm{hex}} = \frac{N_{\mathrm{hex}} \cdot M_{\mathrm{hex}}}{\rho_{\mathrm{hex}}}, \tag{A.11}$$

where M_{hex} and ρ_{hex} denote molecular mass and density of hexadecane, respectively. By dividing the overall volume of hexadecane by the known number of particles N_{par}, the volume of the particle core can calculated by $V_{\mathrm{core}} = V_{\mathrm{hex}}/N_{\mathrm{par}}$. From this, the inner radius can be calculated to be

$$R_{\mathrm{i}} = \left(\frac{3V_{\mathrm{core}}}{4\pi}\right)^{1/3}. \tag{A.12}$$

Table A.2: Summary of the parameters, their values, and the respective errors as used for the estimation of the uncertainty of the shell thickness of the liquid core particles. Details about the calculation are given in the text.

Measure	Value	Error	Note
A_1	100	0.1	0.1 %
A_2	1030.62	1.03	0.1 %
$\tilde{N}_{\mathrm{SDS}}$	50	1.05	2 % + error propagation
$\tilde{N}_{\mathrm{hex}}$	4.66	0.71	
N_{SDS} (mol)	$3.47 \cdot 10^{-6}$	$3.47 \cdot 10^{-8}$	1% weighting error
N_{hex} (mol)	$3.24 \cdot 10^{-7}$	$5.94 \cdot 10^{-8}$	
m_{hex} (g)	$7.33 \cdot 10^{-5}$	$1.34 \cdot 10^{-5}$	
V_{hex} (m^3)	$9.48 \cdot 10^{-11}$	$1.74 \cdot 10^{-11}$	
N_{par}	$1.02 \cdot 10^{11}$	$1.02 \cdot 10^{10}$	10% of N_{par}
V_{core} (m^3)	$9.29 \cdot 10^{-22}$	$2.63 \cdot 10^{-22}$	
R_{i} (m)	$6.05 \cdot 10^{-8}$	$5.72 \cdot 10^{-9}$	

The error estimation follows the maximum error estimation given in equation (A.2). The results of the intermediate steps of the calculation, as well as their errors are shown in table A.2. The column 'Note' tells the errors that are estimated. The uncertainty of the areas in the NMR spectrum is estimated from the difference in determining the area in the NMR spectrum in different approaches. For the relative number of SDS molecules $\tilde{N}_{\mathrm{SDS}}$, an error of 2 % SDS (compared to the total amount of SDS) inside the core of the particles is assumed, so that only around 98 % of the total amount of the SDS are present in the solution outside the particles. For the concentration of SDS in the solution, presented by N_{SDS}, a weighting error of 1 % is assumed. The number of particles N_{par} is assumed to be uncertain by aorund 10 %, as given by the standard deviation of the concentrations obtained by NTA measurements on the same sample, but with different settings. These measurements were performed on another sample than the one evaluated here, but are assumed to serve as a good approximation.

The resulting value of the inner radius is therefore $R_{\mathrm{i}} = (60.5 \pm 5.7)\,\mathrm{nm}$. Compared to an outer radius of $R = 119.7\,\mathrm{nm}$, with the standard deviation of 37.6 nm as obtained by fitting a number PSD distribution to the PFG NMR intensity attenuation, the inner diameter is approximated as 50 % of the outer radius for all particles.

Uncertainty of Mesh Size (Hydrogel)

To obtain the uncertainty of the mesh size of HAMA gels as calculated in equation (5.5), a maximum error estimation following equation (A.2) is performed. The uncertainty of the shell thickness $R_{\mathrm{shell}} = R - R_{\mathrm{i}}$ is

$$\Delta R_{\mathrm{shell}} = \Delta R + \Delta R_{\mathrm{i}} = 31.7\,\mathrm{nm}. \tag{A.13}$$

Here, the value of $\Delta R_{\mathrm{i}} = 5.7\,\mathrm{nm}$ (see table A.2) is used as a maximum value of the shell thickness error. For ΔR, the standard deviation $\sigma_{\mathrm{R}} = 16.0\,\mathrm{nm}$ of the used particles as evaluated from fitting the number PSD onto the PFG NMR intensity attenuation is used.

The total uncertainty of the mesh sizes evaluated by equation (5.5) for the particle system used in section 5.4.2 can therefore be estimated as

$$\Delta\xi = \frac{1}{2}\sqrt{\frac{5\Delta}{D}}\Delta D + 2\Delta R_{\mathrm{shell}}. \tag{A.14}$$

The uncertainty of the diffusion coefficient as calculated from equation (A.7) is used for each sample. The resulting values of $\Delta\xi \approx 70\,\mathrm{nm}$ show that the uncertainty of the mesh size is mostly caused by the polydispersity of the particles and the uncertainty of the shell thickness.

A.2.2 Evaluating PFG NMR Results Assuming a Number PSD

In section 5.3.1, the signal attenuation of a PFG NMR intensity attenuation plot is given for a number weighted gamma distribution of the diffusion coefficients. The result given

in equation (5.3) is calculated following Appendix A in a study by Roeding et al.[145] as follows:

$$\tilde{I}(b) = I_0 \int_0^\infty \tilde{P}(D) \exp(-bD) \mathrm{d}D \tag{A.15}$$

$$= I_0 \int_0^\infty D^{\kappa+2} D_0^{-3} \frac{\exp(-D/\theta)}{\Gamma(\kappa)\theta^\kappa} \exp(-bD) \mathrm{d}D \tag{A.16}$$

$$= I_0 \theta^{-\kappa} \int_0^\infty D^{\kappa+2} D_0^{-3} \frac{1}{\Gamma(\kappa)} \exp(-D/\theta - bD) \mathrm{d}D \tag{A.17}$$

$$= I_0 \theta^{-\kappa} \int_0^\infty D^{\kappa+2} D_0^{-3} \frac{1}{\Gamma(\kappa)} \cdot \exp\left(-D/\left(\frac{1}{b+1/\theta}\right)\right) \mathrm{d}D \tag{A.18}$$

$$= I_0 \theta^{-\kappa} \left(\frac{1}{b+1/\theta}\right)^\kappa \int_0^\infty D^{\kappa+2} D_0^{-3} \frac{1}{\Gamma(\kappa)\left(\frac{1}{b+1/\theta}\right)^\kappa} \cdot \exp\left(-D/\left(\frac{1}{b+1/\theta}\right)\right) \mathrm{d}D \tag{A.19}$$

$$= I_0 \theta^{-\kappa} \left(\frac{1}{b+1/\theta}\right)^\kappa \int_0^\infty \tilde{P}\left(D; \kappa, \frac{1}{b+1/\theta}\right) \mathrm{d}D \tag{A.20}$$

$$\overset{(*)}{=} I_0 \theta^{-\kappa} (b+1/\theta)^{-\kappa} \tag{A.21}$$

$$= I_0 (1+b\theta)^{-\kappa} \tag{A.22}$$

using (*)

$$\int_0^\infty \tilde{P}\left(D; \kappa, \frac{1}{b+1/\theta}\right) \mathrm{d}D = \int_0^\infty D^{\kappa+2} D_0^{-3} \frac{\exp\left(-D/\left(\frac{1}{b+1/\theta}\right)\right)}{\Gamma(\kappa)\left(\frac{1}{b+1/\theta}\right)^\kappa} \mathrm{d}D = 1 \tag{A.23}$$

A.3 Experimental Results

A.3.1 List of NTA-FL Results

When fitting the log-normal distribution to the PSD obtained by NTA-FL, the maximum value can be obtained from the fitting parameters. For most of the experiments shown in chapter 4, the exact values of the distribution maximum and their uncertainties are given with the figure. For the plot showing the size shift with respect to the concentration of IM strands in figure 4.18, the values are given in table A.3.

Table A.3: List of the maximum values of the log-normal distribution and their uncertainties for the measurements shown in figure 4.18.

Concentration IM (pM)	$d_{\max}$ (nm)	$\Delta d_{\max}$ (nm)
0.0	97.8	0.5
2.5	101.7	0.5
5.0	112.0	0.8
7.5	112.6	1.1
10.0	114.8	1.0
12.5	118.3	0.8
15.0	122.0	1.2
25.0	129.7	1.2
35.0	130.6	1.0
50.0	127.1	1.1
75.0	128.8	0.9
100.0	130.7	1.0

A.3.2 ^{19}F PFG NMR Attenuation Plots

Comparison ^{1}H PFG NMR vs ^{19}F NMR on the same sample of particles in water

Figure A.1 shows PFG NMR measurements on the same sample of particles suspended in water. The oil-filled core-shell particles had a core containing hexadecane and SilF7, so that the two peaks of hexadecane were evaluated in the ^{1}H PFG NMR experiment, while the SilF7 provides spins for the ^{19}F PFG NMR. In the ^{1}H experiment, the value obtained for the first gradient was left out, because an impact of the overlapping SDS peak was assumed. To compare between the two measurements, exponential decay were fitted on all curves and averaged. The resulting diffusion coefficients are:

$$D_{^{1}\mathrm{H}} = (2.64 \pm 0.08) \cdot 10^{-12}\,\mathrm{m}^2/\mathrm{s} \tag{A.24}$$

$$D_{^{19}\mathrm{F}} = (2.67 \pm 0.14) \cdot 10^{-12}\,\mathrm{m}^2/\mathrm{s} \tag{A.25}$$

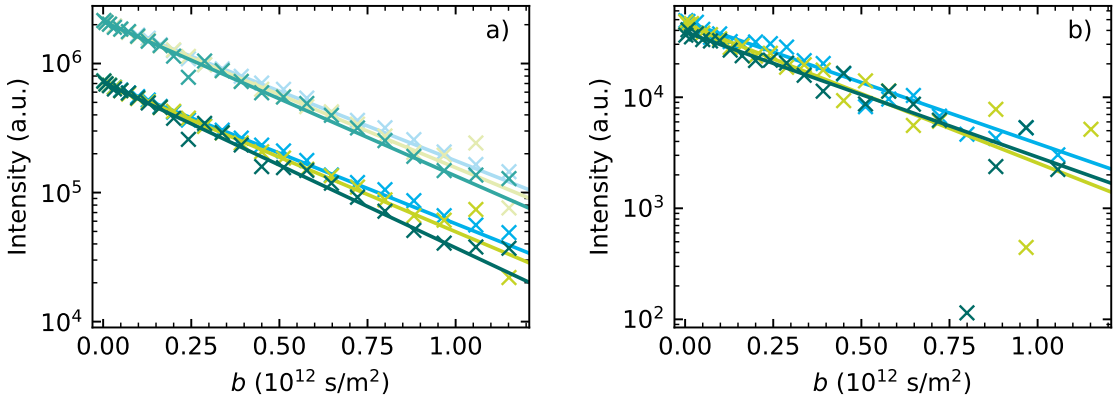

Figure A.1: Comparison of ^{1}H and ^{19}F PFG NMR on the same sample of oil-filled core-shell particles with a core of hexcadecane and FilF7, suspended in water. Both plots were fitted using an exponential decay as given in equation (2.17). The measurements were performed using $\delta_g = 2.5\,\text{ms}$ and $\Delta = 50\,\text{ms}$. a) ^{1}H PFG NMR, 32 scans were performed. b) ^{19}F PFG NMR, 128 scans were performed.

It has to be noted that in some samples, when less scans were measured, the agreement between the ^{1}H and ^{19}F measurements was worse than for the sample shown here. This can range up to 20 %. However, there was no clear trend of the ^{19}F compared to the ^{1}H measurements. It is assumed that – if measurement conditions are chosen appropriately – ^{1}H and ^{19}F measurements can be assumed to give the same results. Nevertheless, measurements on the same nucleus were performed to compare within a series of measurements.

Intensity attenuation plots for glycerol and HAMA gel

Exemplary intensity attenuation plots for ^{1}H PFG NMR measurements on oil-filled core-shell particles in aqueous glycerol solutions and ^{19}F PFG NMR measurements in 1 % HAMA gel are shown in figure A.2.

A.3.3 Discussion of Possible Artifacts in PFG NMR Measurements in Complex Systems

As mentioned in section 5.4, the interpretation of PFG NMR measurements of oil-filled core-shell particles recorded in aqueous 60 % glycerol solution in case of small diffusion times Δ requires consideration of the fluid inside the core with respect to the particle as a

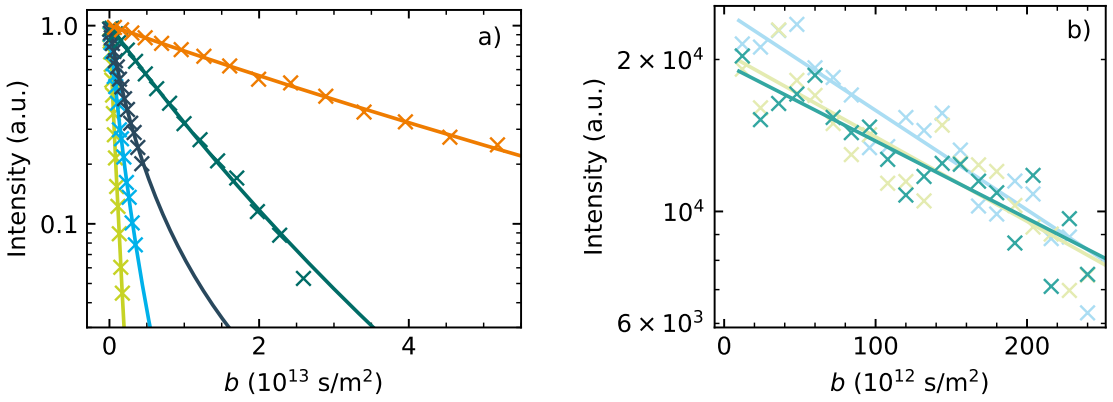

Figure A.2: a) Full representation of figure 5.9a, where a section was shown. The intensity attenuations of exemplary measurements on oil-filled core-shell particles in aqueous glycerol solutions are shown as measured by ^{1}H PFG NMR. The colors denote increasing concentration of glycerol as follows: light green - 0 % glycerol, light blue - 20 % glycerol, dark blue - 40 % glycerol, dark green - 60 % glycerol, orange - 80 % glycerol. The fits follow the number-weighted gamma distribution model in equation (5.3). Parameters $\Delta = 100$ ms and $\delta_g = 5$ ms were used, and 32 scans were recorded. For the samples in 60 % and 80 % glycerol, the diffusion times were increased to 150 ms and 500 ms. b) Intensity attenuation plot of oil-filled core-shell particles containing hexadecane and SilF7, suspended in 1 % HAMA gel as measured by ^{19}F PFG NMR. Parametes were $\Delta = 500$ ms, $\delta_g = 5$ ms, and 64 scans were performed. The fits follow a single exponential decay as given in Eg. (2.17). The resulting averaged diffusion coefficient is part of figure 5.10.

whole, and the impacts of PFG NMR in this system. In short, for the measured diffusion times $\Delta = 11.93$ ms, 20 ms, and 50 ms the spectra recorded for the higher gradient values show broadening and a loss of the phase. The measurement using $\Delta = 100$ ms shows a minor effect. This leads to an intensity attenuation plot as for instance shown in Fig. A.3a for a diffusion time of 20 ms measured in the 60 % glycerol solution. Measurement conditions are given in the figure caption. For the higher diffusion times (shown in Fig. 5.8b) the effect was not observed. However, for the latter case the maximum gradient was reduced upon increasing the diffusion time while keeping the gradient length constant, to cover a reasonable range of the parameter b for the expected diffusion coefficient.

It is therefore not easy to indentify what effects might cause the unphysical decay of the signal attenuation plot. It is not obvious whether the short diffusion time (with respect to the gradient length), or the large gradients are responsible for the phase problems, or if other effects arise in the present system. However, one aspect in the measurements might provide a hint: While all three mentioned measurements measured

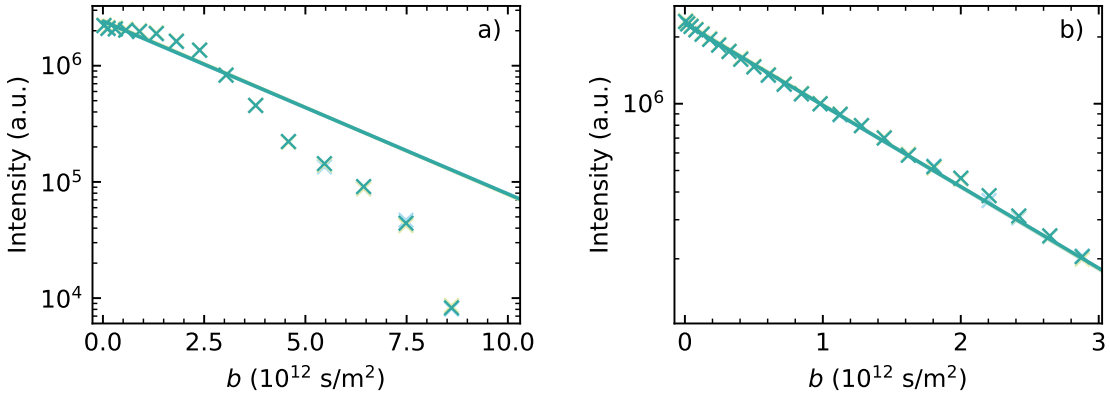

Figure A.3: a) Signal attenuation of the liquid core particles suspended in an aqueous 60 % glycerol solution, measured by ^{1}H PFG NMR. Only the evaluation of the higher hexadecane peak is shown. Although the points overlap, three measurements are shown. Measurements were performed at $\Delta = 20\,\text{ms}$, $\delta_g = 5\,\text{ms}$, and 32 scans. The particle concentration was $5 \cdot 10^{11}$ particles/ml. b) ^{1}H PFG NMR intensity attenuation for a sample of liquid core particles in water. Used parameters were a concentration of around $2 \cdot 10^{12}$ particles/ml, $\Delta = 25\,\text{ms}$, $\delta_g = 2.5\,\text{ms}$, and 32 scans.

at a gradient strength $g > 17\,\text{T/m}$ show a loss of the phase, the apparent evaluated diffusion coefficient steadily decreases from $D_{\Delta=11.93\,\text{ms}} = (4.7 \pm 0.3) \cdot 10^{-13}\,\text{m}^2/\text{s}$ over $D_{\Delta=20\,\text{ms}} = (3.6 \pm 0.2) \cdot 10^{-13}\,\text{m}^2/\text{s}$ and $D_{\Delta=50\,\text{ms}} = (1.5 \pm 0.1) \cdot 10^{-13}\,\text{m}^2/\text{s}$ towards the long-term diffusion coefficient $D_{\Delta=800\,\text{ms}} = (1.1 \pm 0.1) \cdot 10^{-13}\,\text{m}^2/\text{s}$ measured using smaller gradient strengths of around 4 T/m (all values obtained using a single exponential fit for the attenuation of the larger peak of hexadecane). This suggests that the artifact is larger for shorter diffusion times.

In the following, different possible explanations are listed, as well as a discussion of the potential impact on the interpretation of the measurements in the HAMA gel (section 5.4). For the comparison with measurements in the HAMA gel it has to be noted, that the unphysical echo decay due to phase loss does not seem to play a role in the attenuation plots. However, the effect might nevertheless affect the measurements, but could undetected due to the S/N. Further, the HAMA observations contain a surprisingly slightly decreasing mean covered distance for increasing diffusion times. While this could also be attributed to the higher S/N of the 19F PFG NMR measurements, I will nevertheless discuss possible problems in the following that could explain this behaviour of the apparently decreasing covered distance. Therefore the possible effects for the HAMA samples are included in the following discussion.

- **Eddy currents:** For the measurement in figure A.3a, strong gradients of up to around 17.4 T/m were applied. The strong gradients could give rise to eddy currents, which can possibly cause problems for the measurement if they are not recovered at the moment of the signal acquisition. Eddy currents are a well-discussed phenomenon in PFG NMR, see e.g. literature by W. Price[119,300]. To decrease the intensity of eddy currents, sine shaped pulses are used, and a time delay is implemented between the second gradient pulse and the data acquisition. In the diffSte pulse sequence used for the diffusion measurements, a delay of 1 ms was used before the acquisition of the FID. Although it has not been calculated or estimated if this is enough to let the eddy currents fully decay, a comparison to another measurement gives rise to the assumption that eddy currents should not have a big impact on the shown measurement in glycerol. Fig A.3b shows a measurement of the particles in water. Specific parameters of the measurement are given in the figure caption. The measurement in water is performed at slightly lower maximum gradient (15.4 T/m), but also as a shorter gradient time ($\delta_g = 2.5$ s). Since the generation of eddy currents is dependent on the change in the magnetic field strength dB/dt, the eddy currents for the shorter gradient pulse are assumed to be larger than for a longer gradient pulse. As the effect of the unphysical echo attenuation was not observed in the water sample, the effect of eddy currents is assumed to be negligible for the glycerol sample as well. For completeness, it is noted that the two measurements shown in figure A.3a and b are recorded at different dates and the instrument was moved to another lab in between, but with the usual experimental controls this is not considered to affect the measurements.

- **Sedimentation/buoyancy and convection:** While it can be assumed that the particles in water do not show density-driven movement, this can not be excluded for the case of glycerol. In water, centrifugation of the particles was tested to force them to sediment or float, with the result that no solid sediment was observed, but it seemed that the larger particles were distributed more in the upper part of the suspension, while in the lower part more small particles were found. From this result, it is assumed that the particles in water should have a comparable density overall (including shell and liquid core) compared to the surrounding water and the effects of density-driven movement in a water sample should be negligible.

However, if they are suspended in a glycerol solution, the density difference is larger, which could lead to slight buoyancy effect. Flow (like convection or density-driven movement) causes a shift in the phase of the NMR signal. However, it is assumed that the effect of flow should have a larger impact for longer diffusion times, which does not seem to be the case when considering the measurements in glycerol for larger diffusion times. Density-driven movement therefore seems to play a negligible role in the present systems. The same is assumed for convection.

- **Dephasing during high intensity gradient pulses** To be able to measure small diffusion coefficients as present in highly concentrated glycerol solution or in HAMA gel, high gradient strengths and long gradient durations have to be used to reach values of b that allow for a reasonable fit on the echo attenuation plot. However, if the diffusing spins cover a considerable distance during the gradient, the phase encoding of their location becomes blurred, which leads to an unphysical negative curvature of the echo attenuation as already discussed in section 5.2.6.[113] It seems very likely that the loss of phase is caused by this effect since it matches the observed behaviour. This phenomenon is also mentioned in the literature[113].The decrease in the apparent diffusion coefficient as evaluated from the disturbed echo decay plots in the glycerol sample, however, shows that this effect is smaller for higher diffusion times. It is assumed that this can be attributed to an increasing range of covered b values.

  HAMA gel: All measurements in the HAMA gel were performed at the same gradient conditions as the aforementioned glycerol sample, it is therefore likely that the effect of dephasing due to movement during the gradient – if this is indeed the artifact – could also affect the measurements in HAMA gel. The discussed effect of a high gradient intensity could well explain the behaviour of the unphysical decrease in the apparent mean covered distance with increasing diffusion time. For the measurements in glycerol, it was observed that the impact of overestimating the diffusion coefficient is higher for small diffusion times, which would in turn lead to an overestimation of the mean covered distance.

  While this effect can qualitatively explain the unphysical estimates at short diffusion times in both the glycerol and the HAMA sample, it is hard to quantify this effect

for the hydrogel sample. One could assume that in the hydrogel the effect is smaller than for the case of the glycerol sample, since fluorine ^{19}F nuclei that are used in the HAMA sample 'experience' the effect of the magnetic field less than hydrogen nuclei due to the gyromagnetic ratio. This amounts a difference of a few percent in the gyromagnetic ratio. Further, if we assume the particles to be less mobile in the gel compared to the homogeneous glycerol solution, we can assume that the covered distance is smaller and hence the effect of the dephasing is less pronounced. On the other hand, the apparent diffusion coefficient in the hydrogel seems to be smaller than in the glycerol sample. It is unclear if this could increase the impact of the phase loss in the intensity attenuation fit. Even if it is unclear how big this effect in the gel sample is, it can be assumed that it could lead to an overestimation of the apparent diffusion coefficient. However, it can be assumed that his effect is less pronounced for larger diffusion times.

- **Diffusive diffraction:** Diffusive behaviour in restricted geometries can be investigated using diffraction phenomena as described e.g. by W. Price[119] and P. Callaghan[113]. In short, for diffusing species trapped inside a cavity, the echo attenuation plot shows dips dependent on the geometry of the cavity. This phenomenon is present if the the condition $D\Delta/a^2 > 1$ is fulfilled, where a is the radius of the restricting pore for the case of a spherical cavity. If we only consider the diffusion of the molecules in the particle core and assume the particle to be static, so that D equals the free diffusion coefficient of the hexadecane molecules and $a \approx 60\,\mathrm{nm}$, this condition is fulfilled for the liquid molecules diffusing inside the particle core. It can therefore be assumed that diffusive diffraction effects play a role here. The first diffraction dip is then located at $2q \cdot a \approx 1$, with $q = \gamma\delta_\mathrm{g} g$. However, if we estimate this for the given conditions of $g = 17\,\mathrm{T/m}$ and $\delta_\mathrm{g} = 5\,\mathrm{ms}$, we are not reaching high enough values of q to image this first diffraction peak.[119] It is intuitively reasonable that the apparent diffusion coefficient could be overestimated when taking only the decay part of the curve towards the dip into account. However, the values of q are the same for the three mentioned measurements in the glycerol sample that showed phase loss, but there is no obvious reason why the apparent diffusion coefficient should change for increasing diffusion time.

Further, it has to be taken into account that the particles diffuse inside the glycerol solution. This creates a superimposing effect on the echo attenuation, which makes the present system much more complicated than just considering the diffusive diffraction of molecules inside a static particle. To my knowledge, there is no study about the case of diffraction inside cavities (particles) that themselves also move. It can therefore neither be ruled out nor assumed that diffusive diffraction plays a role in the present system. All in all, diffraction phenomena represent a very interesting field. However, it seems that we are outside a reasonable regime for these findings, and the superimposed movement of the particles complicated the interpretation of the system. Nevertheless, it is assumed that the dips generated by the diffraction could in principle affect the measurements of the particles, although it is unclear to which extent. Studying diffusive diffraction in the given particle system would be an interesting topic and could be subject of further investigation, but lies outside the scope of this thesis.

HAMA gel: Since we cannot rule out that diffraction could be responsible for the loss of phase observed in the glycerol samples, the effect on the HAMA gel samples has to be estimated. Since we are in the same regime of gradient intensity as in the glycerol samples that showed the phase problems, it can be asummed that – if the effect plays a role in the HAMA samples – it would lead to an overestimation of the real diffusion coefficient, same as for the samples in glycerol. However, it is assumed that all measurements should be similarly affected since the distance of the maximum used gradient intensity values to the theoretical position of the first dip should be roughly the same for all samples. It is therefore unclear whether the diffractive behaviour could explain the apparent decay of the mean covered distance for the particles in HAMA gel.

Considering the different discussed effects leads me to conlude that two phenomena, namely dephasing due to high intensity gradient pulses, or diffusive diffraction are most likely the cause of the unphysical observations of phase loss in the glycerol sample or the decreasing mean covered distance for increasing diffusion times in the HAMA gel samples. It can be concluded, that both effects could arise in the HAMA sample, which could lead to an overestimation of the measured apparent diffusion coefficient, however by an unknown extent. Nevertheless, the method of PFG NMR measurements using

Table A.4: Diffusion coefficients of the PFG NMR experiments shown in this thesis that are evaluated using an exponential decay. 'Nuc.' denotes the nucleus, 'NS' is the number of scans. For the ^{1}H experiments, three measurements were performed and both hexadecane peaks were evaluated, unless otherwise specified in the notes. For ^{19}F experiments, one peak was evaluated for three measurements, unless the notes denote something else. *Notes:* (1): Only one measurement (1 peak) is evaluated for the exemplary plot; (2): Only two measurements performed due to time restrictions.

Fig.	Sample	Nuc.	δ_g (ms)	Δ (ms)	NS	D (m^2/s)	ΔD (m^2/s)	Note
5.5	0.2 % SDS sol.	^{1}H	4.1	23	128	$1.51 \cdot 10^{-10}$	$0.15 \cdot 10^{-10}$	(1)
						$2.38 \cdot 10^{-12}$	$0.04 \cdot 10^{-12}$	(1)
5.10a	1 % HAMA	^{19}F	5	11.93	64	$3.85 \cdot 10^{-13}$	$2.27 \cdot 10^{-14}$	(2)
				20		$2.94 \cdot 10^{-13}$	$1.19 \cdot 10^{-14}$	(2)
				40		$1.07 \cdot 10^{-13}$	$9.42 \cdot 10^{-15}$	(2)
				70		$5.53 \cdot 10^{-14}$	$4.10 \cdot 10^{-15}$	(2)
				100		$3.92 \cdot 10^{-14}$	$5.71 \cdot 10^{-15}$	(2)
				150		$2.26 \cdot 10^{-14}$	$3.40 \cdot 10^{-15}$	(2)
				200		$1.84 \cdot 10^{-14}$	$2.48 \cdot 10^{-15}$	(2)
				300		$9.55 \cdot 10^{-15}$	$1.11 \cdot 10^{-15}$	(2)
				500		$3.97 \cdot 10^{-15}$	$3.87 \cdot 10^{-16}$	
				800		$2.49 \cdot 10^{-15}$	$6.65 \cdot 10^{-16}$	(2)
5.10b	0.8 % HAMA	^{19}F	5	500	64	$5.92 \cdot 10^{-15}$	$3.92 \cdot 10^{-16}$	
	1.2 % HAMA					$2.57 \cdot 10^{-15}$	$2.95 \cdot 10^{-16}$	
A.1	Water	^{1}H	2.5	50	32	$2.64 \cdot 10^{-12}$	$7.50 \cdot 10^{-14}$	
		^{19}F			128	$2.67 \cdot 10^{-12}$	$1.43 \cdot 10^{-13}$	

liquid core particle gives accurate and reliable results for other measurement conditions. It is assumed that the impact of the discussed effects can be reduced by using smaller nanoparticles as discussed in section 5.5.

A.3.4 List of PFG NMR Results

Table A.4 lists diffusion coefficients and their uncertainties for all samples evaluated with an exponential decay (equation (2.17)). For each sample, two peaks of three measurements were used for the evaluation following equations (A.4) to (A.7), unless otherwise specified in the last column.

For the measurements evaluated assuming a number-weighted gamma distribution of the diffusion coefficient, the exact values and their standard deviations plotted in different figures are shown in Tab A.5.

Table A.5: Diffusion coefficients of the PFG NMR experiments shown in this thesis that are evaluated using the number-weighted gamma distribution. 'Nuc.' denotes the nucleus, 'NS' is the number of scans. For the ^{1}H experiments, three measurements were performed and both headecane peaks were evaluated, unless otherwise specified in the notes. For ^{19}F experiments, one peak was evaluated for three measurements, unless the notes denote something else. *Notes:* (3): Last gradient values left out due to dephasing; (4): Only three results averaged; (5): Only four results averaged

Fig.	Sample	Nuc.	δ_g (ms)	Δ (ms)	NS	D (m^2/s)	σ_D (m^2/s)	Note
5.6	Water	^{1}H	2.5	50	32	$3.55 \cdot 10^{-12}$	$1.15 \cdot 10^{-12}$	
5.8b	60 % Glyc.	^{1}H	5	100	32	$1.66 \cdot 10^{-13}$	$4.49 \cdot 10^{-14}$	(3), (4)
				150		$1.58 \cdot 10^{-13}$	$4.27 \cdot 10^{-14}$	
				200		$1.71 \cdot 10^{-13}$	$5.06 \cdot 10^{-14}$	
				500		$1.67 \cdot 10^{-13}$	$4.79 \cdot 10^{-14}$	
				800		$1.62 \cdot 10^{-13}$	$4.43 \cdot 10^{-14}$	(4)
5.9b	Water	^{1}H	5	100	32	$2.63 \cdot 10^{-12}$	$6.96 \cdot 10^{-13}$	
	20 % Glyc.			100		$1.47 \cdot 10^{-12}$	$5.21 \cdot 10^{-13}$	(5)
	40 % Glyc.			100		$8.54 \cdot 10^{-13}$	$3.43 \cdot 10^{-13}$	
	60 % Glyc.			150		$1.58 \cdot 10^{-13}$	$4.26 \cdot 10^{-14}$	
	80 % Glyc.			500		$4.68 \cdot 10^{-14}$	$1.52 \cdot 10^{-14}$	

Acknowledgements

All the work that was done in the past years with the results presented in this thesis was only possible with the help and support of so many wonderful people.

I would like to thank my supervisor Prof. Dr. Peer Fischer for giving me the opportunity to work in the MNMS group and for supporting me in going my own way by staying in Stuttgart. The care that you have always taken about every single group member and to make sure that everyone is healthy and happy, in both their career and personal life makes you a perfect supervisor. I especially enjoyed discussing physics with you as one of the few physicists in the group.

Thank you, Mariana Alarcón Correa and Nicolás Moreno-Gómez, for working with me on the projects presented in this thesis. What a funny and nice incident that I got to work in my two main projects with the two Colombian colleagues, and I couldn't have asked for better colleagues for this. Thank you for all the work-related support and always having time to help when I had questions or wanted to discuss anything. I enjoyed spending time with you and learn about elections, health insurance system, or food in Colombia.

Thank you, Jan-Philipp Günther, for introducing a physicist to the world of chemistry, all the time that you spent in the lab to explain pipettes, instruments, or ChemLab safety, and to teach me your careful and accurate way of working. You always had a useful advice for me and had time to discuss whenever I texted you, even when you left the group. Thank you, Günter Majer, for introducing me to Max Planck Institute and teaching me so much about the PFG NMR instrument. You were always willing to help, and your deep knowledge about this instrument is being missed.

I would also like to thank all past and present group members of the Micro, Nano, and Molecular Systems group in Stuttgart and Heidelberg. Thank you, Nikhilesh, Lucie, Florian, Rahul, Vincent, Kai, Hyunah, Lovish, Hannah, Thanasi, and everyone else that is or was part of the group. It was a pleasure to work with you in such an international and interdisciplinary group. I further want to thank Helen, Jonas, Chris, Izar, Camila, Ulli, and Bernhard for their work related to this thesis. Special thanks go to Jutta, who keeps the group running and always helps us out.

Additional thanks go to all of my friends, especially to Andrea, Louis, Katharina, Maxim, Lukas, Elinor, Pirmin, Laurenz, and Nadia. I think there is no need to explain how important it is to have friends around you that you enjoy spending time with. I would also like to thank all of my Volleyball teammates. It meant a lot to me having you around for all the training sessions and matches when the group moved to Heidelberg and life became quiet at MPI-IS.

Special thanks go to my family. First, to my parents Anette and Ralf for always supporting me and believing in me. Growing up in a family that is so close and with so much love means a lot in life. I know that physics is not the topic that you are most interested in (or that you aim to understand), but this makes it even more valuable that you supported me on my way through studying and doing this PhD.

I further want to thank my wonderful sisters Britta and Greta. I cannot imagine better siblings to grow up with and I think a lot of who and where we are now is because of this connection. We chose very different topics in our studies, but I am glad that we can always learn from the others and give support in every situation of life. And, by the way, thanks for always having an open door whenever I am staying in Heidelberg.

Finally, thank you, Aaron, for always being there for me. I would never have managed to do this PhD (and especially write this thesis) without your endless support and love. You went through every up and down with me, listened to my explanations and stories every evening, helped me out with Python whenever I needed help, and supported me in every situation. Thank you for being there for me.

Bibliography

[1] Hubert G. M. Niesters. "Clinical virology in real time". In: *Journal of clinical virology: the official publication of the Pan American Society for Clinical Virology* 25 Suppl 3 (2002), S3–12. ISSN: 1386-6532. DOI: 10.1016/S1386-6532(02)00197-X.

[2] Xu-Xiang Zhang, Tong Zhang, and Herbert H. P. Fang. "Antibiotic resistance genes in water environment". In: *Applied microbiology and biotechnology* 82.3 (2009), pp. 397–414. DOI: 10.1007/s00253-008-1829-z.

[3] Shailendra Dwivedi et al. "Diseases and Molecular Diagnostics: A Step Closer to Precision Medicine". In: *Indian journal of clinical biochemistry: IJCB* 32.4 (2017), pp. 374–398. ISSN: 0970-1915. DOI: 10.1007/s12291-017-0688-8.

[4] Andreas Ziegler et al. "Personalized medicine using DNA biomarkers: a review". In: *Human genetics* 131.10 (2012), pp. 1627–1638. DOI: 10.1007/s00439-012-1188-9.

[5] Valentino D'Onofrio et al. "The Clinical Impact of Rapid Molecular Microbiological Diagnostics for Pathogen and Resistance Gene Identification in Patients With Sepsis: A Systematic Review". In: *Open forum infectious diseases* 7.10 (2020), ofaa352. ISSN: 2328-8957. DOI: 10.1093/ofid/ofaa352.

[6] K. B. Mullis and F. A. Faloona. "Specific synthesis of DNA in vitro via a polymerase-catalyzed chain reaction". In: *Methods in enzymology* 155 (1987), pp. 335–350. ISSN: 0076-6879. DOI: 10.1016/0076-6879(87)55023-6.

[7] J. A. Towbin. "Polymerase chain reaction and its uses as a diagnostic tool for cardiovascular disease". In: *Trends in cardiovascular medicine* 5.5 (1995), pp. 175–185. ISSN: 1050-1738. DOI: 10.1016/1050-1738(95)00059-I.

[8] Samuel Yang and Richard E. Rothman. “PCR-based diagnostics for infectious diseases: uses, limitations, and future applications in acute-care settings”. In: *The Lancet. Infectious diseases* 4.6 (2004), pp. 337–348. ISSN: 1473-3099. DOI: 10.1016/S1473-3099(04)01044-8.

[9] Muhammad Sajeer Paramabth and Manoj Varma. “Demystifying PCR tests, challenges, alternatives, and future: A quick review focusing on COVID and fungal infections”. In: *Biochemistry and molecular biology education: a bimonthly publication of the International Union of Biochemistry and Molecular Biology* 51.6 (2023), pp. 719–728. DOI: 10.1002/bmb.21771.

[10] Margret Schuller et al. *PCR for Clinical Microbiology*. Dordrecht: Springer Netherlands, 2010. ISBN: 978-90-481-9038-6. DOI: 10.1007/978-90-481-9039-3.

[11] Azar D. Khosravi et al. “Identification of Mycobacterium tuberculosis in Clinical Specimens of Patients Suspected of Having Extrapulmonary Tuberculosis by Application of Nested PCR on Five Different Genes”. In: *Frontiers in cellular and infection microbiology* 7 (2017), p. 3. DOI: 10.3389/fcimb.2017.00003.

[12] Ying Liu et al. “Detection of 12 Common Food-Borne Bacterial Pathogens by TaqMan Real-Time PCR Using a Single Set of Reaction Conditions”. In: *Frontiers in microbiology* 10 (2019), p. 222. ISSN: 1664-302X. DOI: 10.3389/fmicb.2019.00222.

[13] Antonio Barrientos-Durán et al. “Detection of sexually transmitted disease-causing pathogens from direct clinical specimens with the multiplex PCR-based STD Direct Flow Chip Kit”. In: *European journal of clinical microbiology & infectious diseases: official publication of the European Society of Clinical Microbiology* 39.2 (2020), pp. 235–241. DOI: 10.1007/s10096-019-03686-w.

[14] Jan M. M. Walboomers et al. “Human papillomavirus is a necessary cause of invasive cervical cancer worldwide”. In: *The Journal of Pathology* 189.1 (1999), pp. 12–19. ISSN: 0022-3417. DOI: 10.1002/(SICI)1096-9896(199909)189:1{\%}3C12::AID-PATH431{\%}3E3.0.CO;2-F.

[15] Victor M. Corman et al. “Detection of 2019 novel coronavirus (2019-nCoV) by real-time RT-PCR”. In: *Euro surveillance: bulletin Europeen sur les maladies transmis-*

sibles = European communicable disease bulletin 25.3 (2020). DOI: 10.2807/1560-7917.ES.2020.25.3.2000045.

[16] Omkaram Gangisetty and Doodipala Samba Reddy. "The optimization of TaqMan real-time RT-PCR assay for transcriptional profiling of GABA-A receptor subunit plasticity". In: *Journal of neuroscience methods* 181.1 (2009), pp. 58–66. DOI: 10.1016/j.jneumeth.2009.04.016.

[17] Nicklas N. Poulsen et al. "Flow-Induced Dispersion Analysis for Probing Anti-dsDNA Antibody Binding Heterogeneity in Systemic Lupus Erythematosus Patients: Toward a New Approach for Diagnosis and Patient Stratification". In: *Analytical chemistry* 88.18 (2016), pp. 9056–9061. DOI: 10.1021/acs.analchem.6b01741.

[18] Wenchong Shao et al. "Highly sensitive detection of DNA fragments by fluorescence correlation spectroscopy". In: *Optics in Health Care and Biomedical Optics X*. Ed. by Qingming Luo et al. SPIE, 11/10/2020 - 16/10/2020, p. 95. ISBN: 9781510639218. DOI: 10.1117/12.2575144.

[19] Guillaume Octobre et al. "Monitoring the interaction between DNA and a transcription factor (MEF2A) using fluorescence correlation spectroscopy". In: *Comptes rendus biologies* 328.12 (2005), pp. 1033–1040. ISSN: 1631-0691. DOI: 10.1016/j.crvi.2005.07.007.

[20] Sen Hou et al. "Fluorescence correlation spectroscopy analysis for accurate determination of proportion of doubly labeled DNA in fluorescent DNA pool for quantitative biochemical assays". In: *Biosensors & bioelectronics* 51 (2014), pp. 8–15. DOI: 10.1016/j.bios.2013.07.010.

[21] Aoune Barhoumi et al. "Surface-enhanced Raman spectroscopy of DNA". In: *Journal of the American Chemical Society* 130.16 (2008), pp. 5523–5529. DOI: 10.1021/ja800023j.

[22] Sajanlal R. Panikkanvalappil, Megan A. Mackey, and Mostafa A. El-Sayed. "Probing the unique dehydration-induced structural modifications in cancer cell DNA using surface enhanced Raman spectroscopy". In: *Journal of the American Chemical Society* 135.12 (2013), pp. 4815–4821. DOI: 10.1021/ja400187b.

[23] Keiko Ito, Koji Hashimoto, and Yoshio Ishimori. “Quantitative analysis for solid-phase hybridization reaction and binding reaction of DNA binder to hybrids using a quartz crystal microbalance”. In: *Analytica Chimica Acta* 327.1 (1996), pp. 29–35. ISSN: 00032670. DOI: 10.1016/0003-2670(96)00061-X.

[24] Natália Oliveira et al. “A Sensitive and Selective Label-Free Electrochemical DNA Biosensor for the Detection of Specific Dengue Virus Serotype 3 Sequences”. In: *Sensors (Basel, Switzerland)* 15.7 (2015), pp. 15562–15577. DOI: 10.3390/s150715562.

[25] Kumar Sapkota et al. “Single-Step FRET-Based Detection of Femtomoles DNA”. In: *Sensors (Basel, Switzerland)* 19.16 (2019). DOI: 10.3390/s19163495.

[26] Anoja Megalathan, Kalani M. Wijesinghe, and Soma Dhakal. “Single-Molecule FRET-Based Dynamic DNA Sensor”. In: *ACS sensors* 6.3 (2021), pp. 1367–1374. DOI: 10.1021/acssensors.1c00002.

[27] Lei He et al. “Fluorescence Resonance Energy Transfer-Based DNA Tetrahedron Nanotweezer for Highly Reliable Detection of Tumor-Related mRNA in Living Cells”. In: *ACS nano* 11.4 (2017), pp. 4060–4066. DOI: 10.1021/acsnano.7b00725.

[28] Shuai Zhang et al. “Ratiometric DNA sensing with a host-guest FRET pair”. In: *Chemical communications (Cambridge, England)* 55.5 (2019), pp. 671–674. DOI: 10.1039/C8CC09126A.

[29] Prinjaporn Teengam et al. “Fluorescent paper-based DNA sensor using pyrrolidinyl peptide nucleic acids for hepatitis C virus detection”. In: *Biosensors & bioelectronics* 189 (2021), p. 113381. DOI: 10.1016/j.bios.2021.113381.

[30] Yanan Zhang et al. “Fluorescence turn-on detection of target sequence DNA based on silicon nanodot-mediated quenching”. In: *Analytical and bioanalytical chemistry* 410.13 (2018), pp. 3209–3216. DOI: 10.1007/s00216-018-1030-x.

[31] Shan Huang et al. “A simple QD-FRET bioprobe for sensitive and specific detection of hepatitis B virus DNA”. In: *Journal of fluorescence* 23.5 (2013), pp. 1089–1098. DOI: 10.1007/s10895-013-1238-2.

[32] Mojtaba Shamsipur et al. “A highly sensitive quantum dots-DNA nanobiosensor based on fluorescence resonance energy transfer for rapid detection of nanomolar amounts of human papillomavirus 18”. In: *Journal of pharmaceutical and biomedical analysis* 136 (2017), pp. 140–147. DOI: 10.1016/j.jpba.2017.01.002.

[33] Zhen Gui et al. “Direct detection of circulating free DNA extracted from serum samples of breast cancer using locked nucleic acid molecular beacon”. In: *Talanta* 154 (2016), pp. 520–525. DOI: 10.1016/j.talanta.2016.04.008.

[34] Chunyuan Song et al. “High-Sensitive Assay of Nucleic Acid Using Tetrahedral DNA Probes and DNA Concatamers with a Surface-Enhanced Raman Scattering/Surface Plasmon Resonance Dual-Mode Biosensor Based on a Silver Nanorod-Covered Silver Nanohole Array”. In: *ACS applied materials & interfaces* 12.28 (2020), pp. 31242–31254. DOI: 10.1021/acsami.0c08453.

[35] Ibrahim Khalil et al. “Graphene oxide and gold nanoparticle based dual platform with short DNA probe for the PCR free DNA biosensing using surface-enhanced Raman scattering”. In: *Biosensors & bioelectronics* 131 (2019), pp. 214–223. DOI: 10.1016/j.bios.2019.02.028.

[36] Mei Chen et al. “An electrochemical DNA biosensor based on nitrogen-doped graphene/Au nanoparticles for human multidrug resistance gene detection”. In: *Biosensors & bioelectronics* 85 (2016), pp. 684–691. DOI: 10.1016/j.bios.2016.05.051.

[37] Huayu Huang et al. “An ultrasensitive electrochemical DNA biosensor based on graphene/Au nanorod/polythionine for human papillomavirus DNA detection”. In: *Biosensors & bioelectronics* 68 (2015), pp. 442–446. DOI: 10.1016/j.bios.2015.01.039.

[38] Valentina Di Meo et al. “Advanced DNA Detection via Multispectral Plasmonic Metasurfaces”. In: *Frontiers in bioengineering and biotechnology* 9 (2021), p. 666121. ISSN: 2296-4185. DOI: 10.3389/fbioe.2021.666121.

[39] Ankan Dutta Chowdhury et al. “The detection and identification of dengue virus serotypes with quantum dot and AuNP regulated localized surface plasmon resonance”. In: *Nanoscale advances* 2.2 (2020), pp. 699–709. DOI: 10.1039/C9NA00763F.

[40] Hassan H. Fakih, Malek M. Itani, and Pierre Karam. "Gold nanoparticles-coated polystyrene beads for the multiplex detection of viral DNA". In: *Sensors and Actuators B: Chemical* 250 (2017), pp. 446–452. ISSN: 09254005. DOI: 10.1016/j.snb.2017.04.066.

[41] Fang Wang et al. "Near-infrared band Gold nanoparticles-Au film "hot spot" model based label-free ultratrace lead (II) ions detection via fiber SPR DNAzyme biosensor". In: *Sensors and Actuators B: Chemical* 337 (2021), p. 129816. ISSN: 09254005. DOI: 10.1016/j.snb.2021.129816.

[42] Nicholas R. Y. Ho et al. "Visual and modular detection of pathogen nucleic acids with enzyme-DNA molecular complexes". In: *Nature communications* 9.1 (2018), p. 3238. DOI: 10.1038/s41467-018-05733-0.

[43] Yu Ling et al. "A dual-cycling biosensor for target DNA detection based on the toehold-mediated strand displacement reaction and exonuclease III assisted amplification". In: *New Journal of Chemistry* 42.6 (2018), pp. 4714–4718. ISSN: 1144-0546. DOI: 10.1039/C7NJ05191C.

[44] Shun Wang et al. "Electrochemical detection of hepatitis B and papilloma virus DNAs using SWCNT array coated with gold nanoparticles". In: *Biosensors & bioelectronics* 41 (2013), pp. 205–210. DOI: 10.1016/j.bios.2012.08.021.

[45] Katarzyna Kurzątkowska et al. "Electrochemical label-free and reagentless genosensor based on an ion barrier switch-off system for DNA sequence-specific detection of the avian influenza virus". In: *Analytical chemistry* 87.19 (2015), pp. 9702–9709. DOI: 10.1021/acs.analchem.5b01988.

[46] Brian Cannon et al. "Zeptomole detection of DNA nanoparticles by single-molecule fluorescence with magnetic field-directed localization". In: *Analytical biochemistry* 431.1 (2012), pp. 40–47. DOI: 10.1016/j.ab.2012.08.017.

[47] Li Li et al. "Ultra-sensitive DNA assay based on single-molecule detection coupled with fluorescent quantum dot-labeling and its application to determination of messenger RNA". In: *Analytica Chimica Acta* 685.1 (2011), pp. 52–57. ISSN: 00032670. DOI: 10.1016/j.aca.2010.11.012.

[48] Hamdi Joda et al. “Design of Gaussia luciferase-based bioluminescent stem-loop probe for sensitive detection of HIV-1 nucleic acids”. In: *The Analyst* 143.14 (2018), pp. 3374–3381. DOI: 10.1039/C8AN00047F.

[49] Sai Bi, Shuzhen Yue, and Shusheng Zhang. “Hybridization chain reaction: a versatile molecular tool for biosensing, bioimaging, and biomedicine”. In: *Chemical Society reviews* 46.14 (2017), pp. 4281–4298. DOI: 10.1039/C7CS00055C.

[50] Leyla Esfandiari et al. “Sequence-specific DNA detection at 10 fM by electromechanical signal transduction”. In: *Analytical chemistry* 86.19 (2014), pp. 9638–9643. DOI: 10.1021/ac5021408.

[51] Lihui Yuwen, Shifeng Zhang, and Jie Chao. “Recent Advances in DNA Nanotechnology-Enabled Biosensors for Virus Detection”. In: *Biosensors* 13.8 (2023). DOI: 10.3390/bios13080822.

[52] Mohsen Shariati. “Impedimetric Biosensor for Monitoring Complementary DNA from Hepatitis B Virus Based on Gold Nanocrystals”. In: *Journal of The Electrochemical Society* 168.1 (2021), p. 016512. ISSN: 0013-4651. DOI: 10.1149/1945-7111/abdc72.

[53] Liqun He et al. “Digital immunoassay for biomarker concentration quantification using solid-state nanopores”. In: *Nature communications* 12.1 (2021), p. 5348. DOI: 10.1038/s41467-021-25566-8.

[54] Xiaohan Chen et al. “Nanopore Single-molecule Analysis of Biomarkers: Providing Possible Clues to Disease Diagnosis”. In: *Trends in analytical chemistry: TRAC* 162 (2023). ISSN: 0165-9936. DOI: 10.1016/j.trac.2023.117060.

[55] Breeana Elliott et al. “Solid-state nanopore counting of amplicons from recombinase polymerase isothermal amplification”. In: *Sensors & Diagnostics* 3.10 (2024), pp. 1733–1742. DOI: 10.1039/d4sd00159a.

[56] Silvia Hernández-Ainsa and Ulrich F. Keyser. “DNA origami nanopores: developments, challenges and perspectives”. In: *Nanoscale* 6.23 (2014), pp. 14121–14132. DOI: 10.1039/C4NR04094E.

[57] Oliver Lieleg and Katharina Ribbeck. “Biological hydrogels as selective diffusion barriers”. In: *Trends in cell biology* 21.9 (2011), pp. 543–551. DOI: 10.1016/j.tcb.2011.06.002.

[58] Filipp V. Lavrentev et al. “Diffusion-Limited Processes in Hydrogels with Chosen Applications from Drug Delivery to Electronic Components”. In: *Molecules (Basel, Switzerland)* 28.15 (2023). DOI: 10.3390/molecules28155931.

[59] Paige J. Moncure et al. “Relationship between Gel Mesh and Particle Size in Determining Nanoparticle Diffusion in Hydrogel Nanocomposites”. In: *The journal of physical chemistry. B* 126.22 (2022), pp. 4132–4142. DOI: 10.1021/acs.jpcb.2c00771.

[60] Amel Djoudi et al. “Hyaluronic Acid Scaffolds for Loco-Regional Therapy in Nervous System Related Disorders”. In: *International journal of molecular sciences* 23.20 (2022). DOI: 10.3390/ijms232012174.

[61] Jinlong Li, Xin Jia, and Lijun Yin. “Hydrogel: Diversity of Structures and Applications in Food Science”. In: *Food Reviews International* 37.3 (2021), pp. 313–372. ISSN: 8755-9129. DOI: 10.1080/87559129.2020.1858313.

[62] Karolina Kulka and Alina Sionkowska. “Chitosan Based Materials in Cosmetic Applications: A Review”. In: *Molecules (Basel, Switzerland)* 28.4 (2023). DOI: 10.3390/molecules28041817.

[63] Faheem Ullah et al. “Classification, processing and application of hydrogels: A review”. In: *Materials science & engineering. C, Materials for biological applications* 57 (2015), pp. 414–433. DOI: 10.1016/j.msec.2015.07.053.

[64] Ujith S. K. Madduma-Bandarage and Sundararajan V. Madihally. “Synthetic hydrogels: Synthesis, novel trends, and applications”. In: *Journal of Applied Polymer Science* 138.19 (2021). ISSN: 0021-8995. DOI: 10.1002/app.50376.

[65] Daniel Buenger, Fuat Topuz, and Juergen Groll. “Hydrogels in sensing applications”. In: *Progress in Polymer Science* 37.12 (2012), pp. 1678–1719. ISSN: 00796700. DOI: 10.1016/j.progpolymsci.2012.09.001.

[66] Todd R. Hoare and Daniel S. Kohane. “Hydrogels in drug delivery: Progress and challenges”. In: *Polymer* 49.8 (2008), pp. 1993–2007. ISSN: 00323861. DOI: 10.1016/j.polymer.2008.01.027.

[67] Lixuan Hu et al. “Hydrogel-Based Flexible Electronics”. In: *Advanced materials (Deerfield Beach, Fla.)* 35.14 (2023), e2205326. DOI: 10.1002/adma.202205326.

[68] Nurettin Sahiner. "Soft and flexible hydrogel templates of different sizes and various functionalities for metal nanoparticle preparation and their use in catalysis". In: *Progress in Polymer Science* 38.9 (2013), pp. 1329–1356. ISSN: 00796700. DOI: 10.1016/j.progpolymsci.2013.06.004.

[69] Brian Amsden. "Solute Diffusion within Hydrogels. Mechanisms and Models". In: *Macromolecules* 31.23 (1998), pp. 8382–8395. ISSN: 0024-9297. DOI: 10.1021/ma980765f.

[70] Brian Amsden. "An Obstruction-Scaling Model for Diffusion in Homogeneous Hydrogels". In: *Macromolecules* 32.3 (1999), pp. 874–879. ISSN: 0024-9297. DOI: 10.1021/ma980922a.

[71] Brian G. Amsden. "Hydrogel Mesh Size and Its Impact on Predictions of Mathematical Models of the Solute Diffusion Coefficient". In: *Macromolecules* 55.18 (2022), pp. 8399–8408. ISSN: 0024-9297. DOI: 10.1021/acs.macromol.2c01443.

[72] Nathan R. Richbourg and Nicholas A. Peppas. "The swollen polymer network hypothesis: Quantitative models of hydrogel swelling, stiffness, and solute transport". In: *Progress in Polymer Science* 105 (2020), p. 101243. ISSN: 00796700. DOI: 10.1016/j.progpolymsci.2020.101243.

[73] Günter Majer and Alexander Southan. "Adenosine triphosphate diffusion through poly(ethylene glycol) diacrylate hydrogels can be tuned by cross-link density as measured by PFG-NMR". In: *The Journal of Chemical Physics* 146.22 (2017), p. 225101. ISSN: 0021-9606. DOI: 10.1063/1.4984979.

[74] Günter Majer and Alexander Southan. *PFG-NMR studies of ATP diffusion in PEG-DA hydrogels and aqueous solutions of PEG-DA polymers*. 2018. DOI: 10.18419/opus-11236.

[75] Jennika Karvinen et al. "Characterization of the microstructure of hydrazone crosslinked polysaccharide-based hydrogels through rheological and diffusion studies". In: *Materials science & engineering. C, Materials for biological applications* 94 (2019), pp. 1056–1066. DOI: 10.1016/j.msec.2018.10.048.

[76] Yuhang Zhou et al. "Establishment of a Physical Model for Solute Diffusion in Hydrogel: Understanding the Diffusion of Proteins in Poly(sulfobetaine methacry-

late) Hydrogel". In: *The journal of physical chemistry. B* 121.4 (2017), pp. 800–814. DOI: 10.1021/acs.jpcb.6b10355.

[77] Andreas Bertz et al. "Mobility of green fluorescent protein in hydrogel-based drug-delivery systems studied by anisotropy and fluorescence recovery after photobleaching". In: *Macromolecular bioscience* 13.2 (2013), pp. 215–226. DOI: 10.1002/mabi.201200325.

[78] Elke Kaemmerer et al. "Gelatine methacrylamide-based hydrogels: an alternative three-dimensional cancer cell culture system". In: *Acta biomaterialia* 10.6 (2014), pp. 2551–2562. DOI: 10.1016/j.actbio.2014.02.035.

[79] Silviya P. Zustiak, Hacene Boukari, and Jennie B. Leach. "Solute diffusion and interactions in cross-linked poly(ethylene glycol) hydrogels studied by Fluorescence Correlation Spectroscopy". In: *Soft matter* 6.15 (2010). DOI: 10.1039/C0SM00111B.

[80] D. Sandrin et al. "Diffusion of macromolecules in a polymer hydrogel: from microscopic to macroscopic scales". In: *Physical chemistry chemical physics: PCCP* 18.18 (2016), pp. 12860–12876. DOI: 10.1039/C5CP07781H.

[81] Swen Lehmann, Sebastian Seiffert, and Walter Richtering. "Spatially resolved tracer diffusion in complex responsive hydrogels". In: *Journal of the American Chemical Society* 134.38 (2012), pp. 15963–15969. DOI: 10.1021/ja306808j.

[82] Joris Sprakel et al. "Rouse dynamics of colloids bound to polymer networks". In: *Physical review letters* 99.20 (2007), p. 208301. ISSN: 0031-9007. DOI: 10.1103/PhysRevLett.99.208301.

[83] Jonathan Celli et al. "Viscoelastic properties and dynamics of porcine gastric mucin". In: *Biomacromolecules* 6.3 (2005), pp. 1329–1333. ISSN: 1525-7797. DOI: 10.1021/bm0493990.

[84] Moira Lorenzo Lopez et al. "Diffusion of nanoparticles in heterogeneous hydrogels as vitreous humour in vitro substitutes". In: *Scientific reports* 14.1 (2024), p. 17441. DOI: 10.1038/s41598-024-68267-0.

[85] Federica Burla et al. "Particle diffusion in extracellular hydrogels". In: *Soft matter* 16.5 (2020), pp. 1366–1376. DOI: 10.1039/c9sm01837a.

[86] Yeong Jun Yu et al. "Hydrogel-incorporating unit in a well: 3D cell culture for high-throughput analysis". In: *Lab on a chip* 18.17 (2018), pp. 2604–2613. DOI: 10.1039/c8lc00525g.

[87] Lieber Po-Hung Li et al. "Biocompatible and Implantable Hydrogel Optical Waveguide with Lens–Microneedles for Enhancing Light Delivery in Photodynamic Therapy". In: *Advanced Photonics Research* 5.8 (2024). ISSN: 2699-9293. DOI: 10.1002/adpr.202400031.

[88] Daan W. de Kort et al. "NMR nanoparticle diffusometry in hydrogels: enhancing sensitivity and selectivity". In: *Analytical chemistry* 86.18 (2014), pp. 9229–9235. DOI: 10.1021/ac502211q.

[89] Daan W. de Kort et al. "Nanoparticle diffusometry for quantitative assessment of submicron structure in food biopolymer networks". In: *Trends in Food Science & Technology* 42.1 (2015), pp. 13–26. ISSN: 09242244. DOI: 10.1016/j.tifs.2014.11.003.

[90] Daan W. de Kort et al. "Heterogeneity of Network Structures and Water Dynamics in κ-Carrageenan Gels Probed by Nanoparticle Diffusometry". In: *Langmuir: the ACS journal of surfaces and colloids* 34.37 (2018), pp. 11110–11120. DOI: 10.1021/acs.langmuir.8b01052.

[91] Niklas Lorén et al. "Dendrimer diffusion in kappa-carrageenan gel structures". In: *Biomacromolecules* 10.2 (2009), pp. 275–284. ISSN: 1525-7797. DOI: 10.1021/bm801013x.

[92] Reut Mashiach, Liat Avram, and Amnon Bar-Shir. "Diffusion 19F-NMR of Nanofluorides: In Situ Quantification of Colloidal Diameters and Protein Corona Formation in Solution". In: *Nano letters* 22.21 (2022), pp. 8519–8525. DOI: 10.1021/acs.nanolett.2c02994.

[93] G. Lafitte et al. "Transport properties and aggregation phenomena of polyoxyethylene sorbitane monooleate (polysorbate 80) in pig gastrointestinal mucin and mucus". In: *Langmuir: the ACS journal of surfaces and colloids* 23.22 (2007), pp. 10933–10939. DOI: 10.1021/la701081s.

[94] G. Lafitte et al. “PFG-NMR diffusometry: a tool for investigating the structure and dynamics of noncommercial purified pig gastric mucin in a wide range of concentrations”. In: *Biopolymers* 86.2 (2007), pp. 165–175. ISSN: 0006-3525. DOI: 10.1002/bip.20717..

[95] Tom Brenner and Shingo Matsukawa. “Anomalous diffusion of poly(ethylene oxide) in agarose gels”. In: *International journal of biological macromolecules* 92 (2016), pp. 1151–1154. DOI: 10.1016/j.ijbiomac.2016.07.054.

[96] Florence Franconi et al. “NMR diffusometry: A new perspective for nanomedicine exploration”. In: *Journal of controlled release: official journal of the Controlled Release Society* 337 (2021), pp. 155–167. DOI: 10.1016/j.jconrel.2021.07.025.

[97] Ulf Olsson et al. “Normal and Reverse Vesicles with Nonionic Surfactant: Solvent Diffusion and Permeability”. In: *Langmuir: the ACS journal of surfaces and colloids* 12.12 (1996), pp. 3045–3054. DOI: 10.1021/la9600560.

[98] Annalisa Caria, Oren Regev, and Ali Khan. “Surfactant–Polymer Interactions: Phase Diagram and Fusion of Vesicle in the Didodecyldimethylammonium Bromide–Poly(ethylene oxide)–Water System”. In: *Journal of colloid and interface science* 200.1 (1998), pp. 19–30. DOI: 10.1006/jcis.1997.5310.

[99] T. Kawaguchi et al. “The Bi-modality Diffusion of Water Molecules in Liposome/Water Dispersion Systems Analyzed by Pulsed Field Gradient Spin Echo NMR Method”. In: *Transactions of the Materials Research Society of Japan* 41.4 (2016), pp. 359–362. ISSN: 1382-3469. DOI: 10.14723/tmrsj.41.359.

[100] Helena Wassenius and Paul T. Callaghan. “Nanoscale NMR velocimetry by means of slowly diffusing tracer particles”. In: *Journal of magnetic resonance (San Diego, Calif.: 1997)* 169.2 (2004), pp. 250–256. DOI: 10.1016/j.jmr.2004.05.005.

[101] H. Wassenius and P. T. Callaghan. “NMR velocimetry studies of the steady-shear rheology of a concentrated hard-sphere colloidal system”. In: *The European physical journal. E, Soft matter* 18.1 (2005), pp. 69–84. ISSN: 1292-8941. DOI: 10.1140/epje/i2004-10155-4.

[102] Einar Orn Fridjonsson, Joseph D. Seymour, and Sarah L. Codd. “Anomalous preasymptotic colloid transport by hydrodynamic dispersion in microfluidic cap-

illary flow". In: *Physical review. E, Statistical, nonlinear, and soft matter physics* 90.1 (2014), p. 010301. DOI: 10.1103/PhysRevE.90.010301.

[103] Einar O. Fridjonsson and Joseph D. Seymour. "Colloid particle transport in a microcapillary: NMR study of particle and suspending fluid dynamics". In: *Chemical Engineering Science* 153 (2016), pp. 165–173. ISSN: 00092509. DOI: 10.1016/j.ces.2016.07.005.

[104] Tyler R. Brosten et al. "NMR measurement of the transport dynamics of colloidal particles in an open cell polymer foam porous media". In: *Journal of colloid and interface science* 349.1 (2010), pp. 384–391. DOI: 10.1016/j.jcis.2010.04.050.

[105] Jennifer R. Brown et al. "Dynamics of the solid and liquid phases in dilute sheared Brownian suspensions: irreversibility and particle migration". In: *Physical review letters* 99.24 (2007), p. 240602. ISSN: 0031-9007. DOI: 10.1103/PhysRevLett.99.240602.

[106] Jennifer R. Brown et al. "Nuclear magnetic resonance measurement of shear-induced particle migration in Brownian suspensions". In: *Physics of Fluids* 21.9 (2009). ISSN: 1070-6631. DOI: 10.1063/1.3230498.

[107] E. M. Purcell. "Life at low Reynolds number". In: *American Journal of Physics* 45.1 (1977), pp. 3–11. ISSN: 0002-9505. DOI: 10.1119/1.10903.

[108] ANDRE G. ROY et al. "Size, shape and dynamics of large-scale turbulent flow structures in a gravel-bed river". In: *Journal of Fluid Mechanics* 500 (2004), pp. 1–27. ISSN: 0022-1120. DOI: 10.1017/S0022112003006396.

[109] John F. Douglas. *Fluid mechanics*. 5th ed. Harlow England and New York: Pearson/Prentice Hall, 2005. ISBN: 0131292935.

[110] Jeremy M. Berg et al. *Stryer Biochemie*. Berlin, Heidelberg: Springer Berlin Heidelberg, 2018. ISBN: 978-3-662-54619-2. DOI: 10.1007/978-3-662-54620-8.

[111] Gerald Karp. *Cell and molecular biology: Concepts and experiments*. 6th ed. Hoboken NJ: John Wiley, 2010. ISBN: 0470483377.

[112] R. N. Upton and D. J. Doolette. "Kinetic aspects of drug disposition in the lungs". In: *Clinical and experimental pharmacology & physiology* 26.5-6 (1999), pp. 381–391. ISSN: 0305-1870. DOI: 10.1046/j.1440-1681.1999.03048.x.

[113] Paul T. Callaghan. *Translational Dynamics and Magnetic Resonance*. Oxford University Press, 2011. ISBN: 9780198700821.

[114] Adolf Fick. "Ueber Diffusion". In: *Annalen der Physik* 170.1 (1855), pp. 59–86. ISSN: 0003-3804. DOI: 10.1002/andp.18551700105.

[115] Ryogo Kubo, Morikazu Toda, and Natsuki Hashitsume. *Statistical Physics II*. Vol. 31. Berlin, Heidelberg: Springer Berlin Heidelberg, 1991. ISBN: 978-3-540-53833-2. DOI: 10.1007/978-3-642-58244-8.

[116] A. Einstein. "Über die von der molekularkinetischen Theorie der Wärme geforderte Bewegung von in ruhenden Flüssigkeiten suspendierten Teilchen". In: *Annalen der Physik* 322.8 (1905), pp. 549–560. ISSN: 0003-3804. DOI: 10.1002/andp.19053220806.

[117] William S. Price. "Pulsed-field gradient nuclear magnetic resonance as a tool for studying translational diffusion: Part 1. Basic theory". In: *Concepts in Magnetic Resonance* 9.5 (1997), pp. 299–336. ISSN: 1043-7347. DOI: 10.1002/(SICI)1099-0534(1997)9:5{\%}3C299::AID-CMR2{\%}3E3.0.CO;2-U.

[118] William Sutherland. "LXXV. A dynamical theory of diffusion for non-electrolytes and the molecular mass of albumin". In: *The London, Edinburgh, and Dublin Philosophical Magazine and Journal of Science* 9.54 (1905), pp. 781–785. ISSN: 1941-5982. DOI: 10.1080/14786440509463331.

[119] William S. Price. *NMR Studies of Translational Motion*. Cambridge University Press, 2009. ISBN: 9780521806961. DOI: 10.1017/CBO9780511770487.

[120] Helena Wassenius, Magnus Nydén, and Brian Vincent. "NMR diffusion studies of translational properties of oil inside core-shell latex particles". In: *Journal of colloid and interface science* 264.2 (2003), pp. 538–547. DOI: 10.1016/S0021-9797(03)00474-0.

[121] A. Pochert et al. "Diffusion and Molecular Exchange in Hollow Core-Shell Silica Nanoparticles". In: *Langmuir: the ACS journal of surfaces and colloids* 31.37 (2015), pp. 10285–10295. DOI: 10.1021/acs.langmuir.5b02367.

[122] Jörg Kärger et al. "Pulsed field gradient NMR diffusion measurement in nanoporous materials". In: *Adsorption* 27.3 (2021), pp. 453–484. ISSN: 0929-5607. DOI: 10.1007/s10450-020-00290-9.

[123] Gerardo Palazzo and Luigi Paduano. "Diffusion measuring techniques". In: *Colloidal Foundations of Nanoscience*. Elsevier, 2022, pp. 257–287. ISBN: 9780128220894. DOI: 10.1016/B978-0-12-822089-4.00004-0.

[124] Hermann Sicius. *Handbuch der chemischen Elemente*. Berlin, Heidelberg: Springer Berlin Heidelberg, 2023. ISBN: 978-3-662-65663-1. DOI: 10.1007/978-3-662-65664-8.

[125] Wolfgang Schlegel, Christian P. Karger, and Oliver Jäkel. *Medizinische Physik*. Berlin, Heidelberg: Springer Berlin Heidelberg, 2018. ISBN: 978-3-662-54800-4. DOI: 10.1007/978-3-662-54801-1.

[126] Bruker. *Almanac 2011: Analytical Tables and Product Overview*. 2011.

[127] Fatemeh Khashami. *Fundamentals of NMR and MRI*. Cham: Springer Nature Switzerland, 2024. ISBN: 978-3-031-47975-5. DOI: 10.1007/978-3-031-47976-2.

[128] Charles P. Slichter. *Principles of Magnetic Resonance*. 3rd Enlarged and Updated Edition 1990, Corrected 3rd Printing 1996. Vol. 1. Berlin, Heidelberg: Springer Berlin Heidelberg, 1990. ISBN: 978-3-642-08069-2. DOI: 10.1007/978-3-662-09441-9.

[129] Hermann Haken and Hans Christoph Wolf. *Molekülphysik und Quantenchemie*. Berlin/Heidelberg: Springer-Verlag, 2006. ISBN: 3-540-30314-6. DOI: 10.1007/3-540-30315-4.

[130] Dieter Meschede. *Gerthsen Physik*. Berlin, Heidelberg: Springer Berlin Heidelberg, 2015. ISBN: 978-3-662-45976-8. DOI: 10.1007/978-3-662-45977-5.

[131] Harald Günther. *NMR spectroscopy: Basic principles, concepts, and applications in chemistry*. Third, completely revised and updated edition. Weinheim: Wiley-VCH Verlag GmbH & Co. KGaA, 2013. ISBN: 978-3-527-33004-1.

[132] Daniel Canet. *NMR-Konzepte und Methoden: Übers. aus dem Franz. von E. Krahé*. Berlin et al.: Springer, 1994. ISBN: 3-540-58204-5.

[133] F. Bloch. "Nuclear Induction". In: *Physical Review* 70.7-8 (1946), pp. 460–474. ISSN: 0031-899X. DOI: 10.1103/PhysRev.70.460.

[134] Bernd Reif et al. "Solid-state NMR spectroscopy". In: *Nature reviews. Methods primers* 1 (2021). DOI: 10.1038/s43586-020-00002-1.

[135] Lixin Liang et al. “Solid-State NMR Dipolar and Chemical Shift Anisotropy Recoupling Techniques for Structural and Dynamical Studies in Biological Systems”. In: *Chemical reviews* 122.10 (2022), pp. 9880–9942. DOI: 10.1021/acs.chemrev.1c00779.

[136] E. L. Hahn. “Spin Echoes”. In: *Physical Review* 80.4 (1950), pp. 580–594. ISSN: 0031-899X. DOI: 10.1103/PhysRev.80.580.

[137] Jay W. Pettegrew. *NMR: Principles and Applications to Biomedical Research*. New York, NY: Springer New York, 1990. ISBN: 978-1-4612-7957-0. DOI: 10.1007/978-1-4612-3300-8.

[138] Geir Humborstad Sørland. *Dynamic Pulsed-Field-Gradient NMR*. Vol. 110. Berlin, Heidelberg: Springer Berlin Heidelberg, 2014. ISBN: 978-3-662-44499-3. DOI: 10.1007/978-3-662-44500-6.

[139] E. O. Stejskal and J. E. Tanner. “Spin Diffusion Measurements: Spin Echoes in the Presence of a Time-Dependent Field Gradient”. In: *The Journal of Chemical Physics* 42.1 (1965), pp. 288–292. ISSN: 0021-9606. DOI: 10.1063/1.1695690.

[140] H. C. Torrey. “Bloch Equations with Diffusion Terms”. In: *Physical Review* 104.3 (1956), pp. 563–565. ISSN: 0031-899X. DOI: 10.1103/PhysRev.104.563.

[141] William S. Price and Philip W. Kuchel. “Effect of nonrectangular field gradient pulses in the stejskal and tanner (diffusion) pulse sequence”. In: *Journal of Magnetic Resonance (1969)* 94.1 (1991), pp. 133–139. ISSN: 00222364. DOI: 10.1016/0022-2364(91)90300-I.

[142] Jan-Philipp Günther, Günter Majer, and Peer Fischer. “Absolute diffusion measurements of active enzyme solutions by NMR”. In: *The Journal of Chemical Physics* 150.12 (2019), p. 124201. ISSN: 0021-9606. DOI: 10.1063/1.5086427.

[143] J. E. Tanner. “Use of the Stimulated Echo in NMR Diffusion Studies”. In: *The Journal of Chemical Physics* 52.5 (1970), pp. 2523–2526. ISSN: 0021-9606. DOI: 10.1063/1.1673336.

[144] Wenjia Zhang et al. “Quantifying Binding of Ethylene Oxide-Propylene Oxide Block Copolymers with Lipid Bilayers”. In: *Langmuir: the ACS journal of surfaces and colloids* 33.44 (2017), pp. 12624–12634. DOI: 10.1021/acs.langmuir.7b02279.

[145] Magnus Röding et al. "The gamma distribution model for pulsed-field gradient NMR studies of molecular-weight distributions of polymers". In: *Journal of magnetic resonance (San Diego, Calif.: 1997)* 222 (2012), pp. 105–111. DOI: 10.1016/j.jmr.2012.07.005.

[146] B. Håkansson, M. Nydén, and O. Söderman. "The influence of polymer molecular-weight distributions on pulsed field gradient nuclear magnetic resonance self-diffusion experiments". In: *Colloid & Polymer Science* 278.5 (2000), pp. 399–405. ISSN: 0303-402X. DOI: 10.1007/s003960050532.

[147] Malvern Panalytical Ltd. *NanoSight NS300*. URL: https://www.malvernpanalytical.com/en/support/product-support/nanosight-range/nanosight-ns300.

[148] R. A. Dragovic et al. "Isolation of syncytiotrophoblast microvesicles and exosomes and their characterisation by multicolour flow cytometry and fluorescence Nanoparticle Tracking Analysis". In: *Methods (San Diego, Calif.)* 87 (2015), pp. 64–74. DOI: 10.1016/j.ymeth.2015.03.028.

[149] Vasco Filipe, Andrea Hawe, and Wim Jiskoot. "Critical evaluation of Nanoparticle Tracking Analysis (NTA) by NanoSight for the measurement of nanoparticles and protein aggregates". In: *Pharmaceutical research* 27.5 (2010), pp. 796–810. DOI: 10.1007/s11095-010-0073-2.

[150] Rebecca A. Dragovic et al. "Sizing and phenotyping of cellular vesicles using Nanoparticle Tracking Analysis". In: *Nanomedicine: nanotechnology, biology, and medicine* 7.6 (2011), pp. 780–788. DOI: 10.1016/j.nano.2011.04.003.

[151] Pauline Carnell-Morris et al. "Analysis of Extracellular Vesicles Using Fluorescence Nanoparticle Tracking Analysis". In: *Methods in molecular biology (Clifton, N.J.)* 1660 (2017), pp. 153–173. DOI: 10.1007/978-1-4939-7253-1_13.

[152] Jörg Stetefeld, Sean A. McKenna, and Trushar R. Patel. "Dynamic light scattering: a practical guide and applications in biomedical sciences". In: *Biophysical reviews* 8.4 (2016), pp. 409–427. ISSN: 1867-2450. DOI: 10.1007/s12551-016-0218-6.

[153] Bruce Alberts. *Molecular biology of the cell*. Sixth edition. New York NY: Garland Science Taylor and Francis Group, 2015. ISBN: 978-0-8153-4464-3.

[154] Swarup Dey et al. “DNA origami”. In: *Nature Reviews Methods Primers* 1.1 (2021). DOI: 10.1038/s43586-020-00009-8.

[155] J. H. Chen and N. C. Seeman. “Synthesis from DNA of a molecule with the connectivity of a cube”. In: *Nature* 350.6319 (1991), pp. 631–633. DOI: 10.1038/350631a0.

[156] Nadrian C. Seeman and Hanadi F. Sleiman. “DNA nanotechnology”. In: *Nature Reviews Materials* 3.1 (2018). DOI: 10.1038/natrevmats.2017.68.

[157] Paul W. K. Rothemund. “Folding DNA to create nanoscale shapes and patterns”. In: *Nature* 440.7082 (2006), pp. 297–302. DOI: 10.1038/nature04586.

[158] Shawn M. Douglas et al. “Self-assembly of DNA into nanoscale three-dimensional shapes”. In: *Nature* 459.7245 (2009), pp. 414–418. DOI: 10.1038/nature08016.

[159] Kerstin Göpfrich and Ulrich F. Keyser. “DNA Nanotechnology for Building Sensors, Nanopores and Ion-Channels”. In: *Advances in experimental medicine and biology* 1174 (2019), pp. 331–370. ISSN: 0065-2598. DOI: 10.1007/978-981-13-9791-2{\textunderscore}11.

[160] Pengfei Zhan et al. “Recent Advances in DNA Origami-Engineered Nanomaterials and Applications”. In: *Chemical reviews* 123.7 (2023), pp. 3976–4050. DOI: 10.1021/acs.chemrev.3c00028.

[161] Pengfei Wang et al. “The Beauty and Utility of DNA Origami”. In: *Chem* 2.3 (2017), pp. 359–382. ISSN: 24519294. DOI: 10.1016/j.chempr.2017.02.009.

[162] Zhimei He et al. “Self-assembly of DNA origami for nanofabrication, biosensing, drug delivery, and computational storage”. In: *iScience* 26.5 (2023), p. 106638. DOI: 10.1016/j.isci.2023.106638.

[163] Ebbe S. Andersen et al. “Self-assembly of a nanoscale DNA box with a controllable lid”. In: *Nature* 459.7243 (2009), pp. 73–76. DOI: 10.1038/nature07971.

[164] Shawn M. Douglas et al. “Rapid prototyping of 3D DNA-origami shapes with caDNAno”. In: *Nucleic acids research* 37.15 (2009), pp. 5001–5006. DOI: 10.1093/nar/gkp436.

[165] A. Loxley and B. Vincent. "Preparation of Poly(methylmethacrylate) Microcapsules with Liquid Cores". In: *Journal of colloid and interface science* 208.1 (1998), pp. 49–62. DOI: 10.1006/jcis.1998.5698.

[166] Peter J. Dowding et al. "Oil core-polymer shell microcapsules prepared by internal phase separation from emulsion droplets. I. Characterization and release rates for microcapsules with polystyrene shells". In: *Langmuir: the ACS journal of surfaces and colloids* 20.26 (2004), pp. 11374–11379. DOI: 10.1021/la048561h.

[167] Viktor Eriksson et al. "Formulation of polyphthalaldehyde microcapsules for immediate UV-light triggered release". In: *Journal of colloid and interface science* 579 (2020), pp. 645–653. DOI: 10.1016/j.jcis.2020.06.024.

[168] Viktor Eriksson et al. "Polyanhydride Microcapsules Exhibiting a Sharp pH Transition at Physiological Conditions for Instantaneous Triggered Release". In: *Langmuir: the ACS journal of surfaces and colloids* 39.49 (2023), pp. 18003–18010. DOI: 10.1021/acs.langmuir.3c02708.

[169] Viktor Eriksson et al. "A unified thermodynamic and kinetic approach for prediction of microcapsule morphologies". In: *Journal of colloid and interface science* 662 (2024), pp. 572–582. DOI: 10.1016/j.jcis.2024.01.191.

[170] S. Torza and S.G Mason. "Three-phase interactions in shear and electrical fields". In: *Journal of colloid and interface science* 33.1 (1970), pp. 67–83. DOI: 10.1016/0021-9797(70)90073-1.

[171] Anna Maria Peri et al. "New Microbiological Techniques for the Diagnosis of Bacterial Infections and Sepsis in ICU Including Point of Care". In: *Current infectious disease reports* 23.8 (2021), p. 12. ISSN: 1523-3847. DOI: 10.1007/s11908-021-00755-0.

[172] Walter Florio et al. "Detection of Antibiotic-Resistance by MALDI-TOF Mass Spectrometry: An Expanding Area". In: *Frontiers in cellular and infection microbiology* 10 (2020), p. 572909. DOI: 10.3389/fcimb.2020.572909.

[173] Caroline Weis et al. "Direct antimicrobial resistance prediction from clinical MALDI-TOF mass spectra using machine learning". In: *Nature medicine* 28.1 (2022), pp. 164–174. DOI: 10.1038/s41591-021-01619-9.

[174] Scott L. Weiss et al. “Surviving Sepsis Campaign International Guidelines for the Management of Septic Shock and Sepsis-Associated Organ Dysfunction in Children”. In: *Pediatric critical care medicine: a journal of the Society of Critical Care Medicine and the World Federation of Pediatric Intensive and Critical Care Societies* 21.2 (2020), e52–e106. ISSN: 1529-7535. DOI: 10.1097/PCC.0000000000002198.

[175] Liqun He et al. *Digital Immunoassay Protocol for Solid-State Nanopore Sensing*. 2022. DOI: 10.21203/rs.3.pex-1591/v1.

[176] Deepak Koirala et al. “Single-molecule mechanochemical sensing using DNA origami nanostructures”. In: *Angewandte Chemie (International ed. in English)* 53.31 (2014), pp. 8137–8141. DOI: 10.1002/anie.201404043.

[177] Yike Huang et al. “A DNA Origami-Based Chiral Plasmonic Sensing Device”. In: *ACS applied materials & interfaces* 10.51 (2018), pp. 44221–44225. DOI: 10.1021/acsami.8b19153.

[178] Shuang Wang et al. “DNA Origami-Enabled Biosensors”. In: *Sensors (Basel, Switzerland)* 20.23 (2020). DOI: 10.3390/s20236899.

[179] Caiqing Yuan et al. “Functionalized DNA Origami-Enabled Detection of Biomarkers”. In: *Chembiochem: a European journal of chemical biology* 25.13 (2024), e202400227. DOI: 10.1002/cbic.202400227.

[180] Timon Funck et al. “Sensing Picomolar Concentrations of RNA Using Switchable Plasmonic Chirality”. In: *Angewandte Chemie (International ed. in English)* 57.41 (2018), pp. 13495–13498. DOI: 10.1002/anie.201807029.

[181] Timon Funck, Tim Liedl, and Wooli Bae. “Dual Aptamer-Functionalized 3D Plasmonic Metamolecule for Thrombin Sensing”. In: *Applied Sciences* 9.15 (2019), p. 3006. DOI: 10.3390/app9153006.

[182] Mihir Dass et al. “DNA Origami-Enabled Plasmonic Sensing”. In: *The journal of physical chemistry. C, Nanomaterials and interfaces* 125.11 (2021), pp. 5969–5981. ISSN: 1932-7447. DOI: 10.1021/acs.jpcc.0c11238.

[183] Sarah E. Ochmann et al. “DNA Origami Voltage Sensors for Transmembrane Potentials with Single-Molecule Sensitivity”. In: *Nano letters* 21.20 (2021), pp. 8634–8641. DOI: 10.1021/acs.nanolett.1c02584.

[184] Arun Richard Chandrasekaran et al. "Beyond the Fold: Emerging Biological Applications of DNA Origami". In: *Chembiochem: a European journal of chemical biology* 17.12 (2016), pp. 1081–1089. DOI: 10.1002/cbic.201600038.

[185] Arun Richard Chandrasekaran, Muthuirulan Pushpanathan, and Ken Halvorsen. "Evolution of DNA origami scaffolds". In: *Materials Letters* 170 (2016), pp. 221–224. ISSN: 0167577X. DOI: 10.1016/j.matlet.2016.01.161.

[186] Arun Richard Chandrasekaran et al. "DNA nanotechnology approaches for microRNA detection and diagnosis". In: *Nucleic acids research* 47.20 (2019), pp. 10489–10505. DOI: 10.1093/nar/gkz580.

[187] Ping Liu et al. "Thermophoretic Analysis of Biomolecules across the Nanoscales in Self-Assembled Polymeric Matrices". In: *ACS Applied Nano Materials* 6.20 (2023), pp. 19148–19157. ISSN: 2574-0970. DOI: 10.1021/acsanm.3c03623.

[188] Samet Kocabey et al. "Membrane-assisted growth of DNA origami nanostructure arrays". In: *ACS nano* 9.4 (2015), pp. 3530–3539. DOI: 10.1021/acsnano.5b00161.

[189] Beatrice Ramm et al. "A diffusiophoretic mechanism for ATP-driven transport without motor proteins". In: *Nature Physics* 17.7 (2021), pp. 850–858. ISSN: 1745-2473. DOI: 10.1038/s41567-021-01213-3.

[190] Alena Khmelinskaia et al. "Control of Membrane Binding and Diffusion of Cholesteryl-Modified DNA Origami Nanostructures by DNA Spacers". In: *Langmuir: the ACS journal of surfaces and colloids* 34.49 (2018), pp. 14921–14931. DOI: 10.1021/acs.langmuir.8b01850.

[191] A. Rita Silva-Santos, Pedro M.R. Paulo, and Duarte Miguel F. Prazeres. "Scalable purification of single stranded DNA scaffolds for biomanufacturing DNA-origami nanostructures: Exploring anion-exchange and multimodal chromatography". In: *Separation and Purification Technology* 298 (2022), p. 121623. ISSN: 13835866. DOI: 10.1016/j.seppur.2022.121623.

[192] M. Dienerowitz, F. Dienerowitz, and M. Börsch. "Measuring nanoparticle diffusion in an ABELtrap". In: *Journal of Optics* 20.3 (2018), p. 034006. ISSN: 2040-8978. DOI: 10.1088/2040-8986/aaa6fc.

[193] Kan Du et al. “Quantum dot-DNA origami binding: a single particle, 3D, real-time tracking study”. In: *Chemical communications (Cambridge, England)* 49.9 (2013), pp. 907–909. DOI: 10.1039/c2cc37517f.

[194] Mariana Alarcón-Correa et al. “Platinum-DNA Origami Hybrid Structures in Concentrated Hydrogen Peroxide”. In: *Chemphyschem: a European journal of chemical physics and physical chemistry* 24.22 (2023), e202300294. DOI: 10.1002/cphc.202300294.

[195] Johann D. D. Pitout et al. “The Global Ascendency of OXA-48-Type Carbapenemases”. In: *Clinical microbiology reviews* 33.1 (2019). DOI: 10.1128/cmr.00102-19.

[196] Sara E. Boyd et al. “OXA-48-Like β-Lactamases: Global Epidemiology, Treatment Options, and Development Pipeline”. In: *Antimicrobial agents and chemotherapy* 66.8 (2022), e0021622. DOI: 10.1128/aac.00216-22.

[197] Brian P. Alcock et al. “CARD 2023: expanded curation, support for machine learning, and resistome prediction at the Comprehensive Antibiotic Resistance Database”. In: *Nucleic acids research* 51.D1 (2023), pp. D690–D699. DOI: 10.1093/nar/gkac920.

[198] National Library of Medicine, National Institutes of Health, and U.S. Department of Health and Human Services. *Klebsiella pneumoniae AAKS5 blaOXA-48 gene for beta-lactamase OXA-48, partial cds: Accession No. LC583819.1*. URL: https://www.ncbi.nlm.nih.gov/nuccore/LC583819.1.

[199] A. Yu. Men’shikova. “Monodisperse functional polymeric particles and their application for nanotechnology”. In: *Nanotechnologies in Russia* 5.1-2 (2010), pp. 35–48. ISSN: 1995-0780. DOI: 10.1134/S1995078010010039.

[200] Mohammed Ali Dheyab et al. “Monodisperse Gold Nanoparticles: A Review on Synthesis and Their Application in Modern Medicine”. In: *International journal of molecular sciences* 23.13 (2022). DOI: 10.3390/ijms23137400.

[201] Malvern Panalytical GmbH. *100nm Latex Size Indicator STD 3ml*. URL: https://mystore.malvernpanalytical.com/mystore/s/de/product/100nm-latex-size-indicator-std-3ml/01t0Y000008gfZDQAY.

[202] Chiara Guidolin et al. “Protein Sizing with Differential Dynamic Microscopy”. In: *Macromolecules* 56.20 (2023), pp. 8290–8297. ISSN: 0024-9297. DOI: 10.1021/acs.macromol.3c00782.

[203] W. F. Espenscheid, M. Kerker, and E. Matijević. “Logarithmic Distribution Functions for Colloidal Particles”. In: *The Journal of Physical Chemistry* 68.11 (1964), pp. 3093–3097. ISSN: 0022-3654. DOI: 10.1021/j100793a002.

[204] Weijun Bao et al. “Particle size distribution mathematical models and properties of suspended solids in a typical freshwater pond”. In: *Environmental pollution (Barking, Essex: 1987)* 241 (2018), pp. 164–171. DOI: 10.1016/j.envpol.2018.05.063.

[205] Hossein Bayat et al. “Particle size distribution models, their characteristics and fitting capability”. In: *Journal of Hydrology* 529 (2015), pp. 872–889. ISSN: 00221694. DOI: 10.1016/j.jhydrol.2015.08.067.

[206] N. R. J. Fieller, E. C. Flenley, and W. Olbricht. “Statistics of Particle Size Data”. In: *Applied Statistics* 41.1 (1992), p. 127. ISSN: 00359254. DOI: 10.2307/2347623.

[207] Mathew Stracy and Achillefs N. Kapanidis. “Single-molecule and super-resolution imaging of transcription in living bacteria”. In: *Methods (San Diego, Calif.)* 120 (2017), pp. 103–114. DOI: 10.1016/j.ymeth.2017.04.001.

[208] Marija Vrljic et al. “Translational diffusion of individual class II MHC membrane proteinsin cells”. In: *Biophysical journal* 83.5 (2002), pp. 2681–2692.

[209] Thomas E. Ouldridge, Ard A. Louis, and Jonathan P. K. Doye. “Structural, mechanical, and thermodynamic properties of a coarse-grained DNA model”. In: *The Journal of Chemical Physics* 134.8 (2011). ISSN: 0021-9606. DOI: 10.1063/1.3552946.

[210] Erik Poppleton et al. “oxDNA: coarse-grained simulations of nucleic acids made simple”. In: *Journal of Open Source Software* 8.81 (2023), p. 4693. DOI: 10.21105/joss.04693.

[211] Benedict E. K. Snodin et al. “Introducing improved structural properties and salt dependence into a coarse-grained model of DNA”. In: *The Journal of Chemical Physics* 142.23 (2015). ISSN: 0021-9606. DOI: 10.1063/1.4921957.

[212] Klaus F. Wagenbauer et al. “How We Make DNA Origami”. In: *Chembiochem: a European journal of chemical biology* 18.19 (2017), pp. 1873–1885. DOI: 10.1002/cbic.201700377.

[213] Heini Ijäs et al. “Reconfigurable DNA Origami Nanocapsule for pH-Controlled Encapsulation and Display of Cargo”. In: *ACS nano* 13.5 (2019), pp. 5959–5967. DOI: 10.1021/acsnano.9b01857.

[214] Yuki Suzuki et al. “Lipid bilayer-assisted dynamic self-assembly of hexagonal DNA origami blocks into monolayer crystalline structures with designed geometries”. In: *iScience* 25.5 (2022), p. 104292. DOI: 10.1016/j.isci.2022.104292.

[215] Daichi Hayakawa et al. “Geometrically programmed self-limited assembly of tubules using DNA origami colloids”. In: *Proceedings of the National Academy of Sciences of the United States of America* 119.43 (2022), e2207902119. DOI: 10.1073/pnas.2207902119.

[216] Kerstin Göpfrich et al. “Large-Conductance Transmembrane Porin Made from DNA Origami”. In: *ACS nano* 10.9 (2016), pp. 8207–8214. DOI: 10.1021/acsnano.6b03759.

[217] Silvia Hernández-Ainsa et al. “DNA origami nanopores for controlling DNA translocation”. In: *ACS nano* 7.7 (2013), pp. 6024–6030. DOI: 10.1021/nn401759r.

[218] Kevin Jahnke et al. “Proton gradients from light-harvesting E. coli control DNA assemblies for synthetic cells”. In: *Nature communications* 12.1 (2021), p. 3967. DOI: 10.1038/s41467-021-24103-x.

[219] Pauline J. Kolbeck et al. “Molecular structure, DNA binding mode, photophysical properties and recommendations for use of SYBR Gold”. In: *Nucleic acids research* 49.9 (2021), pp. 5143–5158. DOI: 10.1093/nar/gkab265.

[220] Taehwi Kim et al. “Controlling Chiroptical Responses via Chemo-Mechanical Deformation of DNA Origami Structures”. In: *ACS nano* 18.4 (2024), pp. 3414–3423. DOI: 10.1021/acsnano.3c10386.

[221] Yang Xin et al. “Environment-Dependent Stability and Mechanical Properties of DNA Origami Six-Helix Bundles with Different Crossover Spacings”. In: *Small (Weinheim an der Bergstrasse, Germany)* 18.18 (2022), e2107393. DOI: 10.1002/smll.202107393.

[222] Antonio Suma et al. "TacoxDNA: A user–friendly web server for simulations of complex DNA structures, from single strands to origami". In: *Journal of Computational Chemistry* 40.29 (2019), pp. 2586–2595. ISSN: 0192-8651. DOI: 10.1002/jcc.26029.

[223] Erik Poppleton et al. "Design, optimization and analysis of large DNA and RNA nanostructures through interactive visualization, editing and molecular simulation". In: *Nucleic acids research* 48.12 (2020), e72–e72. DOI: 10.1093/nar/gkaa417.

[224] Joakim Bohlin et al. "Design and simulation of DNA, RNA and hybrid protein–nucleic acid nanostructures with oxView". In: *Nature Protocols* 17.8 (2022), pp. 1762–1788. ISSN: 1754-2189. DOI: 10.1038/s41596-022-00688-5.

[225] Jonathan P. K. Doye et al. "The oxDNA Coarse-Grained Model as a Tool to Simulate DNA Origami". In: *DNA and RNA Origami*. Ed. by Julián Valero. Vol. 2639. Methods in Molecular Biology. New York, NY: Springer US, 2023, pp. 93–112. ISBN: 978-1-0716-3027-3. DOI: 10.1007/978-1-0716-3028-0_6.

[226] Lorenzo Rovigatti et al. "A comparison between parallelization approaches in molecular dynamics simulations on GPUs". In: *Journal of Computational Chemistry* 36.1 (2015), pp. 1–8. ISSN: 0192-8651. DOI: 10.1002/jcc.23763.

[227] J. G. La Garcia de Torre and V. A. Bloomfield. "Hydrodynamic properties of complex, rigid, biological macromolecules: theory and applications". In: *Quarterly reviews of biophysics* 14.1 (1981), pp. 81–139. ISSN: 0033-5835. DOI: 10.1017/S0033583500002080.

[228] Ilja N. Bronštejn et al. *Taschenbuch der Mathematik*. 10., überarbeitete Auflage. Edition Harri Deutsch. Haan-Gruiten: Verlag Europa-Lehrmittel - Nourney Vollmer GmbH & Co. KG, 2016. ISBN: 978-3-8085-5789-1.

[229] Ousmane Oumou Diallo et al. "Antibiotic resistance surveillance systems: A review". In: *Journal of global antimicrobial resistance* 23 (2020), pp. 430–438. DOI: 10.1016/j.jgar.2020.10.009.

[230] Giuseppe Mancuso et al. "Bacterial Antibiotic Resistance: The Most Critical Pathogens". In: *Pathogens (Basel, Switzerland)* 10.10 (2021). ISSN: 2076-0817. DOI: 10.3390/pathogens10101310.

[231] Marianna D'Anca et al. "Exosome Determinants of Physiological Aging and Age-Related Neurodegenerative Diseases". In: *Frontiers in aging neuroscience* 11 (2019), p. 232. ISSN: 1663-4365. DOI: 10.3389/fnagi.2019.00232.

[232] Noah Kastelowitz and Hang Yin. "Exosomes and microvesicles: identification and targeting by particle size and lipid chemical probes". In: *Chembiochem: a European journal of chemical biology* 15.7 (2014), pp. 923–928. DOI: 10.1002/cbic.201400043.

[233] Fred Etoc et al. "Non-specific interactions govern cytosolic diffusion of nanosized objects in mammalian cells". In: *Nature materials* 17.8 (2018), pp. 740–746. DOI: 10.1038/s41563-018-0120-7.

[234] M. H. Blees, J. M. Geurts, and J. C. Leyte. "Self-Diffusion of Charged Polybutadiene Latex Particles in Water Measured by Pulsed Field Gradient NMR". In: *Langmuir: the ACS journal of surfaces and colloids* 12.8 (1996), pp. 1947–1957. DOI: 10.1021/la9502960.

[235] N. A. Peppas et al. "Physicochemical foundations and structural design of hydrogels in medicine and biology". In: *Annual review of biomedical engineering* 2 (2000), pp. 9–29. ISSN: 1523-9829. DOI: 10.1146/annurev.bioeng.2.1.9.

[236] Francisco Drusso Martinez-Garcia et al. "A Beginner's Guide to the Characterization of Hydrogel Microarchitecture for Cellular Applications". In: *Gels (Basel, Switzerland)* 8.9 (2022). DOI: 10.3390/gels8090535.

[237] Panchami Patel and Prachi Thareja. "Hydrogels differentiated by length scales: A review of biopolymer-based hydrogel preparation methods, characterization techniques, and targeted applications". In: *European Polymer Journal* 163 (2022), p. 110935. ISSN: 00143057. DOI: 10.1016/j.eurpolymj.2021.110935.

[238] Jennie Baier Leach et al. "Photocrosslinked hyaluronic acid hydrogels: natural, biodegradable tissue engineering scaffolds". In: *Biotechnology and bioengineering* 82.5 (2003), pp. 578–589. ISSN: 0006-3592. DOI: 10.1002/bit.10605.

[239] Benjamin S. Spearman et al. "Tunable methacrylated hyaluronic acid-based hydrogels as scaffolds for soft tissue engineering applications". In: *Journal of biomedical materials research. Part A* 108.2 (2020), pp. 279–291. DOI: 10.1002/jbm.a.36814.

[240] Margaux Vigata et al. “Hydrogels as Drug Delivery Systems: A Review of Current Characterization and Evaluation Techniques”. In: *Pharmaceutics* 12.12 (2020). ISSN: 1999-4923. DOI: 10.3390/pharmaceutics12121188.

[241] Cecília Leal et al. “Dynamic and structural aspects of PEGylated liposomes monitored by NMR”. In: *Journal of colloid and interface science* 325.2 (2008), pp. 485–493. DOI: 10.1016/j.jcis.2008.05.051.

[242] Fadwa Odeh et al. “PFG–NMR Investigation of Liposome Systems Containing Hydrotrope”. In: *Journal of Dispersion Science and Technology* 27.5 (2006), pp. 665–669. ISSN: 0193-2691. DOI: 10.1080/01932690600660574.

[243] Massimiliano Valentini et al. “Diffusion NMR spectroscopy for the characterization of the size and interactions of colloidal matter: the case of vesicles and nanoparticles”. In: *Journal of the American Chemical Society* 126.7 (2004), pp. 2142–2147. ISSN: 0002-7863. DOI: 10.1021/ja037247r.

[244] Joachim Wagner, Wolfram Härtl, and Harald Walderhaug. “Long time self-diffusion in suspensions of highly charged colloids: A comparison between pulsed field gradient NMR and Brownian dynamics”. In: *The Journal of Chemical Physics* 114.2 (2001), pp. 975–983. ISSN: 0021-9606. DOI: 10.1063/1.1326909.

[245] Sydney Chapman and T. G. Cowling. *The mathematical theory of non-uniform gases: An account of the kinetic theory of viscosity, thermal conduction, and diffusion in gases*. 3rd ed. Cambridge mathematical library. Cambridge and New York: Cambridge University Press, 1990. ISBN: 052140844X.

[246] Zuoyi Yang, Jiahao Cui, and Bo Yin. “Solubilization of Nitrogen Heterocyclic Compounds Using Different Surfactants”. In: *Water, Air, & Soil Pollution* 229.9 (2018). ISSN: 0049-6979. DOI: 10.1007/s11270-018-3917-8.

[247] Xing-Yu Li et al. “Conversion of biomass-derived fatty acids and derivatives into hydrocarbons using a metal-free hydrodeoxygenation process”. In: *Green Chemistry* 17.5 (2015), pp. 2790–2793. ISSN: 1463-9262. DOI: 10.1039/C5GC00556F.

[248] John H. Dymond and Kenneth R. Harris. “The temperature and density dependence of the self-diffusion coefficient of n -hexadecane”. In: *Molecular Physics* 75.2 (1992), pp. 461–466. ISSN: 0026-8976. DOI: 10.1080/00268979200100351.

[249] Nian-Sheng Cheng. “Formula for the Viscosity of a Glycerol−Water Mixture”. In: *Industrial & Engineering Chemistry Research* 47.9 (2008), pp. 3285–3288. ISSN: 0888-5885. DOI: 10.1021/ie071349z.

[250] Yoshihiro Nishida et al. “1H-NMR Karplus Analysis of Molecular Conformations of Glycerol under Different Solvent Conditions: A Consistent Rotational Isomerism in the Backbone Governed by Glycerol/Water Interactions”. In: *International journal of molecular sciences* 24.3 (2023). DOI: 10.3390/ijms24032766.

[251] Adam D. Wexler et al. “Nuclear Magnetic Relaxation Mapping of Spin Relaxation in Electrically Stressed Glycerol”. In: *ACS omega* 5.35 (2020), pp. 22057–22070. DOI: 10.1021/acsomega.0c02059.

[252] Victoria G. Muir and Jason A. Burdick. “Chemically Modified Biopolymers for the Formation of Biomedical Hydrogels”. In: *Chemical reviews* 121.18 (2021), pp. 10908–10949. DOI: 10.1021/acs.chemrev.0c00923.

[253] Carl C. L. Schuurmans et al. “Hyaluronic acid and chondroitin sulfate (meth)acrylate-based hydrogels for tissue engineering: Synthesis, characteristics and pre-clinical evaluation”. In: *Biomaterials* 268 (2021), p. 120602. DOI: 10.1016/j.biomaterials.2020.120602.

[254] Kimberly A. Smeds et al. “Synthesis of a novel polysaccharide hydrogel”. In: *Journal of Macromolecular Science, Part A* 36.7-8 (1999), pp. 981–989. ISSN: 1060-1325. DOI: 10.1080/10601329908951194.

[255] W.N.E. van Dijk-Wolthuls, S.K.Y. Tsang, and J. J. Kettenes-van den BoschW.E. Hennink. “A new class of polymerizable dextrans with hydrolyzable groups: hydroxyethyl methacrylated dextran with and without oligolactate spacer”. In: *Polymer* 38.25 (1997), pp. 6235–6242. ISSN: 00323861. DOI: 10.1016/S0032-3861(97)00189-4.

[256] Xinqiao Jia et al. “Synthesis and Characterization of in Situ Cross-Linkable Hyaluronic Acid-Based Hydrogels with Potential Application for Vocal Fold Regeneration”. In: *Macromolecules* 37.9 (2004), pp. 3239–3248. ISSN: 0024-9297. DOI: 10.1021/ma035970w.

[257] Junliang Lu et al. "Harnessing the potential of hyaluronic acid methacrylate (HAMA) hydrogel for clinical applications in orthopaedic diseases". In: *Journal of orthopaedic translation* 50 (2025), pp. 111–128. ISSN: 2214-031X. DOI: 10.1016/j.jot.2024.11.004.

[258] Liliang Ouyang et al. "3D Printing of Shear-Thinning Hyaluronic Acid Hydrogels with Secondary Cross-Linking". In: *ACS biomaterials science & engineering* 2.10 (2016), pp. 1743–1751. DOI: 10.1021/acsbiomaterials.6b00158.

[259] Gi-Woong Hong et al. "Manufacturing Process of Hyaluronic Acid Dermal Fillers". In: *Polymers* 16.19 (2024). DOI: 10.3390/polym16192739.

[260] Ane Albillos Sanchez et al. "Enhanced osteogenic differentiation in hyaluronic acid methacrylate (HAMA) matrix: a comparative study of hPDC and hBMSC spheroids for bone tissue engineering". In: *Biofabrication* 17.2 (2025). DOI: 10.1088/1758-5090/adb2e6.

[261] Giorgia D'Arrigo et al. "Hyaluronic acid methacrylate derivatives and calcium alginate interpenetrated hydrogel networks for biomedical applications: physico-chemical characterization and protein release". In: *Colloid and Polymer Science* 290.15 (2012), pp. 1575–1582. ISSN: 0303-402X. DOI: 10.1007/s00396-012-2735-6.

[262] Jason A. Burdick et al. "Controlled degradation and mechanical behavior of photopolymerized hyaluronic acid networks". In: *Biomacromolecules* 6.1 (2005), pp. 386–391. ISSN: 1525-7797. DOI: 10.1021/bm049508a.

[263] Sharon Gerecht et al. "Hyaluronic acid hydrogel for controlled self-renewal and differentiation of human embryonic stem cells". In: *Proceedings of the National Academy of Sciences of the United States of America* 104.27 (2007), pp. 11298–11303. ISSN: 0027-8424. DOI: 10.1073/pnas.0703723104.

[264] Ali Khademhosseini et al. "Micromolding of photocrosslinkable hyaluronic acid for cell encapsulation and entrapment". In: *Journal of biomedical materials research. Part A* 79.3 (2006), pp. 522–532. DOI: 10.1002/jbm.a.30821.

[265] Jie Hu et al. "Salvianolic acid B combined with bone marrow mesenchymal stem cells piggybacked on HAMA hydrogel re-transplantation improves intervertebral

disc degeneration". In: *Frontiers in bioengineering and biotechnology* 10 (2022), p. 950625. ISSN: 2296-4185. DOI: 10.3389/fbioe.2022.950625.

[266] Yang Zhou et al. "Arginine based poly (ester amide)/ hyaluronic acid hybrid hydrogels for bone tissue Engineering". In: *Carbohydrate polymers* 230 (2020), p. 115640. DOI: 10.1016/j.carbpol.2019.115640.

[267] Benjamin Teong et al. "The stiffness of a crosslinked hyaluronan hydrogel affects its chondro-induction activity on hADSCs". In: *Journal of biomedical materials research. Part B, Applied biomaterials* 106.2 (2018), pp. 808–816. DOI: 10.1002/jbm.b.33881.

[268] B. Velasco-Rodriguez et al. "Hybrid Methacrylated Gelatin and Hyaluronic Acid Hydrogel Scaffolds. Preparation and Systematic Characterization for Prospective Tissue Engineering Applications". In: *International journal of molecular sciences* 22.13 (2021). DOI: 10.3390/ijms22136758.

[269] Yongli Gao et al. "Components and physical properties of hydrogels modulate inflammatory response and cartilage repair". In: *Journal of materials chemistry. B* 11.41 (2023), pp. 10029–10042. DOI: 10.1039/d3tb01917a.

[270] Panita Maturavongsadit et al. "Influence of Cross-Linkers on the in Vitro Chondrogenesis of Mesenchymal Stem Cells in Hyaluronic Acid Hydrogels". In: *ACS applied materials & interfaces* 9.4 (2017), pp. 3318–3329. DOI: 10.1021/acsami.6b12437.

[271] Seok Hyun Lee et al. "3D bioprinting of human mesenchymal stem cells-laden hydrogels incorporating MXene for spontaneous osteodifferentiation". In: *Heliyon* 9.3 (2023), e14490. ISSN: 2405-8440. DOI: 10.1016/j.heliyon.2023.e14490.

[272] Huijuan Fu et al. "Application of 3D-printed tissue-engineered skin substitute using innovative biomaterial loaded with human adipose-derived stem cells in wound healing". In: *International journal of bioprinting* 9.2 (2023), p. 674. DOI: 10.18063/ijb.v9i2.674.

[273] Sara Nejati and Luc Mongeau. "Injectable, pore-forming, self-healing, and adhesive hyaluronan hydrogels for soft tissue engineering applications". In: *Scientific reports* 13.1 (2023), p. 14303. DOI: 10.1038/s41598-023-41468-9.

[274] Pavanchandh Atturu et al. "Adipose-derived stem cells loaded photocurable and bioprintable bioinks composed of GelMA, HAMA and PEGDA crosslinker to differentiate into smooth muscle phenotype". In: *International journal of biological macromolecules* 265.Pt 2 (2024), p. 130710. DOI: 10.1016/j.ijbiomac.2024.130710.

[275] Shuai Chen et al. "A 3D bioprinted adhesive tissue engineering scaffold to repair ischemic heart injury". In: *Biomaterials science* 13.2 (2025), pp. 506–522. DOI: 10.1039/d4bm00988f.

[276] Wangbei Cao et al. "Migration of endothelial cells into photo-responsive hydrogels with tunable modulus under the presence of pro-inflammatory macrophages". In: *Regenerative biomaterials* 6.5 (2019), pp. 259–267. ISSN: 2056-3418. DOI: 10.1093/rb/rbz025.

[277] Shan Yu et al. "A novel one-step mechanically strengthened hyaluronic acid hydrogel assisted by a small molecular agent". In: *Chemical Papers* 75.8 (2021), pp. 4093–4098. ISSN: 2585-7290. DOI: 10.1007/s11696-021-01635-6.

[278] Longxi Xiao et al. "Hyaluronic acid-based hydrogels containing covalently integrated drug depots: implication for controlling inflammation in mechanically stressed tissues". In: *Biomacromolecules* 14.11 (2013), pp. 3808–3819. ISSN: 1525-7797. DOI: 10.1021/bm4011276.

[279] Carl C. L. Schuurmans et al. "Complex coacervation-based loading and tunable release of a cationic protein from monodisperse glycosaminoglycan microgels". In: *Soft matter* 14.30 (2018), pp. 6327–6341. DOI: 10.1039/c8sm00686e.

[280] Eneko Axpe et al. "A Multiscale Model for Solute Diffusion in Hydrogels". In: *Macromolecules* 52.18 (2019), pp. 6889–6897. ISSN: 0024-9297. DOI: 10.1021/acs.macromol.9b00753:.

[281] Ateyyah M. Al-Baradi et al. "Magnetic field dependence of the diffusion of single dextran molecules within a hydrogel containing magnetite nanoparticles". In: *The Journal of Chemical Physics* 134.9 (2011), p. 094901. ISSN: 0021-9606. DOI: 10.1063/1.3557496.

[282] Irene M. Hansen et al. “Hyaluronic Acid Molecular Weight-Dependent Modulation of Mucin Nanostructure for Potential Mucosal Therapeutic Applications”. In: *Molecular pharmaceutics* 14.7 (2017), pp. 2359–2367. DOI: 10.1021/acs.molpharmaceut.7b00236.

[283] Chundong Xue et al. “Hopping Behavior Mediates the Anomalous Confined Diffusion of Nanoparticles in Porous Hydrogels”. In: *The journal of physical chemistry letters* 13.45 (2022), pp. 10612–10620. DOI: 10.1021/acs.jpclett.2c02733.

[284] Maayan Levin, Adar Sonn-Segev, and Yael Roichman. “Structural changes in nanoparticle-hydrogel composites at very low filler concentrations”. In: *The Journal of Chemical Physics* 150.6 (2019), p. 064908. ISSN: 0021-9606. DOI: 10.1063/1.5053171.

[285] Sandeep Palvai et al. “Free-Standing Hierarchically Porous Silica Nanoparticle Superstructures: Bridging the Nano- to Microscale for Tailorable Delivery of Small and Large Therapeutics”. In: *ACS applied materials & interfaces* 16.5 (2024), pp. 5568–5581. DOI: 10.1021/acsami.3c16463.

[286] Yuhang Huang et al. “Stimulus-Responsive Transport Properties of Nanocolloidal Hydrogels”. In: *Biomacromolecules* 24.3 (2023), pp. 1173–1183. ISSN: 1525-7797. DOI: 10.1021/acs.biomac.2c01222:.

[287] Seda Yamanlar et al. “Surface functionalization of hyaluronic acid hydrogels by polyelectrolyte multilayer films”. In: *Biomaterials* 32.24 (2011), pp. 5590–5599. DOI: 10.1016/j.biomaterials.2011.04.030.

[288] C. Picart et al. “Molecular basis for the explanation of the exponential growth of polyelectrolyte multilayers”. In: *Proceedings of the National Academy of Sciences of the United States of America* 99.20 (2002), pp. 12531–12535. ISSN: 0027-8424. DOI: 10.1073/pnas.202486099.

[289] Seth Rowland et al. “Layer-by-Layer Nanoparticle Assembly for Biomedicine: Mechanisms, Technologies, and Advancement via Acoustofluidics”. In: *ACS Applied Nano Materials* 7.14 (2024), pp. 15874–15902. ISSN: 2574-0970. DOI: 10.1021/acsanm.4c02463.

[290] Yajun Wang, Alexandra S. Angelatos, and Frank Caruso. "Template Synthesis of Nanostructured Materials via Layer-by-Layer Assembly". In: *Chemistry of Materials* 20.3 (2008), pp. 848–858. ISSN: 0897-4756. DOI: 10.1021/cm7024813.

[291] Miguel A. Ramos Docampo et al. "Self-Propelled Collagenase-Powered Nano/ Micromotors". In: *ACS Applied Nano Materials* 5.10 (2022), pp. 14622–14629. ISSN: 2574-0970. DOI: 10.1021/acsanm.2c02989.

[292] Marcin Płaczek and Magdalena Kosela. "Microscopic methods in analysis of submicron phospholipid dispersions". In: *Acta pharmaceutica (Zagreb, Croatia)* 66.1 (2016), pp. 1–22. DOI: 10.1515/acph-2016-0003.

[293] P. Couvreur. "Nanoparticles in drug delivery: past, present and future". In: *Advanced drug delivery reviews* 65.1 (2013), pp. 21–23. DOI: 10.1016/j.addr.2012.04.010.

[294] Esther Amstad and Erik Reimhult. "Nanoparticle actuated hollow drug delivery vehicles". In: *Nanomedicine (London, England)* 7.1 (2012), pp. 145–164. DOI: 10.2217/nnm.11.167.

[295] J. Danie Kingsley et al. "Nanotechnology for tissue engineering: Need, techniques and applications". In: *Journal of Pharmacy Research* 7.2 (2013), pp. 200–204. ISSN: 09746943. DOI: 10.1016/j.jopr.2013.02.021.

[296] Carlos F. Guimarães et al. "The stiffness of living tissues and its implications for tissue engineering". In: *Nature Reviews Materials* 5.5 (2020), pp. 351–370. DOI: 10.1038/s41578-019-0169-1.

[297] Soroosh Derakhshanfar et al. "3D bioprinting for biomedical devices and tissue engineering: A review of recent trends and advances". In: *Bioactive materials* 3.2 (2018), pp. 144–156. DOI: 10.1016/j.bioactmat.2017.11.008.

[298] Huawei Qu et al. "Biomaterials for bone tissue engineering scaffolds: a review". In: *RSC advances* 9.45 (2019), pp. 26252–26262. DOI: 10.1039/c9ra05214c.

[299] Badriprasad Ananthanarayanan, Yushan Kim, and Sanjay Kumar. "Elucidating the mechanobiology of malignant brain tumors using a brain matrix-mimetic hyaluronic acid hydrogel platform". In: *Biomaterials* 32.31 (2011), pp. 7913–7923. DOI: 10.1016/j.biomaterials.2011.07.005.

[300] William S. Price. “Pulsed-field gradient nuclear magnetic resonance as a tool for studying translational diffusion: Part II. Experimental aspects”. In: *Concepts in Magnetic Resonance* 10.4 (1998), pp. 197–237. ISSN: 1043-7347. DOI: 10.1002/(SICI)1099-0534(1998)10:4{\textless}197::AID-CMR1{\textgreater}3.0.CO;2-S.